Nucleon structure from lattice QCD

D I S S E R T A T I O N

zur Erlangung des akademischen Grades

doctor rerum naturalium
(Dr. rer. nat.)
im Fach Physik

eingereicht an der
Mathematisch-Naturwissenschaftlichen Fakultät I
Humboldt-Universität zu Berlin

von
Dipl.-Phys. Simon Dinter

Präsident der Humboldt-Universität zu Berlin:
Prof. Dr. Jan-Hendrik Olbertz

Dekan der Mathematisch-Naturwissenschaftlichen Fakultät I:
Prof. Stefan Hecht PhD

Gutachter:
1. Dr. habil. Karl Jansen
2. Prof. Dr. Michael Müller-Preußker
3. Dr. habil. Meinulf Göckeler

eingereicht am: 09. August 2012
Tag der mündlichen Prüfung: 13. November 2012

I dedicate my dissertation work
to my family und my friends

Zusammenfassung

In dieser Arbeit berechnen wir mit Hilfe der Gitter-QCD Observablen, die in Beziehung zur Struktur des Nukleons stehen. Ein Teil dieser Arbeit beschäftigt sich mit Momenten von Parton-Verteilungsfunktionen. Solche Momente sind wichtig für das Verständnis der Nukleon-Struktur und werden durch globale Analysen von tief-inelastischen Streuexperimenten bestimmt. Eine theoretische, nicht-perturbative Rechnung der Momente in der Gitter-QCD ist möglich. Allerdings existiert, seit solche Gitter-QCD Rechnungen vorliegen, eine Diskrepanz zwischen diesen Rechnungen und den Ergebnissen globaler Analysen experimenteller Daten. Wir untersuchen, ob systematische Effekte für diese Diskrepanz verantwortlich sind, dabei studieren wir insbesondere die Effekte angeregter Zustände. Zudem führen wir eine erste Rechnung mit vier dynamischen Quark-Flavors durch.
Ein weiterer Aspekt dieser Arbeit ist eine Machbarkeitsstudie zur Berechnung des skalaren Quark-Inhalts des Nukleons in der Gitter-QCD. Dieser bestimmt den Wirkungsquerschnitt der durch ein skalares Teilchen (z.B. ein Higgs-Teilchen) vermittelten Wechselwirkung eines schweren Teilchens mit einem Nukleon und kann somit einen Einfluss bei der Suche nach Dunkler Materie haben. Bisherige Gitter-Rechnungen dieser Größe besitzen große Unsicherheiten und sind daher von geringer Signifikanz für phenomenologische Anwendungen. Wir benutzen eine Varianz-Reduktions-Methode zur Auswertung von unverbundenen Diagrammen um ein präzises Ergebnis zu erhalten.
Des Weiteren stellen wir eine neue stochastische Methode zur Berechnung von Nukleon-Dreipunkt-Korrelationsfunktionen vor, die für die Berechnung von Observablen der Nukleon-Struktur benötigt werden. Wir testen die Konkurrenzfähigkeit dieser neuen Methode gegenüber der Standard-Methode.
In allen Rechnungen benutzen wir Wilson twisted-Mass Fermionen mit maximalem Twist, so dass die hier berechneten Observablen nur $\mathcal{O}(a^2)$ Diskretisierungsfehler aufweisen.

Abstract

In this thesis we compute within lattice QCD observables related to the structure of the nucleon. One part of this thesis is concerned with moments of parton distribution functions (PDFs). Those moments are essential elements for the understanding of nucleon structure and can be extracted from a global analysis of deep inelastic scattering experiments. On the theoretical side they can be computed non-perturbatively by means of lattice QCD. However, since the time lattice calculations of moments of PDFs are available, there is a tension between these lattice calculations and the results from a global analysis of experimental data. We examine whether systematic effects are responsible for this tension, and study particularly intensively the effects of excited states by a dedicated high precision computation. Moreover, we carry out a first computation with four dynamical flavors.
Another aspect of this thesis is a feasibility study of a lattice QCD computation of the scalar quark content of the nucleon, which is an important element in the cross-section of a heavy particle with the nucleon mediated by a scalar particle (*e.g.* Higgs particle) and can therefore have an impact on Dark Matter searches. Existing lattice QCD calculations of this quantity usually have a large error and thus a low significance for phenomenological applications. We use a variance-reduction technique for quark-disconnected diagrams to obtain a precise result.
Furthermore, we introduce a new stochastic method for the calculation of connected 3-point correlation functions, which are needed to compute nucleon structure observables, as an alternative to the usual sequential propagator method. In an explorative study we check whether this new method is competitive to the standard one.
We use Wilson twisted mass fermions at maximal twist in all our calculations, such that all observables considered here have only $\mathcal{O}(a^2)$ discretization effects.

Contents

1 Introduction

It is one of the fundamental challenges of Quantum Chromodynamics (QCD), as our theory of the strong interaction, to describe the structure of hadrons. The high energy, correspondingly short distance properties of this theory have been tested experimentally, partly with outstanding precision, at particle accelerators and other high energy experimental facilities such as Jlab and BNL. Thus, we have a very good understanding of QCD as the theory describing the short distance dynamics of quarks and gluons. However, there is no analytic description of the quark-gluon interaction at low energies and consequently, to the present day, we are lacking an *analytic* understanding of the mechanism that leads to the formation of hadrons. Thus, *e.g.* the masses of the simplest baryons, the nucleons, of which basically all visible matter in our universe consists, cannot be computed analytically.

Lattice QCD has significantly furthered the understanding of the quark-gluon dynamics at low energies by computer simulations. In this way the lattice community has been able to correctly compute the mass spectrum of mesons and baryons from a first principles QCD calculation and hence proves that that the mass spectrum can be explained by QCD. Of course, it still remains to be seen, whether also other low energy phenomena such as the spontaneous breaking of chiral symmetry or the structure of the hadrons follow from QCD.

Lattice QCD can in principle provide information on the low energy sector of QCD and, in particular, the inner structure of mesons and baryons. This thesis is concerned with the calculation of quantities related to the inner structure of nucleons. In particular, we calculate moments of parton distribution functions and the scalar quark contents of the nucleon. As these quantities contain information about the constitution of the nucleon, they can help to shed light on the dynamics taking place inside protons and neutrons.

Besides the importance to understand hadron structure from a first principles QCD calculation, there is another puzzling aspect. At present, there is a tension between value of moments of parton distribution functions calculated in lattice QCD and their experimental counterparts. It is one of the main goals of this thesis to resolve this tension. As an example, even for simple moments like the nucleon axial charge g_A or the first moment of the unpolarized parton distribution (in the isovector flavor combination) $\langle x \rangle_{u-d}$, there exists a difference between results obtained from global analyses of experimental data and from lattice QCD calculations which is significantly greater than the quoted uncertainties.
The most likely explanation for this mismatch is that systematic effects are not well-controlled. Lattice QCD computations are subject to several such systematic effects. Our aim is hence to perform a comprehensive study of systematic effects and attempt to see, whether they can resolve the aforementioned conflict.

Particular focus will be on excited state effects that lattice calculations have to deal with and which can severely affect results from lattice calculations. Other systematic effects are discretization and finite volume effects and the, still, necessary extrapolation of the results to physical values of the pion mass. We will discuss all these lattice effects in detail in this thesis and try to understand, whether controlling these systematic errors can reconcile the discrepancy between lattice calculations and experimental determinations of at least g_A and $\langle x \rangle_{u-d}$ as the here considered benchmark observables.

As a second key target we want to calculate the scalar quark content of the nucleon, which is, for reasons that we explain later, a very challenging calculation on the lattice. Such a theoretical calculation is appealing since hardly anything is known about this quantity. However it is an important quantity in models of physics beyond the standard model. It governs the interaction between the nucleon and a massive particle through the exchange of a scalar particle such as the Higgs boson. This massive particle can be a weakly interactive massive particle (WIMP) - a promising candidate for Dark Matter.
Here, we would like to provide a reliable computation of scalar matrix elements of the nucleon $\langle N|\bar{q}q|N\rangle$. Those matrix elements are a low-energy quantity and therefore not directly accessible by perturbative QCD. It can be calculated indirectly at the cost of large systematic uncertainties. A direct calculation with lattice QCD methods is therefore very desirable, but present results have a rather large error such that the significance for phenomenological applications is questionable. Using a special noise-reduction technique, we attempt to obtain precise results for the scalar matrix elements of the nucleon for all quarks of the first two generations.

Besides the physical quantities we want to address in this thesis, there is also a very important technical aspect, namely the efficient calculation of 3-point correlation functions which underlie the evaluation of the quantities mentioned above. We explore a new method for the evaluation of connected 3-point correlation functions of the nucleon, which are needed for the evaluation of nucleon matrix elements. It is not clear whether this method, involving a stochastic estimation of a quark propagator, is competitive compared to the method typically employed in the calculation of nucleon structure, the so-called sequential method with fixed sink. The stochastic method has the advantage of higher versatility, but is potentially more expensive concerning the computational effort. Our objective here is more of exploratory nature. We need to develop new methods and perform a a number of tests in order to clarify the potential of the method. The feasibility of the method will be tested in a benchmark calculation, including the scaling of the computational cost with increasing volume.

We would like to remark that without the collaboration with the European Twisted Mass collaboration (ETMC), providing configurations, computing resources and cross-checks, and in particular knowledge and experience, this work would not have been possible. Acknowledging this, we use the first person plural throughout this thesis.

This thesis is organized as follows:
In Chapter 2 we explain how hadron structure can be accessed by experiment as well as with lattice QCD methods. In addition, we introduce the observables this thesis is concerned with. In Chapter 3, we introduce the nucleon correlation functions needed for the calculation of nucleon matrix elements and explain how the latter are obtained from suitable ratios of correlation

functions. We also discuss how excited state contributions can enter in the calculation. A brief introduction of some basic elements of lattice QCD is given in Chapter 4. In this chapter we also discuss some of the systematic effects which lattice QCD calculations have to deal with. While Chapter 4 is meant as a basic introduction, we concentrate on the more technical elements and methods employed in the scope of this thesis work in Chapter 5.
We discuss the stochastic method mentioned above in Chapter 6, where we present a study of the feasibility and explain a few benefits of this method. Chapter 7 deals with moments of parton distributions. We describe the tension between experimental results and results from lattice QCD calculations for the simple observables g_A and $\langle x \rangle_{u-d}$ and present a study of systematic effects, in particular contributions from excited states. Chapter 8 covers the lattice computation of the scalar quark content of the nucleon. We present an explorative study and discuss the impact of excited state effects.
Finally, we give a summary in Chapter 9.

2 Hadron Structure from Experiment and from Lattice QCD

This thesis is concerned with the structure of the nucleon. In experiments one can gather information about the inner structure of hadrons – such as nucleons – through scattering experiments. For example, there are fixed-target experiments with a high energy electron beam sent through hydrogen or deuteron target, or the famous lepton-proton collision experiments at particle accelerators like HERA.

The measurable (differential) cross section is theoretically given by a kinematic factor containing the details of the process and a factor given by an element of the scattering matrix that depends on the underlying theory (here: QED and QCD) describing the interactions between the particles. As we will see in the following sections we are particularly interested in matrix elements of the nucleon $\langle N| \bar{q}\hat{X}q |N\rangle$, where $|N\rangle$ denotes a nucleon state and $\bar{q}\hat{X}q$ represents a quantum-mechanical operator that involves two quark fields of flavor q. Those matrix elements in fact provide information about the nucleon structure. On the one hand they are related to the elastic (Compton) scattering amplitude through the operator product expansion (OPE), and can therefore be accessed in deep inelastic scattering (DIS) experiments. On the other hand they can be determined in lattice QCD from a first-principles calculation. Depending on the operator $\bar{q}\hat{X}q$ we can obtain information not only about the quark content of the nucleon but also about the distributions of momentum, angular momentum or spin of the constituent quarks.

We start with a discussion of DIS revealing the proton structure. Then we discuss what the observables of interest are and how to compute them from experimental data and in lattice QCD.

2.1 Deep Inelastic Scattering

A major tool for the study of nucleon structure is electron scattering, the reason being the well understood interaction of the electron with another particle carrying electric charge in the framework of Quantum Electrodynamics, such that the interaction of the electron with a nucleon can serve the purpose of probing the unknown structure of the latter. We will learn how this is done in practice in the course of this section.

Let us start with a bit of history. In the late 1960s electron-proton scattering experiments were performed at the Stanford Linear Accelerator (SLAC) in the highly inelastic kinematic region, which means essentially at high center of mass energies and momentum transfer [1, 2]. The

outcome of those inelastic scattering experiments which was in sharp contrast to the elastic scattering results, suggested a non-trivial substructure of the proton[1]. Inspired by Feynman, Bjorken tried to explain the DIS data using an intuitive model, in which the proton is not a fundamental particle but consists of point-like constituents, called partons, off which the electron scatters elastically [3]. This results in a cross-section that does not depend on the energy of the incoming electron, which is known as Bjorken scaling and was found to hold true in good approximation at high momentum transfers. Thus the findings of the DIS scattering experiments established the parton picture of the nucleon and eventually guided the way for QCD as the theory of strong interactions and the quarks and gluons being the constituents of hadrons.
We discuss the scattering process quantitatively in the following and demonstrate how to obtain information about nucleon structure therefrom. Also, we are going to see how nucleon structure can be computed in lattice QCD.

Deep inelastic scattering is the common term for the scattering of a lepton (typically e^+/e^-) off a hadron (typically a nucleon) at high momentum transfer. We denote this by the reaction

$$l(p) + N(P) \to l'(p') + X(P_X). \tag{2.1}$$

where l and l' label the initial and final lepton, respectively, and N is the nucleon. The final (hadronic) states except for the scattered lepton itself are summarized in X, *i.e.* the reaction above is to be understood as fully inclusive. We have additionally written the corresponding 4-momenta in parentheses.

If the momentum is not too high the neutral current process ($l = l'$ in 2.1) is dominated by a one-photon exchange. This particular process is illustrated in Fig. 2.1, where we only write the momenta from Eq. (2.1), $q = p - p'$ is the momentum transfer.

The inclusive process (2.1) is described by 3 kinematic variables. One may choose as the first one the (square of the) center-of-mass energy

$$s = (p + P)^2, \tag{2.2}$$

which is typically fixed by the experimental setup, *e.g.* the beam energy in a particle collider. The other two may be chosen from the following ones,

$$Q^2 = -q^2 = -(p - p')^2 \tag{2.3}$$

$$x = \frac{Q^2}{2P \cdot q} = \frac{Q^2}{2m_N \nu} \tag{2.4}$$

$$\nu = \frac{P \cdot q}{m_N}. \tag{2.5}$$

In the equations above, m_N labels the nucleon mass and q is again the momentum transfer. The variable ν corresponds to the transferred energy in the rest frame of the nucleon and x is the

[1] To be more precise, the inelastic cross-section was found to be nearly independent of the momentum transfer, whereas the elastic cross-section possesses a steep momentum transfer dependence.

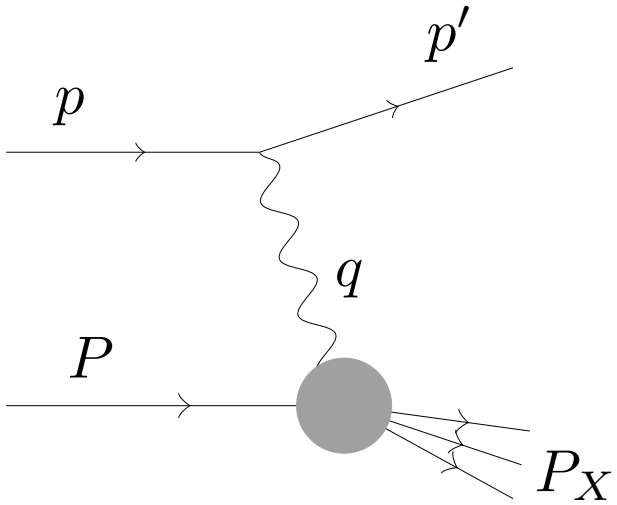

Figure 2.1: Typical DIS process.

Bjorken variable. Now, DIS in terms of those variables is the regime, where

$$m_N \nu \gg m_N^2, \tag{2.6}$$
$$Q^2 \gg m_N^2, \tag{2.7}$$
$$x \quad \text{fixed and finite.} \tag{2.8}$$

The differential cross section for the (unpolarized) DIS process shown in Fig. 2.1 is

$$d\sigma = \frac{1}{4p \cdot P} \frac{1}{4} \sum_{s_l, S} \sum_{s_{l'}, X} \int \frac{d^3 P_X}{(2\pi)^3 2P_X^0} \frac{d^3 p'}{(2\pi)^3 2E'} (2\pi)^4 \delta^{(4)} \left(p + P - p' - P_X\right) |\mathcal{M}|^2 , \tag{2.9}$$

where E' denotes the energy of the outgoing lepton l' and we have a sum over the spins of the initial (s_l,S) and all final states ($s_{l'}$,X). The element of the scattering matrix $\mathcal{M}$ that encodes the quantum field theoretical part of the cross section, can be straightforwardly calculated in QED, but in QCD it contains unknown elements. It is expressed in terms of a leptonic tensor $L_{\mu\nu}$ and a hadronic tensor $W_{\mu\nu}$.

$$|\mathcal{M}|^2 \sim L_l^{\mu\nu} W_{\mu\nu}, \tag{2.10}$$
$$L^{\mu\nu}(p, p') = 2 \left(p'^{\mu} p^{\nu} + p'^{\nu} p^{\mu} - g^{\mu\nu} p \cdot p'\right), \tag{2.11}$$
$$W_{\mu\nu}(P, q) = \int d^4 z \, e^{iq \cdot z} \langle P | \left[J^{\mu}(z), J^{\nu}(0)\right] | P \rangle \tag{2.12}$$

Here, J^{μ} is the hadronic current, which is – in contrast to the leoptonic current – unknown. Lorentz and gauge invariance in combination with the parity conservation of the electromagnetic current imply that the hadronic tensor, encoding the response of the nucleon, is of the

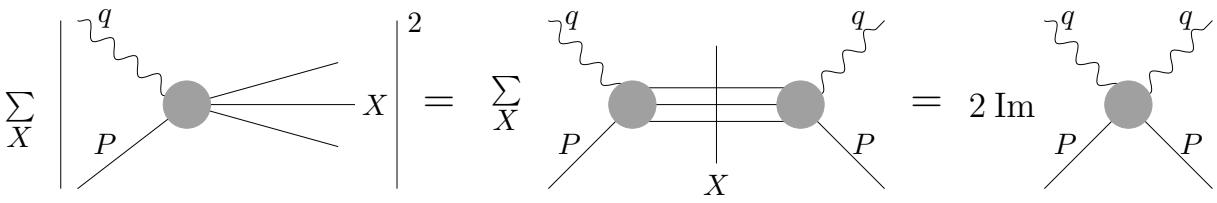

Figure 2.2: Illustration of the relation between the hadronic part of a DIS process (left) mediated by a photon and the virtual Compton scattering amplitude (right). The sum is taken over all final states X.

general form

$$\begin{aligned} W_{\mu\nu} = \quad & W_1(\nu, Q^2)\left(\frac{q_\mu q_\nu}{q^2} - g_{\mu\nu}\right) \\ & + \frac{W_2(\nu, Q^2)}{m_N^2}\left(P_\mu - \frac{P\cdot q}{q^2}q_\mu\right)\left(P_\nu - \frac{P\cdot q}{q^2}q_\nu\right) \end{aligned} \tag{2.13}$$

with the a priori unknown functions W_1 and W_2. Those functions contain information about the nucleon structure and – as we will see later – are in fact related to the structure functions and thereby to the parton distribution functions (PDFs). In Eq. (2.13) we have ignored terms antisymmetric in μ, ν, because they are not relevant in the unpolarized DIS process considered here.

Using the optical theorem based on the unitarity of the S matrix, one can establish a relation between the hadronic tensor and the forward Compton scattering amplitude $T_{\mu\nu}$,

$$W_{\mu\nu} = 2\,\mathrm{Im}\, T_{\mu\nu}, \tag{2.14}$$

$$T_{\mu\nu} = i\int d^4z\, e^{iq\cdot z}\,\langle p|\,\mathcal{T}\left[J^\mu(z)J^\nu(0)\right]|p\rangle\,, \tag{2.15}$$

where $\mathcal{T}\left[J^\mu(z)J^\nu(0)\right]$ is the time-ordered product of the currents $J^\mu(z)$ and $J^\nu(0)$. This relation is schematically illustrated in Fig. 2.2.

In Appendix 1 we will show that the phase space very close to the light cone, corresponding to $z^2 \to 0$, dominates the integral in Eq. (2.12), *i.e.*

$$W_{\mu\nu} \overset{\substack{Q^2\to\infty \\ x\ \text{finite}}}{\longrightarrow} \int d^4z\, e^{iq\cdot z}\,\langle p|\,[J^\mu(z), J^\nu(0)]\,|p\rangle\,\Big|_{z^2=0} \tag{2.16}$$

For $z^2 \to 0$ however the current product $J^\mu(z)J^\nu(0)$ is not well-defined. The proper way to treat it in the limit $z^2 \to 0$ is by means of the operator product expansion (OPE). The latter relates the product of composite operators separated by an infinitesimally small or a light-like distance to a sum over local operators multiplied by (possibly singular) coefficient functions. In Appendix

2 we demonstrate that at leading twist [2] for our case of unpolarized DIS the relevant operators are

$$\mathcal{O}^{\mu_1\mu_2\cdots\mu_{k+1}} = \bar{q}\gamma^{\{\mu_1}D^{\mu_2}\cdots D^{\mu_{k+1}\}}q. \tag{2.17}$$

$\mathcal{O}^{\mu_1\mu_2\cdots\mu_{k+1}}$ is a local twist-two operator, D is the covariant derivative and the braces indicate symmetrization and subtraction of the trace.

Local operators, more precisely nucleon matrix elements thereof, $\langle N|\mathcal{O}|N\rangle$, can be calculated in Euclidean quantum field theory and therefore lattice QCD calculations of of those matrix elements are possible. Of course in practice one cannot calculate the infinite tower of local operators appearing in expression (2.17). It is still possible to calculate the lowest terms, corresponding to the moments of parton distribution functions as we will see later.

To conclude the discussion let us emphasize that the light cone dominance makes it practically impossible to calculate parton distributions directly in Euclidean QFT, since the concept of a light cone is non-existent in Euclidean space-time. However, it allows for the operator product expansion, which makes a calculation of moments of the PDFs possible, because the OPE relates the moments of PDFs to matrix elements of local operators. Details are given in appendix 2.

2.2 Parton Distribution Functions and their Moments

Parton distribution functions are probability density functions. We can write the probability of finding a constituent p, *i.e.* a quark, an anti-quark or a gluon, in the nucleon which possesses a certain value of the Bjorken variable x (the longitudinal momentum fraction in the Bjorken limit) as $f_p(x)dx$. $f_p(x)$ is then called a parton distribution function (PDF). Note that the PDFs in principle also depend on Q^2, but the latter is typically used as the scale and thus serves as a parametrization. It is worthwhile mentioning that the scaling violation (the dependence on Q^2) is a consequence of higher order QCD corrections to the parton model, providing information about the gluon distribution and allow for the determination of the strong coupling constant α_s, since the corrections (logarithmically in Q) go like $\alpha_s(Q^2)/\pi$. To keep notation simple, instead of $f_p(x)$ we simply denote the PDFs $p(x)$, *i.e.* we use the symbol of the parton p (not to be confused with the momentum) for the corresponding PDF, *e.g.* $u(x)$, $\bar{u}(x)$ for the (anti-)u quark distribution function and $g(x)$ for the gluon distribution function. The quantum numbers of

[2] Twist is the sum of dimension and spin, which serves as an effective dimension of the operator. One expects that higher twist orders are strongly suppressed and this is confirmed by perturbative QCD calculations.

the proton give the following constraints:

$$\int_0^1 dx\ (u(x) - \bar{u}(x)) = 2, \tag{2.18}$$

$$\int_0^1 dx\ \left(d(x) - \bar{d}(x)\right) = 1, \tag{2.19}$$

$$\int_0^1 dx\ (q(x) - \bar{q}(x)) = 0 \quad \text{for} \quad q = s, c, b, t. \tag{2.20}$$

Moreover, the sum over all parton distributions must yield the momentum of the proton,

$$\int_0^1 dx\ x \left[\sum_{q \in \text{proton}} (q(x) + \bar{q}(x)) + g(x) \right] = 1. \tag{2.21}$$

Actually, the sum over the quark distributions gives about 0.5 which implies that half of the momentum of the proton is carried by gluons at typical energies about the GeV scale.

With relation (2.13) one is now equipped with the necessary tool to access the functions W_1 and W_2 experimentally. The functions $W_{1,2}$ and in fact all structure functions are related to parton distributions via coefficient functions that can be determined in perturbative QCD. Note that in polarized DIS, where the spin polarization of the electron and the proton is known, one can also access the spin distribution functions, moreover there are transverse momentum distribution functions, which are however hard to access in experiments.

In order to avoid a cumbersome derivation that can also be found in the standard literature (see for instance [4], section 18.5), we start with the operator definition of a (generalized) PDF via the light cone operator.

$$F_\Gamma(x, q^2) = \frac{1}{2} \int \frac{d\lambda}{2\pi} e^{ix\lambda} \langle p' | \bar{\psi}(-\lambda n/2) \Gamma \mathcal{P}\, e^{ig \int_{-\lambda/2}^{\lambda/2} d\alpha\, n \cdot A(n\alpha)} \psi(\lambda n/2) | p \rangle$$

$\mathcal{P}$ is the path ordering operator, n is a light-like vector (*i.e.* $n^2 = 0$) and F_Γ is a generalized parton distribution function that depends on the form of Γ. We use ψ and $\bar{\psi}$ to denote the quark field in order to avoid a confusion with the momentum transfer q. The right hand side can be related to matrix elements of local operators, as explained before. Parton distributions can be equivalently expressed by form factors. The form factor decomposition follows from the symmetry properties of QCD. As an example we show the form factor decomposition of a

matrix element of a local twist-two operator.

$$\langle N(p',s')|\mathcal{O}^{\mu\nu}|N(p,s)\rangle = \bar{U}_N(p',s')\left[A_{20}(q^2)\,\gamma^{\{\mu}P^{\nu\}} + B_{20}(q^2)\,\frac{i\sigma^{\{\mu\alpha}q_\alpha P^{\nu\}}}{2m_N} + C_{20}(q^2)\,\frac{1}{m_N}q^{\{\mu}q^{\nu\}}\right]U_N(p,s), \quad (2.22)$$

with the (generalized) form factors A_{20}, B_{20} and C_{20}. m_N is the mass of the nucleon and $U_N(p,s)$ is the on-shell nucleon spinor.

Form factors are more convenient for lattice QCD calculations because they are directly related to individual matrix elements of local operators and their momentum dependence. This corresponds to a calculation of the (momentum-dependent) moments of parton distributions, *e.g.* via the relation $A_{20}(0) = \langle x\rangle$.

The experimental determination of parton distributions works as follows. A more detailed overview can be found in Ref. [5] and the theoretical framework is explained in detail in Ref. [6]. Typically the PDFs are modeled using an ansatz that reproduces the expected behavior for $x \to 1$ and $x \to 0$. This behavior can be obtained from phenomenological models. Then a global fit to DIS data from experiments at particle accelerators is performed. This requires the evolution of the PDFs from some reference scale, typically of order 1 GeV, to a scale where pQCD is supposed to hold. Of course, one has the freedom of selecting the data and the details of the fit. There is an ongoing discussion between the groups performing those fits which is the preferred choice. The interested reader is referred to the work of the different groups that address the parton distributions [7, 5, 8, 9, 10]. We show as an example PDFs of the proton obtained at a scale $Q^2 = (2\text{ GeV})^2$ in Fig. 2.3. The functional form of the PDFs shown in the plot is given in [5], Eqs. (6) *ff*. For illustration we write here the fit ansätze used for the u and d quark distributions.

$$x(u-\bar{u})(x,Q^2) = A_u x^{\eta_1}(1-x)^{\eta_2}(1+\epsilon_u\sqrt{x}+\gamma_u x), \quad (2.23)$$

$$x(d-\bar{d})(x,Q^2) = A_d x^{\eta_3}(1-x)^{\eta_4}(1+\epsilon_d\sqrt{x}+\gamma_d x), \quad (2.24)$$

where all variables but x on the r.h.s. are fit parameters. One important note is that the phenomenological determination (combining pQCD and experiment) is based on the factorization theorem, basically stating that one can separate the long-distance dependence from the short-distance behavior. It is the theoretical confirmation that the OPE, where the matrix elements of the local operators contain the long-distance behavior and the short-distance behavior is incorporated in the coefficient functions, makes indeed sense.

In lattice QCD, all we need to do is to evaluate matrix elements of local operators of type

$$\mathcal{O}^{\mu_1\cdots\mu_n}(x) = \bar{q}(x)\Gamma^{\{\mu_1}D^{\mu_2}\cdots D^{\mu_n\}}q(x), \quad (2.25)$$

where $\Gamma_{\mu_0} = \gamma^\mu, \gamma^\mu\gamma_5$ and D is the covariant derivative and the braces mean symmetrization in the indices and subtraction of the trace, see also the discussion at the end of the previous section. We will show later that the calculation of those matrix elements basically amounts to

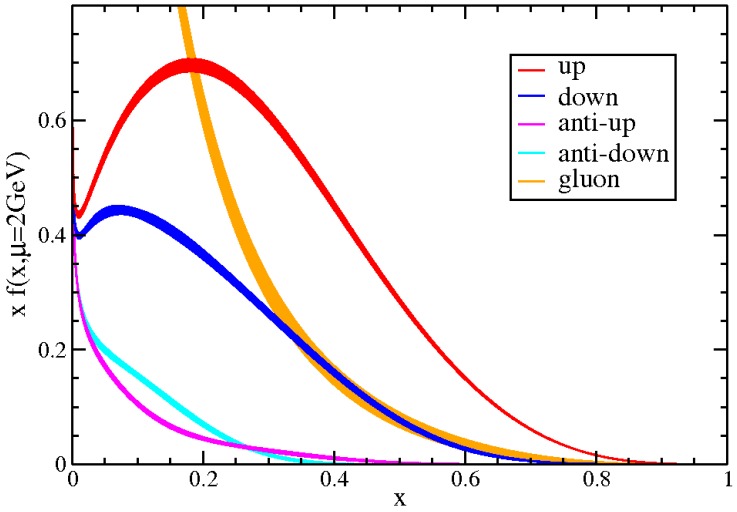

Figure 2.3: Parton distribution functions of the proton at $Q^2 = (2\ \text{GeV})^2$. The PDFs are taken from the MSTW PDFs library [5].

computing suitable ratios of nucleon 2-point and 3-point correlation functions. This can – at least theoretically – be done utilizing lattice QCD methods.

We are now prepared to discuss a few basic observables we deal with. Apart from the moments of PDFs, where we are actually only capable of computing some of the lowest non-trivial moments, we also introduce another matrix element in Sec. 2.3 which is not a PDF moment, namely the scalar quark content. It is a measure of the sensitivity of the nucleon mass to the quark mass and hence a measure of the influence of the individual quark flavors on the nucleon mass.

2.2.1 The Nucleon Axial Charge g_A

A simple but nonetheless important quantity related to hadron structure is the nucleon axial charge g_A. As we will see in the following discussion it plays a role in the neutron beta decay and is an important parameter in the chiral effective Lagrangian describing pion-nucleon interaction at low energies.

Consider the form factor decomposition of the matrix element of the axial isospin current $J^{5\,\mu a}(x) = \bar{q}(x)\gamma^\mu\gamma_5\tau^a q(x)$, where $q = (u,d)$ is the light quark doublet and τ is a Pauli matrix acting in flavor space.

$$\langle N(p',s')|J^{5\,\mu a}(0)|N(p,s)\rangle = \\ \bar{u}_N(p',s')\left[F_1^5(q^2)\,\gamma^\mu\gamma_5 + F_2^5(q^2)\,\frac{i\sigma^{\{\mu\nu}q_\nu P^{\nu\}}}{2m}\gamma_5 + F_3^5(q^2)\,q^\mu\gamma_5\right]\tau^a u_N(p,s) \quad (2.26)$$

This quantity enters the theory of the beta decay of the neutron. g_A is defined as $F_1^5(0)$m simply

because there is no fundamental conservation law that fixes the value of $F_1^5(0)$ trivially. In practice we can thus use a simplified definition,

$$\langle N(p,s)|\bar{q}(0)\gamma^\mu\gamma_5\tau^3 q(0)|N(p,s)\rangle = 2g_A s^\mu. \tag{2.27}$$

Note that with the definition of g_A it is also equivalent to say that g_A is the lowest (zeroth) moment of the polarized parton distributions (in isovector flavor combination), *i.e.* $g_A = \langle 1\rangle_{\Delta u - \Delta d}$.

The observable is quite precisely measured by experiments, with a current PDG value of $g_A = 1.2701(25)$ [11]. This is an accuracy of 2 per mill. Note that this is a world average, where most of the data comes from decay measurements on cold polarized neutrons. Therefore a comparison with lattice data, where no world average has been taken, has to be regarded with care.

The axial charge can also be calculated in a (chiral) effective theory. Under the assumption that the pion is massless we can write down an effective Lagrangian for the pion-nucleon interaction,

$$\mathcal{L} = ig_{\pi NN}\pi^a\bar{N}\gamma_5\sigma^a N, \tag{2.28}$$

where $g_{\pi NN}$ is the effective coupling of a pion to a nucleon. In this framework, g_A can be computed (assuming massless quarks) to give

$$g_A = \frac{f_\pi}{m_N} g_{\pi NN}. \tag{2.29}$$

This identity, known as Goldberger-Treiman relation [12], holds experimentally to about 5% accuracy, showing the predictive power of chiral perturbation theory for such quantities, see *e.g.* Ref. [13] for a review.

In lattice QCD g_A serves as a benchmark observable for nucleon structure calculations, because it can be straightforwardly computed from the nucleon matrix element of the simple local operator $\bar{q}\gamma^\mu\gamma^5\tau^3 q$. There is, however, a tension between experimentally measured values and lattice calculations of various collaborations. In fact, we are going to discuss this issue in detail in Chapter 7, since it is an important aspect of the work presented in this thesis. It is most important for the lattice QCD community to provide a value for g_A as the most easily accessible benchmark observable with fully controlled systematic errors, because only then it can be reliably compared to the experimental value.

2.2.2 The First Moment of the Unpolarized Parton Distribution $< x >_{u-d}$

Another observable being of particular interest is the first moment of the unpolarized parton distribution in isospin vector combination $\langle x \rangle_{u-d}$, defined

$$\int_0^1 dx\, x \left[(u(x) + \bar{u}(x)) - \left(d(x) + \bar{d}(x)\right) \right]. \tag{2.30}$$

Actually, it is the first non-trivial moment since the zeroth moment is fixed by the quantum numbers of the nucleon, here the number of valence quarks, that result in the constraints (2.18) *ff*.

Let us note in addition that, in terms of generalized form factors, $\langle x \rangle_{u-d} = A_{20}(0)$ with $A_{20}(q^2)$ from Eq. (2.22). A simplified definition as in the case of g_A, see the previous subsection, reads

$$\langle N(p,s)|\bar{q}(0)\gamma^{\{\mu} iD^{\nu\}}\tau^3 q(0)|N(p,s)\rangle\Big|_{\mu^2} = 2\langle x\rangle_{u-d}\Big|_{\mu^2} p^{\{\mu}p^{\nu\}}, \tag{2.31}$$

where the braces indicate symmetrization in the indices μ and ν and subtraction of the parts proportional to $g^{\mu\nu}$, and μ^2 is the scale at which the above expression is evaluated. A particular benefit for the lattice evaluation is – provided that the usual mass degenerate light quarks are employed and the fermion action respects isospin symmetry – the absence of quark disconnected contributions. The latter are known to be computationally demanding and their existence would make the lattice calculation of $\langle x \rangle_{u-d}$ more cumbersome. Thus, $\langle x \rangle_{u-d}$ can serve as another benchmark quantity to test the lattice QCD calculation of hadron structure. Let us note that we give first results for the isospin octet flavor combination $\langle x \rangle_{u+d-2s}$ including disconnected diagrams, which we discuss later.

As in the case of the axial charge g_A, there is a discrepancy between results from experiments and lattice calculations, however for $\langle x \rangle_{u-d}$ the tension is much bigger than for g_A. At this point, this statement shall just serve as a motivation for Chapter 7, where the issue is discussed in detail.

2.3 The Scalar Quark Content

Another quantity being of a different nature than the moments of PDFs discussed above also provides information about the inner structure of the nucleon: the scalar quark content of the nucleon. Mainly due to an increase of computer power and the development of special techniques, this observable has received increasing interest in the past few years, as a precise calculation of this quantity has become more feasible.

The scalar quark content of the nucleon is formally defined as $\langle N|\, \bar{q}q \,|N\rangle$, where $\bar{q}$ and q are quark fields of a certain (but the same) flavor. It is a measure of the sensitivity of the nucleon

mass to the quark mass, as can be seen from the following identity,

$$\langle N | \, \bar{q}q \, | N \rangle = \frac{\partial m_N}{\partial m_q}, \tag{2.32}$$

based on the Hellman-Feynman theorem [14]. As an immediate consequence, direct experimental measurements of the scalar quark content are not possible, simply because the quark mass cannot be varied. Note at this point that this restriction does not exist in lattice QCD, where the quark mass can in principle be chosen arbitrarily. Indirect measurements are still possible due to a relation of the scalar quark content to meson-nucleon scattering amplitudes. However, this method exhibits ambiguities and thus has large systematic uncertainties. This is reflected in the fact that the results of different groups differ significantly.
A theoretical prediction is therefore highly desirable. The non-perturbative nature of the scalar quark content suggests lattice QCD calculations. In fact there are two methods since both the right hand side and the left hand side of Eq. (2.32) can be evaluated individually using lattice methods.

The scalar quark content is particularly interesting for dark matter detection because it is an important ingredient in the cross section of the interaction of a weakly interactive massive particle (WIMP) – a promising dark matter candidate – with the nucleon mediated by a scalar particle, such as the recently discovered Higgs particle [15]. A diagram of the interaction is shown in Fig. 2.4.

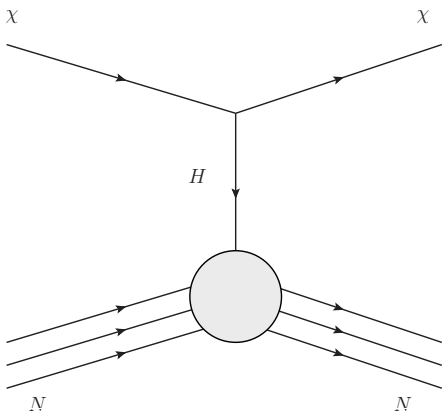

Figure 2.4: Interaction of a weakly interactive massive particle (WIMP), here denoted as χ, with a nucleon (N) mediated by the exchange of a Higgs-boson (H).

The cross section of such a process behaves like [16]

$$\sigma_{\chi N} \sim \left| \sum_q G_q(m_\chi^2) f_{T_q} \right|^2 , \tag{2.33}$$

$$f_{T_q} = \frac{m_q}{m_N} \langle N|\bar{q}q|N\rangle. \tag{2.34}$$

Here, the sum is over the quark flavors q. The function $G_q(m_\chi^2)$ depends on the particular details of the dark matter model, but certainly on the mass of the WIMP. f_{T_q} are dimensionless and renormalization group invariant couplings that depend on the quark flavor q and the mass m_q. We call the matrix element $\langle N|\bar{q}q|N\rangle$ the quark content of flavor q.

The strange quark contribution is expected to play an important role in the cross section (2.33) since the strange quark mass is more than one order of magnitude heavier than the light quark masses and the Higgs coupling is proportional to the quark mass. If the strange quark content $\langle N|\bar{s}s|N\rangle$ would be large compared to the light quark content, then the effects of the strange quark would be dominant in the cross-section. Note that the quark content of the heavier flavors might play an even more important role because their Higgs coupling is even stronger, but the quark content of the heavier flavors is also expected to be strongly suppressed compared to the three lightest flavors u, d and s, because already the c quark with a mass of about 1.6 GeV is heavier than the nucleon itself and hence difficult to generate in a virtual process.

In the literature (*e.g.* [17]) the observable of interest is the so-called pion-nucleon sigma term

$$\sigma_{\pi N} = \langle N|\, m_l \left(\bar{u}u + \bar{d}d\right) |N\rangle \,, \tag{2.35}$$

$$m_l = \frac{1}{2}\left(m_u + m_d\right), \tag{2.36}$$

where m_l is the average light quark mass. $\sigma_{\pi N}$ is a measure of the contribution of the non-vanishing light quark masses to the nucleon mass. A way to calculate $\sigma_{\pi N}$ is the extrapolation of the pion-nucleon scattering amplitude to the so-called Cheng-Dashen point [18]. Using a dispersion relation formula to analytically continue the (on-shell) pion-nucleon scattering amplitude to an un-physical region, contact to the sigma term can be made. The empirical value obtained with this method is $\sigma_{\pi N} = 79(7)$ MeV [19], a more recent result relying on baryon χPT is $\sigma_{\pi N} = 59(7)$ MeV [20]. We would like to remark here the the corresponding picture of the nucleon at low energy is the valence quarks surrounded by a cloud of (interacting) pions.

One can write the sigma term in a slightly more complicated fashion

$$\sigma_{\pi N} = \frac{\langle N|\, m_l \left(\bar{u}u + \bar{d}d - 2\bar{s}s\right) |N\rangle}{1-y}, \tag{2.37}$$

$$y = \frac{2\,\langle N|\,(\bar{s}s)\,|N\rangle}{\langle N|\,\left(\bar{u}u + \bar{d}d\right)\,|N\rangle}. \tag{2.38}$$

Here, the so-called y-parameter is a measure of the relative scalar strange quark content of the

nucleon and the observable of interest for phenomenological applications.
To leading order in baryon χPT the relation

$$y = \frac{m_l}{m_s - m_l} \left(m_\Xi + m_\Sigma - 2m_N \right) \tag{2.39}$$

holds in the SU(3) isospin limit. However, we cannot expect to have a reliable formula in this limit since of course the physical s quark is heavier than the physical light quarks by at least one order of magnitude. Therefore, at least one-loop corrections from χPT involving the pseudoscalar meson octet have to be included. Such a calculation gives $y = 0.44 \pm 0.13$ [21]. That is, y is not quite precisely determined, which emphasizes the necessity of a direct calculation. In Chapter 8 we present a calculation of the left hand side of Eq. (2.32), *i.e.* a direct calculation of matrix elements of the form $\langle N | \bar{q}q | N \rangle$. A noise reduction technique detailed in Sec. 5.7.2 allows us to present a result with unprecedented precision. Several systematic errors are not well-controlled in this calculation, but this is not the goal of the study presented in this thesis. We intend to demonstrate that a precise determination of scalar matrix elements is feasible with the method we use.

3 Correlation Functions in Euclidean Field Theory

In order to understand the details of the lattice calculations which we present in the chapters 6 to 8, we need to establish a theoretical basis. In this chapter we therefore describe the field-theoretical aspects of the calculations, whereas in chapters 4 and 5 we concentrate on the aspects specific to lattice QCD.

In euclidean field theory matrix elements $\langle N|\mathcal{O}|N\rangle$ of local operators $\mathcal{O}$, say $\bar{q}\Gamma q$ or a twist-two operator [see Eq. (2.25)], are given as limit of large time separations of appropriate ratios of 2-point and 3-point correlation functions of the nucleon. This is described in Sec. 3.3, the correlation functions are explained in the two subsequent sections. We start discussing the nucleon 2-point function in Sec. 3.1 before we address the more complicated 3-point function in Sec. 3.2. Sec. 3.4 is concerned with excited state effects arising from finite time separations in the correlation functions. We specify the nucleon field in Sec. 3.5, with which we can write the correlation functions in terms of quark propagators, *i.e.* Wick contractions of the fundamental quark fields. Eventually, in Sec. 3.6 we deal with renormalization.

3.1 Nucleon 2-point Correlation Functions

The basic nucleon 2-point function is a Green function defined as

$$\begin{aligned} C_2^{\alpha'\alpha}(x',x) &= \langle\Omega|\, N_{\alpha'}(x')\bar{N}_{\alpha}(x)\,|\Omega\rangle \\ &= \frac{\int \mathcal{D}U\ \mathcal{D}(\bar{\psi}\psi)\ \exp\left(-S[U,\bar{\psi},\psi]\right) N_{\alpha'}(x')\bar{N}_{\alpha}(x)}{\int \mathcal{D}U\ \mathcal{D}(\bar{\psi}\psi)\ \exp\left(-S[U,\bar{\psi},\psi]\right),} \end{aligned} \tag{3.1}$$

where $|\Omega\rangle$ is the QCD vacuum state and the integral $\int \mathcal{D}U\ \mathcal{D}(\bar{\psi}\psi)$ has to be understood as the usual path integral over the gauge field and the fermionic content of the theory, here being the quark fields $\bar{q}$ and q, summed over all flavors. The indices α and α' refer to the Dirac structure of the nucleon, since it is a spin-$\frac{1}{2}$ particle that is represented by the 4-component spinor field $N_\alpha(x)$ constructed such that it carries the quantum numbers of the nucleon, see Sec. 3.5 for an explicit definition of the nucleon interpolating field used in the lattice QCD calculations presented in this thesis. Note that we have used the integration over the elements U_μ of the $\mathrm{SU}(3)$ gauge group rather than the integration over the gauge fields A_μ being themselves elements of the algebra $\mathrm{su}(3)$. This is equivalent but more applicatory in anticipation of the formulation of the theory on the lattice, see Chapter 4.

We refer to $x = (\vec{x}, t)$ as the source position and $x' = (\vec{x}', t')$ as the sink position. $t' - t$ is usually called source-sink separation, even if it is just the euclidean time component thereof. We always assume $t < t'$, since we have suppressed a time ordering in Eq. (3.1).

Translational invariance implies that $C_2^{\alpha'\alpha}(x', x)$ can in fact only be a function of $x' - x$. We account for this circumstance by setting x to zero for convenience and drop it from the expressions. The dependency on x can however be restored by the simple replacement $x' \to (x' - x)$. In addition, for convenience we often write the spatial and the temporal components of x' explicitly, that is

$$C_2^{\alpha'\alpha}(x', 0) = C_2^{\alpha'\alpha}(\vec{x}', t', 0) \equiv C_2^{\alpha'\alpha}(\vec{x}', t'). \tag{3.2}$$

Now, for practical reasons – we want to resolve a momentum dependence of the matrix elements – let us introduce a *momentum-projected* 2*-point function*, where the spatial $\vec{x}'$ dependence has been transformed by a Fourier transformation and we are left with a momentum dependence:

$$C_2^{\alpha'\alpha}(\vec{p}, t') = \int d^3x' \; e^{-i\vec{p}\cdot\vec{x}'} \; C_2^{\alpha'\alpha}(\vec{x}', t') \tag{3.3}$$

Applying the transfer matrix formalism we can derive a spectral representation of the 2-point function,

$$C_2^{\alpha'\alpha}(\vec{p}, t') = \sum_n \frac{1}{2E_{\vec{p}}^{(n)}} \, e^{-E_{\vec{p}}^{(n)} t'} \; \langle \Omega | \, N_{\alpha'} \, | n, \vec{p} \rangle \, \langle n, \vec{p} | \, \bar{N}_\alpha \, | \Omega \rangle \tag{3.4}$$

$$= \sum_n \frac{|Z_n|^2}{2E_{\vec{p}}^{(n)}} \, e^{-E_{\vec{p}}^{(n)} t'} \; \left(p^{(n)} \cdot \gamma + m_n \right)_{\alpha'\alpha}. \tag{3.5}$$

The sum is over states the nucleon field couples to, *i.e.* states with the same quantum numbers as the nucleon[1]. $E_{\vec{p}}^{(n)}$ is the energy of the n^{th} eigenstate with momentum $\vec{p}$, *i.e.* $e^{-Ht}|n, \vec{p}\rangle = e^{-E_{\vec{p}}^{(n)} t}|n, \vec{p}\rangle$. In the last line we have used the relations

$$\langle \Omega | \, N_{\alpha'} \, | n, \vec{p} \rangle = Z_n \, U_{\alpha'}(p^{(n)}, s), \tag{3.6}$$

$$\sum_s U_{\alpha'}(p, s) \, \bar{U}_\alpha(p, s) = (p \cdot \gamma + m)_{\alpha'\alpha}. \tag{3.7}$$

The factor Z_n in Eq. (3.6) is a measure how much of the state $|n, \vec{p}\rangle$ is created by the field $N_{\alpha'}$. Eq. (3.7) is the spin sum completeness relation for spinors. Actually, we have suppressed the sum over the spin s in Eq. (3.4) for better readability. Note that Eq. (3.4) holds only for $0 < t'$, since we have implicitly used of a time-ordered product as mentioned above. The sum in the spectral representation of the momentum-projected 2-point correlation function, Eq. (3.4), is

[1] We assume that there are no degenerate states.

clearly dominated by the ground state energy, in the limit $t' \to \infty$,

$$C_2^{\alpha'\alpha}(\vec{p}, t') \overset{t'\to\infty}{\longrightarrow} \frac{|Z_0|^2}{2E_{\vec{p}}^{(0)}} e^{-E_{\vec{p}}^{(0)} t'} \left(p \cdot \gamma + m_N\right)_{\alpha'\alpha}, \tag{3.8}$$

which allows to extract at zero momentum the ground state mass from the exponential decay at large source-sink separation. Note that it is possible, but more demanding, to extract the energies of the higher energy states. A sound method to do so is outlined in Sec. 5.7.3.

Typically, one is not interested in the particular spin structure of C_2. Thus, the Dirac trace of C_2 times an appropriate combination of γ matrices, here referred to as Γ, is taken,

$$\begin{aligned} C_2^{\Gamma}(\vec{p}, t') &= \Gamma_{\alpha\alpha'} C_2^{\alpha'\alpha}(\vec{p}, t') \\ &\equiv \text{Tr}\left[\Gamma C_2(\vec{p}, t')\right]. \end{aligned} \tag{3.9}$$

We call this trace over the 2-point function *spin-projected 2-point function*. The trace only acts in Dirac space on $p \cdot \gamma + m_N$, hence the form of the spectral representation does not change but depending on the particular form of Γ, we have different traces, *e.g.*

$$\begin{aligned} \text{Tr}\left[1\left(p \cdot \gamma + m_N\right)\right] &= 4m_N, \\ \text{Tr}\left[\gamma^\mu\left(p \cdot \gamma + m_N\right)\right] &= 4p^\mu. \end{aligned}$$

For the scope of this thesis the only ones used for the 2-point function, are the combinations $\Gamma^\pm \equiv \frac{1}{2}(1 \pm \gamma_0)$. Those project on the parity-plus and parity-minus states.

3.2 Nucleon 3-point Correlation Functions

In this section we define a nucleon 3-point correlation function,

$$C_3^{\alpha'\alpha}(x', y, x) = \qquad = \frac{\int \mathcal{D}U\, \mathcal{D}(\bar{\psi}\psi)\, \exp\left(-S[U, \bar{\psi}, \psi]\right) N_{\alpha'}(x') \mathcal{O}(y) \bar{N}_\alpha(x)}{\int \mathcal{D}U\, \mathcal{D}(\bar{\psi}\psi)\, \exp\left(-S[U, \bar{\psi}, \psi]\right)}, \tag{3.10}$$

with the same conventions as used in the definition of the nucleon 2-point correlation function [see Eq. (3.1)]. In general the operator $\mathcal{O}(y)$ (to be understood as composite field) carries Dirac and may even carry color indices, however those have to be properly contracted, as we show in Sec. 3.5. For better readability we suppress them here. Translational invariance implies that the 3-point function is only a function of the distances $x' - y$ and $y - x$. Consequently, in analogy to the 2-point case, we set the source point x to zero and remark that the x dependency can be restored by replacing $y \to (y - x)$ and $x' \to (x' - x)$ in all expressions. Moreover, we split the spatial and the temporal components of the coordinates x' and y,

$$C_3^{\alpha'\alpha}(x', y, 0) \equiv C_3^{\alpha'\alpha}\left(\vec{x}' - \vec{y}, t' - \tau, \vec{y}, \tau\right) \tag{3.11}$$

where we denote the point of the operator insertion with $y = (\vec{y}, \tau)$. Note that we implicitly assume $0 < \tau < t'$ due to time ordering, in analogy to the 2-point function.

Actually, the term nucleon 3-point function may appear misleading, since it does not involve the nucleon field at three different space-time points but only two nucleon fields and the operator. However, following standard practice we use the term 3-point function consistently in the course of this thesis.

As in the case of the 2-point correlation function we define a momentum-projected 3-point function, where now the two spatial dependencies $\vec{x}' - \vec{y}$ and $\vec{y}$ are traded for two momentum dependencies via two Fourier transformations,

$$C_3^{\alpha'\alpha}(\vec{p}', t' - \tau, \vec{p}, \tau) = \int d^3x'\ d^3y\ e^{-i\vec{p}'\cdot(\vec{x}'-\vec{y})}\ e^{-i\vec{p}\cdot\vec{y}} \times \\ \times\, C_3^{\alpha'\alpha}(\vec{x}' - \vec{y}, t' - \tau; \vec{y}, \tau). \tag{3.12}$$

The spectral representation of the 3-point function can be straightforwardly derived from the transfer matrix formalism to give

$$C_3^{\alpha'\alpha}(\vec{p}', t' - \tau, \vec{p}, \tau) = \sum_{n,m} \frac{Z_n Z_m^*}{2E_{\vec{p}'}^{(n)} 2E_{\vec{p}}^{(m)}}\ e^{-E_{\vec{p}}^{(n)}(t'-\tau)}\ e^{-E_{\vec{p}}^{(m)}\tau} \\ \times \left[\left(p'^{(n)} \cdot \gamma + m_n \right) \mathcal{O}_{nm} \left(p^{(m)} \cdot \gamma + m_m \right) \right]_{\alpha'\alpha}. \tag{3.13}$$

Analogously to the case of the 2-point function case [*cf.* Eq. (3.9)], we define a spin-projected 3-point function

$$C_3^{\Gamma}(\vec{p}', t' - \tau, \vec{p}, \tau) = \mathrm{Tr}\left[\Gamma C_3(\vec{p}', t' - \tau, \vec{p}, \tau) \right], \tag{3.14}$$

where again Γ is an appropriate combination of γ matrices. The spectral decomposition is basically the same as for the full 3-point function, Eq. (3.13), but the trace applies to Γ times the expression in square brackets. $\mathcal{O}_{nm}$ is the matrix element $\langle n|\mathcal{O}|m\rangle$ of the operator $\mathcal{O}$ between two energy eigenstates. With regard to its form factor decomposition (*cf.* Eq. (2.22)) it is evident that the choice of Γ is crucial if one wants to calculate the full matrix element. One may even want to keep the full Dirac structure of the 3-point function and not take the trace, in order to access all the form factors.

It is worthwhile considering the asymptotic limit $t' - \tau \to \infty$, $\tau \to \infty$ of Eq. (3.13) since apparently the exponential decay for large times is dominated by the nucleon mass being the lowest energy level at zero momentum,

$$C_3^{\alpha'\alpha}(\vec{p}', t' - \tau, \vec{p}, \tau) \overset{\substack{(t'-\tau)\to\infty \\ \tau\to\infty}}{\longrightarrow} \frac{|Z_0|^2}{2E_{\vec{p}'}^{(0)}\ 2E_{\vec{p}}^{(0)}} e^{-E_{\vec{p}'}^{(0)}(t'-\tau)}\ e^{-E_{\vec{p}}^{(0)}(\tau)} \times \\ \times \left[\left(p' \cdot \gamma + m_N \right) \mathcal{O}_{00} \left(p \cdot \gamma + m_N \right) \right]_{\alpha'\alpha}. \tag{3.15}$$

This fact makes it possible to extract the wanted nucleon matrix elements, here denoted $\mathcal{O}_{00}$. In order to dispose of the unwanted and unknown prefactors we can combine 3-point and 2-point correlation functions in ratios, as we demonstrate in the subsequent section.

3.3 Nucleon Matrix Elements in Euclidean Field Theory

The matrix element $\mathcal{O}_{00} \equiv \mathcal{O}_{NN}$ in Eq. (3.13) is a nucleon matrix element of the (local) Operator $\mathcal{O}$ that gives information about the nucleon structure, corresponding to certain form factors. More precisely, we can obtain generalized form factors from the form factor decomposition. For example, if $\mathcal{O}$ is a local twist-two operator, we can obtain the moments of parton distributions or the form factors of the respective form factor decomposition from the matrix element.

The asymptotic limits of the 2-point and 3-point correlation functions, Eq. (3.8) and Eq. (3.15), suggest that we can cancel the unwanted Z_N factors as well as any t',τ or t dependence, by building appropriate ratios of 3-point and 2-point functions.

As a first step – for better comprehension – let us consider the special case $p' = p$. In fact, in the asymptotic limit $t' - \tau \to \infty$, $\tau \to \infty$ and consequently $t' \to \infty$, the ratio of the 3-point and the 2-point yields [*cf.* Eq. (3.15) and Eq. (3.8)]

$$\frac{C_3^{\tilde{\Gamma}}(\vec{p}, t' - \tau, \vec{p}, \tau)}{C_2^{\Gamma}(\vec{p}, t')} \to \frac{\mathrm{Tr}\,\left[\tilde{\Gamma}\,(p\cdot\gamma + m_N)\,\mathcal{O}_{NN}\,(p\cdot\gamma + m_N)\right]}{2E_{\vec{p}}\ \mathrm{Tr}\,\left[\Gamma\,(p\cdot\gamma + m_N)\right]}, \tag{3.16}$$

from which we can easily obtain the matrix element $\mathcal{O}_{NN}$ by dividing out the known kinematic factors. Note that the Γ matrices do not necessarily need to be the same in the projected 3-point function and for the projected 2-point function. We indicate this by using $\tilde{\Gamma}$ and Γ in Eq. (3.16).

In the general case where the momenta p' and p are different, the ratio that cancels the unwanted factors is not so easy to figure out, but with some algebra we obtain

$$\frac{C_3^{\tilde{\Gamma}}(\vec{p}', t' - \tau; \vec{p}, \tau)}{C_2^{\Gamma}(\vec{p}', t')} \sqrt{\frac{C_2^{\Gamma}(\vec{p}, t' - \tau)\ C_2^{\Gamma}(\vec{p}', \tau)\ C_2^{\Gamma}(\vec{p}', t')}{C_2^{\Gamma}(\vec{p}', t' - \tau)\, C_2^{\Gamma}(\vec{p}, \tau)\, C_2^{\Gamma}(\vec{p}, t')}} \to \frac{\mathrm{Tr}\,\left[\tilde{\Gamma}\,(p'\cdot\gamma + m_N)\,\mathcal{O}_{00}\,(p\cdot\gamma + m_N)\right]}{2\sqrt{E_{\vec{p}}E_{\vec{p}'}\ \mathrm{Tr}\,\left[\Gamma\,(p'\cdot\gamma + m_N)\right]\ \mathrm{Tr}\,\left[\Gamma\,(p\cdot\gamma + m_N)\right]}}. \tag{3.17}$$

Thus we have demonstrated that the matrix element of a local operator can be obtained by building appropriate ratios of 3-point and 2-point functions.

However, if the asymptotic limit of large time separations cannot be attained – as is the case in all practical calculations of lattice QCD where we have to restrict to a finite lattice – corrections from states with higher energy and mass than the nucleon arise. This problem, denoted as excited state contributions, requires a special treatment and is discussed in Sec. 3.4. A dedicated analysis of this effect is an important aspect of this thesis work.

3.4 Excited State Contributions at Finite Source-Sink Separation

Let us now discuss the corrections that arise when the asymptotic limit of infinitely large time separations [*cf.* Eq. (3.16) and Eq. (3.17)] cannot be reached. In lattice QCD calculations this is always the case since computing resources are always finite and so must be the spatial and temporal extent of the lattice.

Consider the spectral decomposition of the nucleon 2-point function, Eq. (3.4). The arguments made here essentially depend on the exponential factors appearing in the spectral decomposition and not on the particular spin structure, hence we take the spin-projected 2-point function, to keep notation simple.
We would like to know the leading corrections at finite source-sink separation t'. To this end we write the first terms in the sum over energy eigenstates $|n\rangle$ explicitly,

$$\begin{aligned} C_2^\Gamma(\vec{p}, t'; \vec{x} = 0) = &\frac{|Z_0|^2}{2E^0}\, e^{-E_0 t')}\, \mathrm{Tr}\, \left[\Gamma \left(p^{(0)} \cdot \gamma + m_N\right)\right] \\ &+ \frac{|Z_1|^2}{2E^1}\, e^{-E_1 t'}\, \mathrm{Tr}\, \left[\Gamma \left(p^{(1)} \cdot \gamma + m_1\right)\right] + \cdots , \end{aligned} \tag{3.18}$$

where we always understand E_i as $E_{\vec{p}}^{(i)}$, the energy of the i^{th} state with momentum $\vec{p}$. Recall that $E_0 < E_1 < E_2 < \cdots$, so 0 labels the nucleon being the lowest energy state. For simplicity let us combine the terms that do not depend on t' in constants

$$f_i^\Gamma = \frac{|Z_i|^2}{2E^i}\, \mathrm{Tr}\, \left[\Gamma \left(p^{(i)} \cdot \gamma + m_i\right)\right]. \tag{3.19}$$

Actually, those constants are parametrized by the mass of the eigenstate, the momentum $\vec{p}$ as well as the choice of Γ. We drop the superscript Γ from the expressions for the rest of this section, since it is not important for the discussion here. The expression in Eq. (3.18) has to be compared to the asymptotic limit, Eq. (3.8). Therefore we factor out the asymptotic limit and obtain

$$\begin{aligned} C_2(\vec{p}, t') = &f_0\, e^{-E_0 t'} \\ &\times \left(1 + \frac{f_1}{f_0}\, e^{-E_{01} t'} + \frac{f_2}{f_0}\, e^{-E_{02} t'} + \cdots\right), \end{aligned} \tag{3.20}$$

where we have introduced the energy differences $E_{ij} = E_j - E_i$. For the remainder of the discussion let us assume that the terms with $e^{-E_{0i} t'}$, $(i \geq 2)$ are small compared to the one with $e^{-E_{01} t'}$. This is the case if E_{12} is sufficiently large and f_2 is at least not much greater than f_1. Therefore the leading excited state contribution relative with respect to the asymptotic limit is $f_1/f_0\ e^{-E_{01} t'}$, which vanishes exponentially with t'. That is why in principle they can be neglected for $t' \gg 1/E_{01}$, but in practice one typically has $t' \gtrsim c/E_{01}$, where c is a constant that is not much bigger than one. The consequences are discussed in Sec. 7.4, were some more details are given how such situations can be treated.

Additionally, if the ratio f_1/f_0 is large, which can be the case if the nucleon interpolating field couples much stronger to the first excited state than to the ground state (the nucleon), the contribution from the first excited state can be sizable even for moderately large source-sink separations. Therefore in most cases it is desirable to have an interpolating field that couples strongly to the ground state and only little to the higher energy states.

Let us now consider the spin-projected 3-point function. With the double sum written explicitly, its spectral representation reads

$$\begin{aligned} C_3^\Gamma(\vec{p}', t'-\tau, \vec{p}, \tau) = f_{00}\, e^{-E_0 t'} + f_{01}\, e^{-E_0(t'-\tau)}\, e^{-E_1 \tau} \\ + f_{10}\, e^{-E_1(t'-\tau)}\, e^{-E_0 \tau} + f_{11}\, e^{-E_1 t'} \\ + \cdots, \end{aligned} \tag{3.21}$$

where introduce the constants

$$f_{ij} = \frac{Z_i}{2E^i} \frac{Z_j^*}{2E^j} \operatorname{Tr}\left[\Gamma\left(p'^{(i)} \cdot \gamma + m_i\right) \mathcal{O}_{ij} \left(p^{(j)} \cdot \gamma + m_j\right)\right]. \tag{3.22}$$

f_{ij} depend on the momenta $\vec{p}$ and $\vec{p}'$ as well as the masses of the states i and j and in addition on the matrix element $\mathcal{O}_{ij}$. We assume that $f_{ij} \lesssim f_{00}$ so that we can focus our discussion on the exponential dependencies of the time separations.

In terms of the asymptotic limit, the series in Eq. (3.21) reads

$$\begin{aligned} C_3^\Gamma(\vec{p}', t'-\tau, \vec{p}, \tau) = f_{00}\, e^{-E_0 t'} \\ \times \left(1 + \frac{f_{01}}{f_{00}}\, e^{-E_{01}\tau} + \frac{f_{10}}{f_{00}}\, e^{-E_{01}(t'-\tau)} + \frac{f_{11}}{f_{00}}\, e^{-E_{01} t'}) + \cdots\right), \end{aligned} \tag{3.23}$$

so the leading contributions fall of exponentially with $e^{-E_{01}\Delta t}$, where $\Delta t = \tau, t'-\tau$ or t'. In most practical applications however τ is more or less in the middle between source and sink, *i.e.* $\tau \approx t'/2$. The reasoning is that τ and $(t'-\tau)$ have to be sufficiently large and since $0 < \tau < t'$, τ cannot be too close to either source or sink time slice. As a consequence the contribution with $e^{-E_{01} t'}$ is approximately quadratically suppressed compared to the contributions with $e^{-E_{01}\tau}$ and $e^{-E_{01}(t'-\tau)}$, of which the exponential decay goes roughly like $e^{-E_{01} t'/2}$.
In the more general case where τ is not centered between source and sink the statement that the contribution with $e^{-E_{01} t'}$ is smaller than the others appearing in Eq. (3.23) still holds, provided that but τ is not too close to either source or sink. For our qualitative discussion here, we ignore those contributions.
Note that in this case in order to be consistent we also ignore the leading contribution to the 2-point function [see Eq. (3.20)], because its exponential decrease is the same, namely $e^{-E_{01} t'}$. Thus, the leading contributions to the ratio of a 3-point and a 2-point function, from which we

extract the matrix element of interest [see Eq. (3.16)], are

$$\frac{C_3^{\tilde{\Gamma}}(\vec{p}, t'-\tau; \vec{p}, \tau)}{C_2^{\Gamma}(\vec{p}, t')} = \frac{C_3^{\tilde{\Gamma}}(\vec{p}, (t'-\tau)=\infty; \vec{p}, \tau=\infty)}{C_2^{\Gamma}(\vec{p}, t'=\infty)} \times \left(1 + \frac{f_{01}}{f_{00}}\, e^{-E_{01}(\tau)} + \frac{f_{10}}{f_{00}}\, e^{-E_{01}(t'-\tau)}\right). \tag{3.24}$$

3.5 Nucleon Field

In the previous sections we have not specified the particular form of the nucleon interpolating field. While – as mentioned before – the only theoretical requirement is a coupling to the nucleon state at all (more precisely to the physical nucleon wave function), in practice we would like this coupling to be as big as possible. The reasoning is that the asymptotic limit of infinitely large time separations [*cf.* Eqs. (3.8) and (3.15)] cannot be performed. Therefore states with higher energy contribute as discussed in Sec. 3.4. In order to reduce the influence of these so-called excited states one can choose a field that couples strongly to the nucleon and only little to the excited states, that is $\langle\Omega|N|i\rangle \ll \langle\Omega|N|0\rangle$ for $i \geq 1$.

The nucleon is a composite particle and hence we can build its interpolating field from the basic quark and gluon fields in such a way that all quantum numbers are equal to those of the nucleon. Those quantum number are baryon number, parity, spin and isospin (valence quark content). Often the simple interpolating field, here for the case of the proton,

$$N_\alpha(x) = \varepsilon^{\mathrm{abc}} u_\alpha^{\mathrm{a}}(x) \left(d^{\mathrm{b}\,\mathrm{T}}(x) \mathcal{C}\gamma_5 u^{\mathrm{c}}(x)\right) \tag{3.25}$$

is used. Here, $C = i\gamma_0\gamma_2$ is the charge conjugation operator and the transpose only acts in Dirac space. The corresponding neutron interpolating field reads

$$N_\alpha(x) = \varepsilon^{\mathrm{abc}} d_\alpha^{\mathrm{a}}(x) \left(u^{\mathrm{b}\,\mathrm{T}}(x) \mathcal{C}\gamma_5 d^{\mathrm{c}}(x)\right). \tag{3.26}$$

Let us now have a closer look at the nucleon correlation functions from the previous chapter. With the form of the nucleon field specified as in Eq. (3.25), we can now write down the correlation functions in terms of Wick contractions of the quark fields.
To this end, let us write the proton field with all indices explicitly,

$$N_\alpha(x) = \zeta_{\alpha BCD}\; u^B(x) d^C(x) u^D(x), \tag{3.27}$$
$$\bar{N}_\alpha(x) = \bar{\zeta}_{\alpha BCD}\; \bar{u}_B(x) \bar{d}_C(x) \bar{u}_D(x), \tag{3.28}$$

where we have replaced the Dirac structure in Eq. (3.25) by the symbol ζ,

$$\zeta_{\alpha BCD} = \varepsilon^{bcd} \delta_{\alpha\beta} \left(\mathcal{C}\gamma_5\right)_{\gamma\delta}, \quad \bar{\zeta}_{\alpha BCD} = \varepsilon^{dcb} \left(\mathcal{C}\gamma_5\right)_{\delta\gamma} \delta_{\beta\alpha} \tag{3.29}$$

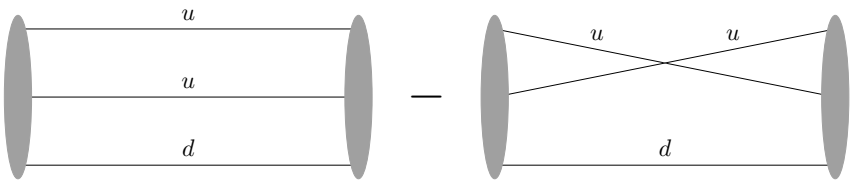

Figure 3.1: Schematic representation of the proton 2-point function contraction pattern.

and combined the Greek letters for Dirac indices and the small Roman letters into capital Roman letters, *i.e.* $B = (\beta, b)$, $C = (\gamma, c)$ and $D = (\delta, d)$. This allows us to focus on the more fundamental structure of the correlation functions and not become confused by the amount of indices.

In this notation, the proton 2-point correlation function (*cf.* Eq. (3.1)) reads

$$C_2^{\alpha'\alpha}(x', x) = \int \mathcal{D}U \ \det M[U] \ e^{-S_g[U]} \ \bar{\zeta}_{\alpha' B' C' D'} \zeta_{\alpha B C D} \times \left\langle \bar{u}_{B'}(x') \bar{d}_{C'}(x') \bar{u}_{D'}(x') u_B(x) d_C(x) u_D(x) \right\rangle_{S_f}, \quad (3.30)$$

up to normalization by the partition function, which we consider absorbed in the path integral measure in the following for an easier notation. In the above expression, $\det M[U] = \int \mathcal{D}(\bar{\psi}\psi) \ e^{-S_f[U]}$ formally replaces the integration over the quark degrees of freedom in the background of the gauge field U. S_g is the pure gauge part of the QCD action and S_f is the fermionic part of the action. We discuss this in more detail when introducing lattice QCD in Chapter 4, since M can only be strictly defined in the discretized theory. Here, it shall only serve the purpose of an easier notation. Note that the source point x is not fixed to zero as usual when we write correlation functions, since this coordinate appears explicitly in the quark fields.
Wick's theorem states we have to contract all possible quark fields and respect that Grassmann numbers anti-commute, which gives

$$C_2^{\alpha'\alpha}(x', x) = \int \mathcal{D}U \ \det M[U] \ e^{-S_g[U]} \ \bar{\zeta}_{\alpha' B' C' D'} \zeta_{\alpha B C D} \times \Big\{ \left[\bar{u}_{B'}(x') u_B(x)\right]_U \left[\bar{d}_{C'}(x') d_C(x)\right]_U \left[\bar{u}_{D'}(x') u_D(x)\right]_U - \left[\bar{u}_{B'}(x') u_D(x)\right]_U \left[\bar{d}_{C'}(x') d_C(x)\right]_U \left[\bar{u}_{D'}(x') u_B(x)\right]_U \Big\} \quad (3.31)$$

This contraction pattern is illustrated in Fig. 3.1. The contraction $[\bar{u}(x')u(x)]_U$ is the quark propagator in the background of the gauge fields U. It is addressed in more detail in Chapter 4.

For the 3-point the contraction looks slightly more complicated, because we have two addi-

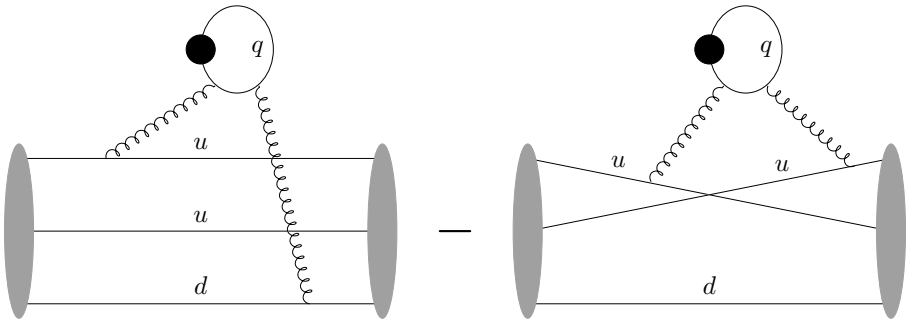

Figure 3.2: Contraction pattern of the disconnected piece of the proton 3-point function local operator of type $\bar{q}Xq$, where q is the quark field of the flavor of interest. The helical lines indicate that interactions are mediated by gluons only. The filled black circle represents the operator insertion.

tional quark fields we can contract with the others.

$$C_3^{\alpha'\alpha}(x',y,x) = \int \mathcal{D}U \ \det M[U]\, e^{-S_g[U]}\, \bar{\zeta}_{\alpha' B' C' D'} \zeta_{\alpha B C D} \times \bar{u}_{B'}(x') \bar{d}_{C'}(x') \bar{u}_{D'}(x') \bar{q}_{E'}(y) O_{E'E} q_E(y) u_B(x) d_C(x) u_D(x) \quad (3.32)$$

Here, the O has to be thought of as say a γ matrix or (the kernel of) a twist-two operator. The contraction pattern now depends on the flavor of the fields q and $\bar{q}$. In all cases there are quark-disconnected contractions,

$$C_3^{\alpha'\alpha}(x',y,x)\Big|_{DISC} = \int \mathcal{D}U \ \det M[U]\, e^{-S_g[U]}\, \bar{\zeta}_{\alpha' B' C' D'} \zeta_{\alpha B C D} \times [\bar{q}_{E'}(y) q^e_E(y)]_{U_\mu} O^{e'e}_{E'E} \Big\{ \left[\bar{u}_{B'}(x') u_B(x)\right]_U \left[\bar{d}_{C'}(x') d_C(x)\right]_U \left[\bar{u}_{D'}(x') u_D(x)\right]_U - \left[\bar{u}_{B'}(x') u_D(x)\right]_U \left[\bar{d}_{C'}(x') d_C(x)\right]_U \left[\bar{u}_{D'}(x') u_B(x)\right]_U \Big\}. \quad (3.33)$$

The interaction between the separated (dis-connected) pieces of these propagators are solely through the gluon fields which makes this quantity hard to measure compared to a quantity that has only connected contributions, see below. The contraction pattern of the disconnected piece of a proton 3-point function, Eq. (3.33), is illustrated in Fig. 3.2.

Let us now consider the connected piece of the 3-point function. For the interpolating field Eq. (3.27) connected diagrams can only arise if $q = u, d$. The simpler of both cases is $q = d$. In

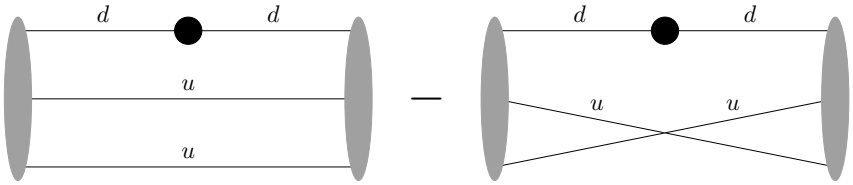

Figure 3.3: Contraction pattern of the connected piece of the proton 3-point function involving a local operator of type $\bar{d}Xd$. The operator insertion is represented by a filled black circle.

this case the contractions, illustrated in in Fig. 3.3, read

$$\begin{aligned} C_3^{\alpha'\alpha}(x',y,x)\Big|_{CONN} = \int \mathcal{D}U \ \det M[U]\ e^{-S_g[U]}\ \bar{\zeta}_{\alpha' B' C' D'}\zeta_{\alpha BCD} \\ \times O_{E'E}\Big\{ \left[\bar{u}_{B'}(x')u_B(x)\right]_U \left[\bar{d}_{C'}(x')d_E(y)\right]_U \left[\bar{d}_{E'}(y)d_C(x)\right]_U \left[\bar{u}_{D'}(x')u_D(x)\right]_U \\ - \left[\bar{u}_{B'}(x')u_D(x)\right]_U \left[\bar{d}_{C'}(x')d_E(y)\right]_U \left[\bar{d}_{E'}(y)d_C(x)\right]_U \left[\bar{u}_{D'}(x')u_B(x)\right]_U .\Big\} \end{aligned} \tag{3.34}$$

If the quark field of the operator is of up (u) flavor, we can write down four connected contractions,

$$\begin{aligned} C_3^{\alpha'\alpha}(x',y,x)\Big|_{CONN} = \int \mathcal{D}U \ \det M[U]\ e^{-S_g[U]}\ \bar{\zeta}_{\alpha' B' C' D'}\zeta_{\alpha BCD}\, O_{E'E} \\ \times \Big\{ \left[\bar{u}_{B'}(x')u_E(x)\right]_U \left[\bar{u}_{E'}(y)u_B(x)\right]_U \left[\bar{d}_{C'}(x')d_C(y)\right]_U \left[\bar{u}_{D'}(x')u_D(x)\right]_U \\ - \left[\bar{u}_{B'}(x')u_E(x)\right]_U \left[\bar{u}_{E'}(y)u_D(x)\right]_U \left[\bar{d}_{C'}(x')d_C(y)\right]_U \left[\bar{u}_{D'}(x')u_B(x)\right]_U \\ + \left[\bar{u}_{B'}(x')u_B(x)\right]_U \left[\bar{d}_{C'}(x')d_C(y)\right]_U \left[\bar{u}_{D'}(x')u_E(x)\right]_U \left[\bar{u}_{E'}(y)u_D(x)\right]_U \\ - \left[\bar{u}_{B'}(x')u_D(x)\right]_U \left[\bar{d}_{C'}(x')d_C(y)\right]_U \left[\bar{u}_{D'}(x')u_E(x)\right]_U \left[\bar{u}_{E'}(y)u_B(x)\right]_U \Big\} \end{aligned} \tag{3.35}$$

The contractions of Eq. (3.35) are graphically illustrated in Fig. 3.4.

At this point we have reduced calculating correlation functions of the nucleon to the computation and contraction of quark propagators. All we are left with is a tool to calculate the quark propagator, however in a non-perturbative way. A natural and straightforward way to do so is given by lattice QCD, on which we concentrate in the next chapter.

3.6 Renormalization

In the discussion of correlation functions and matrix elements of the nucleon we have thus far ignored an important fact. The ratios in the equations (3.16) and (3.17) only give bare matrix elements that need to be renormalized.

For comprehension we start with a discussion in the framework of perturbation theory. The

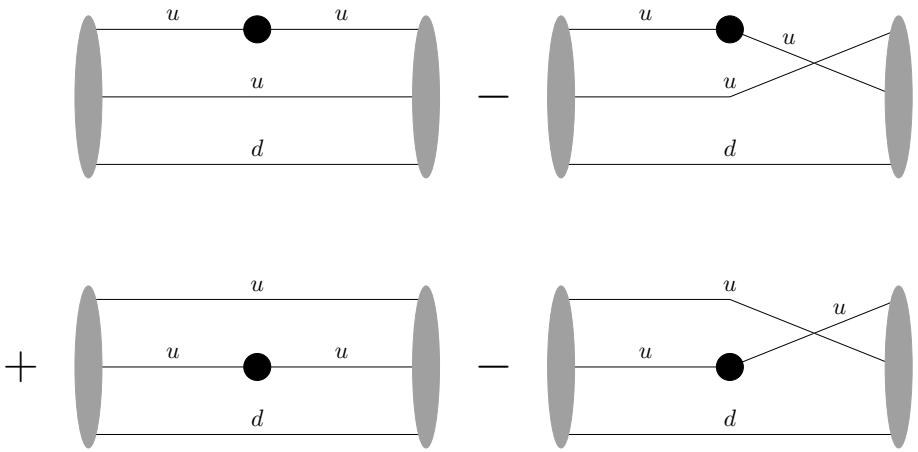

Figure 3.4: Contraction pattern of the connected piece of the proton 3-point function involving a local operator of type $\bar{u}Xu$. The operator insertion is represented by a filled black circle.

essential concepts, regularization and the imposition of renormalization conditions can as well be used in a non-perturbative way, such as in lattice QCD. We discuss the non-perturbative renormalization later, in Sec. 4.2.

To begin with, let us first consider the perturbative expansion (in powers of the bare coupling g around the free theory) of Green functions like the correlation functions defined in the previous sections. The terms of the expansion are typically represented as Feynman diagrams. While tree diagrams, like the one in the left panel of Fig. 3.5, represent well-defined amplitudes, for loop diagrams, see Fig. 3.5 (right), we have to integrate over the internal momenta which typically results in divergent expressions. Therefore one has to introduce an ultra-violet momentum cut-off Λ rendering all loop integrals finite[2]. This process is known as regularization. Renormalization is a well-defined formalism to associate regularized expressions to amplitudes that remain finite when the cut-off is removed, *i.e.* $\Lambda \to \infty$ order by order in perturbation theory. The theory is (perturbatively) renormalizable if *a finite* set of renormalization conditions renders the amplitudes finite at all orders of perturbation theory.

In QCD, renormalization amounts to computing multiplicative renormalization constants (often called Z-factors) for the elementary quark fields, Z_q, such that

$$q^R = Z_q^{\frac{1}{2}} q, \quad \bar{q}^R = Z_q^{\frac{1}{2}} \bar{q}. \tag{3.36}$$

Moreover, Z-factors for the bare quark mass and the bare coupling have to be computed.

$$m_q^R = Z_{m_q} m_q, \quad g^R = Z_g g \tag{3.37}$$

Those Z-factors are obtained by imposing a set of renormalization conditions. For our pur-

[2] In principle there can also be infrared divergences, which however do not appear in the observables considered here and are therefore ignored.

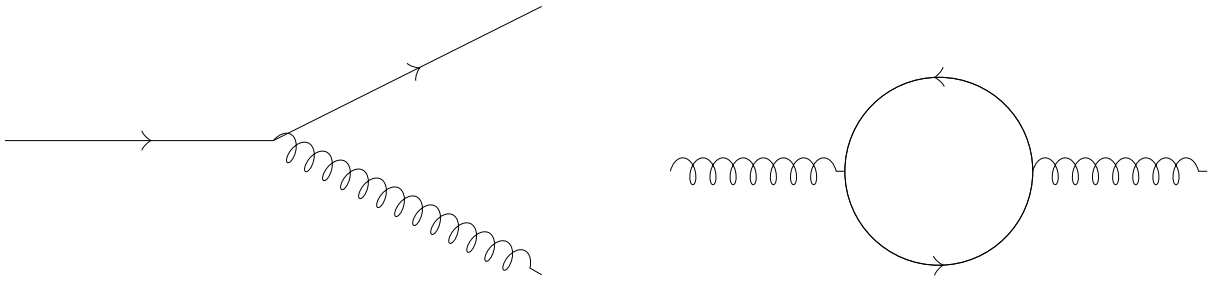

Figure 3.5: left: Example of a tree diagram in QCD. **right:** Example of a QCD loop diagram. A solid line corresponds to a quark propagator in the free theory and the helical line depicts a free gluon propagator.

pose it is most convenient to use the so-called RI′MOM scheme [22], where *e.g.* for two-quark operators like the ones used in this thesis work we impose the renormalization condition

$$Z_{\mathcal{O}} \langle p| \mathcal{O} |p\rangle \Big|_{p^2=\mu^2} = \langle p| \mathcal{O} |p\rangle_{\text{tree}}, \tag{3.38}$$

where on the left hand side we have the full operator matrix element of interest in some fixed gauge, here the Landau gauge, evaluated at a renormalization scale μ^2. It can be evaluated non-perturbatively using lattice QCD methods. The renormalization condition is then that the so computed matrix element at the scale $p^2 = \mu^2$ equals its tree-level value. In order to make contact the most commonly used $\overline{\text{MS}}$ scheme, which is essentially a subtraction of the most divergent pole emerging from a dimensional regularization, we need a conversion prescription between the two schemes. A set of conversion factors $C_{\mathcal{O}}$ can be calculated perturbatively [23], such that

$$Z_{\mathcal{O}}^{\overline{\text{MS}}} = C_{\mathcal{O}} Z_{\mathcal{O}}^{\text{RI′MOM}}. \tag{3.39}$$

The scale is typically $\mu^2 = (2\text{ GeV})^2$. The conversion factors are functions of the coupling in the RI′MOM scheme and the gauge fixing parameter λ and are typically known to three-loop order [24].

Note that for some matrix elements Ward identities (the quantum analogue of the Noether theorem) hold, as a consequence of symmetries. In this case – since the Ward identity remains unaffected by renormalization, the Z-factor for the corresponding matrix element is trivial.

In general the renormalization procedure mixes operators possessing the same quantum numbers and of the same or less dimension.

$$\mathcal{O}_i^R = \sum_j Z_{ij} \mathcal{O}_j^{(\text{bare})} \tag{3.40}$$

For example, in order to renormalize a twist-two operator $\mathcal{O}^{\mu_1 \cdots \mu_n}$ [see Eq. (2.25)] involving two

quark fields, one has to compute the diagrams shown in Fig. 3.6. However, for even n there

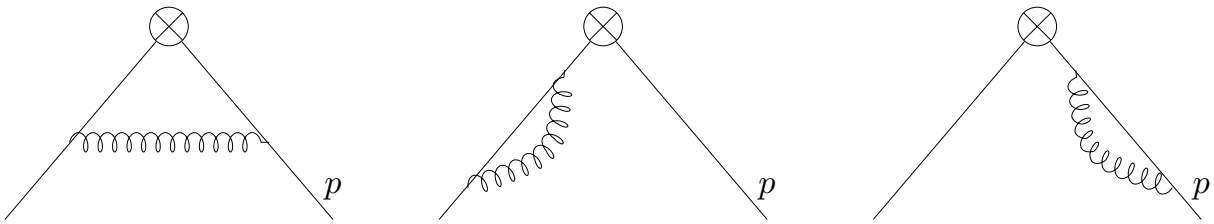

Figure 3.6: Diagrams contributing to the Z-factor for a local twist-two operator.

exist also twist-two operators involving the gluon field,

$$O_g^{\mu_1\cdots\mu_n} = F^{\{\mu_1\nu}D^{\mu_2}\cdots D^{\mu_{n-1}}F^{\mu_n\}\nu}. \tag{3.41}$$

The braces indicate symmetrization in the μ indices and subtraction of the trace. In Fig. 3.7 we show the diagrams that give rise to mixing with this operator. When mixing occurs, we have a renormalization pattern which is more complicated than the multiplicative renormalization. In particular, here one would have to compute matrix element of $O_g^{\mu_1\cdots\mu_n}$ which is way more demanding than for the twist-two operator involving two quark fields, $O^{\mu_1\cdots\mu_n}$.

We would like to conclude this section by emphasizing that imposing the renormalization condition Eq. (3.38) involves computing correlation functions in Landau gauge, and that this computation can be carried out in lattice QCD.

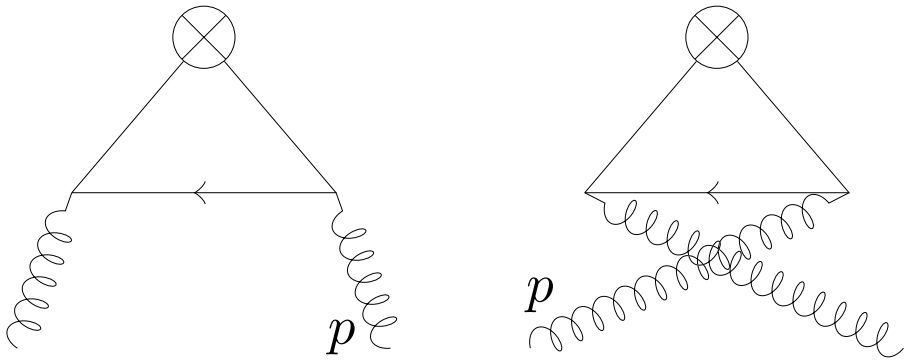

Figure 3.7: Diagrams that induce mixing between a local twist-two operator $O^{\mu_1\cdots\mu_n}$ (n even) with two fermion fields and a gluonic twist-two operator $O_g^{\mu_1\cdots\mu_n}$ under renormalization.

4 Introduction to Lattice QCD

In the previous chapter we discuss how to calculate matrix elements of local operators in (Euclidean) quantum field theory using suitable ratios of 3-point and 2-point correlation functions of the nucleon. We also describe how to express the correlation functions in terms of Wick contractions of the quark fields, which amounts to calculating quark propagators as fundamental building blocks of the correlation functions. We are left with the demand for a non-perturbative method to compute those quark propagators. Lattice QCD (LQCD) provides a tool for a calculation "from first principles", which means a direct numerical calculation in discrete euclidean space-time. We learn how this is possible in the course of this chapter. It shall serve as an introduction of some aspects of LQCD. Since the main focus of this thesis is on hadron structure, we keep the discussion of the basic elements brief and refer to LQCD books (*e.g.* [25], [26] or [27])for more details. More advanced and technical issues are discussed in the proximate chapter.

4.1 Numerical Treatment of the Path Integral

The form of the path integral in Euclidean QFT with a weight e^{-S}, which resembles the partition function in statistical physics, suggests a treatment by means of statistical methods, if one is interested in a numerical evaluation of the path integral. In fact, Monte-Carlo integration, employing importance sampling, is used to perform the integration.

Before we introduce the lattice formulation of QCD let us briefly review a few basic ingredients in the continuum theory. For simplicity we restrict to a single quark flavor, however the generalization is straightforward for more than one quark flavors. We start with the QCD action S_{QCD} that can be divided into a gauge action S_g and a fermionic action S_f.

$$S_{\mathrm{QCD}} = S_g + S_f \tag{4.1}$$

$$S_g = \int d^4x \, \frac{1}{4} \,\mathrm{Tr}\, F^{\mu\nu}(x) F_{\mu\nu}(x), \tag{4.2}$$

$$S_f = \int d^4x \; \bar{\psi}(x) \left[\gamma^\mu D_\mu + m_0\right] \psi(x). \tag{4.3}$$

Here, $F^a_{\mu\nu} = \partial_\mu A^a_\nu - \partial_\nu A^a_\mu + g f^{abc} A^b_\mu A^c_\nu$ is the field strength tensor, A^a_μ is the $SU(3)$ gauge field, f^{abc} are the so-called structure constants of the $SU(3)$ group and the trace is in color space. $D_\mu = \partial_\mu + igA_\mu$ is the covariant derivative, which couples the gauge fields to the quark fields with the coupling strength g. ψ denotes the quark field, which is a spinor field with 12 (3 color

times 4 Dirac) components. Most notably, the action is invariant under local gauge transformations

$$\psi(x) \to G(x)\psi(x), \quad \bar{\psi}(x) \to \bar{\psi}(x)G^\dagger(x), \tag{4.4}$$

$$A_\mu(x) \to G(x)A_\mu(x)G^\dagger(x) - \frac{i}{g}G(x)\partial_\mu G^\dagger(x), \tag{4.5}$$

where $G(x) = e^{i\lambda_a(x)\tau_a}$ is an element of the non-abelian gauge group $SU(3)$.

Let us now introduce a discretized space-time on a hypercubic grid, the *lattice*, with a spacing a, the *lattice spacing*, between nearest neighbors in each direction. To this end it is convenient to replace all dimensionful variables with dimensionless lattice variables by scaling them with a power of a according to their dimension, *e.g.* $\psi(x) \to a^{-3/2}\psi(x)$, $m_0 \to a^{-1}m_0$. Since in practice it very simple to restore the dimension and to discriminate between dimensionful and dimensionless quantities, we do not see the need of introducing new symbols for the dimensionless lattice variables.
Note that eventually the cut-off $\Lambda = 1/a$ has to be removed by sending the lattice spacing to zero. The limit $a \to 0$ is called continuum limit. In order to have a physical result – recall the discussion about renormalization in Sec. 3.6 – we need to do this in a particular way in order to keep the physics the same when sending a to zero. This is detailed in Sec. 4.2. Furthermore, in order to perform the numerical calculation we also have to restrict to a finite volume, which serves as an infrared cut-off. The consequences this has on the results are discussed later, in Sec. 4.5.
In the discretized theory, the quark field is defined on the lattice sites (the discrete grid points) and the gauge fields are represented by the so-called gauge links $U_\mu(x)$, which connect two lattice sites in one direction,

$$U_\mu(x) = e^{igaA_\mu(x)} \tag{4.6}$$

Let us now discuss the simplest way of defining a lattice QCD action. The properties of such a discretized action are discussed later.
One way to define a discretized version of the gauge action, Eq. (4.2), is via plaquettes, quadratic planar Wilson loops, path-ordered products of gauge links, with an extent of a single lattice spacing in each direction,

$$U_{P\,\mu\nu}(x) = U_\nu^\dagger(x)\, U_\mu^\dagger(x+\hat{\nu})\, U_\nu(x+\hat{\mu})\, U_\mu(x). \tag{4.7}$$

The action arising from Eq. (4.7) is,

$$S_g^{\text{plaq}} = \frac{6}{g^2} \sum_x \sum_{\mu<\nu} \left(1 - \frac{1}{3}\ \text{Re Tr}\ \left[U_{P\,\mu\nu}(x)\right]\right), \tag{4.8}$$

where the first sum is over all lattice sites and the second sum is over all μ-ν planes without double counting. The factor $\frac{6}{g^2}$ is usually called β, in fact β is also conventionally called coupling.

The fermionic lattice action as proposed in 1975 by Wilson [28], who also suggested the plaquette gauge action [29], reads

$$S_f^{\mathrm{W}}[\bar{\psi},\psi,U] = (m_0+4r)\sum_x \bar{\psi}(x)\psi(x) \\ -\frac{1}{2}\sum_{x,\mu}\left[\bar{\psi}(x)(r-\gamma_\mu)U_\mu(x)\psi(x+\hat{\mu}) + \bar{\psi}(x+\hat{\mu})(r+\gamma_\mu)U_\mu^\dagger(x)\psi(x)\right], \quad (4.9)$$

where r is the so-called Wilson parameter that is conventionally chosen to be 1 in most applications. $\hat{\mu}$ is a vector in μ-direction with a length of one lattice spacing. It can be shown that this action reproduces in fact the continuum action, Eq. (4.3), when the lattice spacing is sent to zero.

For the evaluation of correlation functions it is beneficial to consider the so called Hopping Parameter Expansion. We can rewrite the Wilson action S_f^{W} in the following form.

$$S_f^{\mathrm{W}} = \frac{1}{2\kappa}\sum_{x,y}\bar{\psi}_x M_{xy}[U]\,\bar{\psi}_y \quad (4.10)$$

$$\kappa = \frac{1}{8r+2m_0} \quad (4.11)$$

κ is called hopping parameter. The matrix $M_{xy}[U]$ is a matrix in Dirac and color space as well as discrete position space, since x and y assume only discrete values. This matrix has the form

$$M_{xy}[U] = \delta_{xy}\mathbb{1} - \kappa\tilde{M}_{xy}[U], \quad (4.12)$$

where the only non-vanishing terms in $\tilde{M}_{xy}$ are those connecting neighboring lattice sites, hence the name hopping parameter for κ. The overall factor $1/2\kappa$ in Eq. (4.10) can be absorbed by a field redefinition

$$\bar{\psi}(x) \to \frac{1}{\sqrt{2\kappa}}\bar{\psi}(x), \quad \psi(x) \to \frac{1}{\sqrt{2\kappa}}\psi(x), \quad (4.13)$$

after which the action reads

$$S_f^{\mathrm{W}} = \sum_{x,y,\alpha,\beta,a,b}\bar{\psi}_{x\alpha a}\left(M_{xy}[U]\right)_{(\alpha a)(\beta b)}\bar{\psi}_{y\beta b} \quad (4.14)$$

where we retain the Dirac α,β and color indices a,b in order to make the reader aware of the full Dirac and color structure. M is frequently referred to as Dirac matrix.

Concerning the evaluation of correlation functions we need to consider the path integral formalism. The path integral, defined purely formally in the continuum can now be given a con-

crete definition on the lattice,

$$\int \mathcal{D}U \;= \prod_{x,\mu} \int dU_{x,\mu} \;, \quad \int \mathcal{D}(\bar{\psi}\psi) \;= \prod_{x,A} \int d\bar{\psi}_{x,A}\, d\bar{\psi}_{x,A} \;. \tag{4.15}$$

We have summarized the Dirac and color degrees of freedom in the capital Roman letters for simplicity in the above equations. The integration variables $\bar{\psi}$ and ψ are anti-commuting Grassmann numbers, which by their integration rules satisfy

$$\int \mathcal{D}(\bar{\psi}\psi)\; e^{-S_f^{\mathrm{W}}[U,\bar{\psi},\psi]} = \det M[U]. \tag{4.16}$$

Therefore, the path integral simplifies to

$$\int \mathcal{D}U\; \mathcal{D}(\bar{\psi}\psi)\;\; e^{-S_{\mathrm{QCD}}} = \int \mathcal{D}U\; e^{-S_g[U]} \det M[U]. \tag{4.17}$$

The determinant $\det M[U]$ can be interpreted as a measure encoding the influence of (disconnected) quark loops as vacuum fluctuations. For this interpretation however, we need to ensure we have a real and positive integration measure. Fortunately, M, although being non-hermitian, satisfies a γ_5-hermiticity

$$M^\dagger = \gamma_5 M \gamma_5, \tag{4.18}$$

from which immediately follows that $\det M$ is real. Moreover, for $\kappa < 1/8$, which is the case for the usual choices $r = 1$ and $m_0 > 0$, it was shown that $0 < \det M < 1$ [30]. This allows an interpretation of the path integral measure $e^{-S_g[U]} \det M[U]$ as a real probability density which hence renders a treatment by statistical means possible.
With this in mind, we can consider a generic correlation function, involving the fields ψ, $\bar{\psi}$ and U,

$$\begin{aligned}
&\Big\langle \psi_{x_1,A_1} \cdots \psi_{x_N,A_N} \bar{\psi}_{y_1,B_1} \cdots \bar{\psi}_{y_N,B_N} U^{c_1 d_1}_{z_1,\mu_1} \cdots U^{c_M d_M}_{z_M,\mu_M} \Big\rangle \\
&\quad = \frac{\int \mathcal{D}U\; \mathcal{D}(\bar{\psi}\psi)\;\; \psi_{x_1,A_1} \cdots \psi_{x_N,A_N} \bar{\psi}_{y_1,B_1} \cdots \bar{\psi}_{y_N,B_N} U^{c_1 d_1}_{z_1,\mu_1} \cdots U^{c_M d_M}_{z_M,\mu_M}\, e^{-S^{\mathrm{lattice}}_{\mathrm{QCD}}[U,\bar{\psi},\psi]}}{\int \mathcal{D}U\; \mathcal{D}(\bar{\psi}\psi)\;\; e^{-S^{\mathrm{lattice}}_{\mathrm{QCD}}[U,\bar{\psi},\psi]}}, \\
&\quad = \frac{\int \mathcal{D}U\; \left\langle \psi_{x_1,A_1} \cdots \psi_{x_N,A_N} \bar{\psi}_{y_1,B_1} \cdots \bar{\psi}_{y_N,B_N} \right\rangle_{S_f} U^{c_1 d_1}_{z_1,\mu_1} \cdots U^{c_M d_M}_{z_M,\mu_M}\, e^{-S_g[U]} \det M[U]}{\int \mathcal{D}U\;\; e^{-S_g[U]} \det M[U]}
\end{aligned} \tag{4.19}$$

where $x_i, y_i \quad i = 1, \ldots, N$ and $Z_i, \quad i = 1, \ldots, M$ label lattice sites and A_i, B_i, label color and Dirac index and c_i, d_i are color indices indicating the element of the color matrix U_{z_i,μ_i}.

For every gauge field configuration[1] $\{U\}$, Wick's theorem applies, *i.e.*

$$\left\langle \psi_{x_1,A_1} \cdots \psi_{x_N,A_N} \bar{\psi}_{y_1,B_1} \cdots \bar{\psi}_{y_N,B_N} \right\rangle_{S_f} = \sum_{\text{contractions}} \psi_{x_1,A_1} \cdots \psi_{x_N,A_N} \bar{\psi}_{y_1,B_1} \cdots \bar{\psi}_{y_N,B_N} \tag{4.20}$$

A contraction is here used in the sense of a 2-point function on a fixed configuration of gauge links $\{U\}$

$$\left\langle \psi_{x,A} \bar{\psi}_{y,B} \right\rangle_{S_f} = \frac{1}{\det M[U]} \int \mathcal{D}(\bar{\psi}\psi)\, e^{-S_f^W[\{U\},\bar{\psi},\psi]} \psi_{x,A} \bar{\psi}_{y,B}, \tag{4.21}$$

$$= (M^{-1})_{xA\,yB}[U]. \tag{4.22}$$

In the last line we have again used integration rules for Grassmann variables. Thus on a fixed gauge field background the 2-point function of the quark fields – the quark propagator – is just the inverse of the Dirac matrix M, on a given gauge field background. We discuss the calculation of quark propagators in Sec. 4.3. It is the building block of all hadronic correlation functions such as the nucleon correlation functions we need to compute in order to obtain nucleon matrix elements.

Having learned how the path integral formalism can be rigorously applied in the framework of lattice QCD, we would like to discuss now how this is done in practice. The path integration over the configuration space, as it appears on the right hand side of Eq. (4.17), is numerically performed by creating an ensemble of gauge link configurations $\{U\}$, obeying the probability distribution

$$\mathbb{P}\left(\{U\}\right) \propto e^{-S_g[U]} \det M[U]. \tag{4.23}$$

To achieve such a distribution one can make use of a simulation algorithm. When we speak about simulations, we always mean generating ensembles of gauge field configurations that are distributed according to the probability density Eq. (4.23). The algorithm typically employed nowadays is Hybrid Monte Carlo (see *e.g.* Refs. [31, 32] for a review). Once a number N_{g} of gauge field configurations has been generated, the integration can be properly approximated by the mean over the gauge field configurations, provided statistical independence of the configurations holds. That is,

$$\langle O \rangle = \frac{\int \mathcal{D}U\, \mathbb{P}\left(\{U\}\right) O[U]}{\int \mathcal{D}U\, \mathbb{P}\left(\{U\}\right)}$$

$$\approx \frac{1}{N_{\mathrm{g}}} \sum_{\{U_\mu\}} O_{\{U\}}. \tag{4.24}$$

The observable O can be thought of as a generic correlation function as described above. The error introduced by summing over a finite number of gauge field configurations is referred to

[1] We use the common term gauge field configuration for a configuration of gauge link variables, which is formally wrong but generally accepted. In the context of lattice gauge theory it should be clear that the gauge fields cannot be treated directly, but always in terms of link variables.

as gauge noise. Its magnitude depends on the observable, but for sufficiently large N_{gauge} we know it scales like $1/\sqrt{N_{gauge}}$. Moreover, in the limit $N_{\text{gauge}} \to \infty$ equality holds in Eq. (4.24). Of course there is a number of technical subtleties that have not been mentioned. Those are addressed in the following sections.

4.2 Continuum limit and Non-perturbative Renormalization

Lattice QCD calculations are carried out in discrete euclidean space-time with a non-zero lattice spacing a. This provides a natural regularization since the (inverse) lattice spacing serves as a momentum cut-off. The reason is that all functions on the lattice are periodic in momentum space with a periodicity of $2\pi/a$, such that we can restrict all momenta to the interval $]-\pi/a, \pi/a]$, the first Brillouin zone. Accordingly we have a momentum cut-off π/a.
In order to obtain QCD results in the continuum, the lattice spacing a has to be sent to zero, thus removing the cut-off, which in turn would render loop integrals divergent (*cf.* discussion in Sec. 3.6). However, we have to assure that when decreasing a we move along a line of constant physics, otherwise the continuum limit does not make sense. This can be achieved by choosing the bare mass m_0 and the coupling g as functions of a such that the physics is unaltered as we approach the continuum limit. To state this more precisely, once we have chosen starting values for m_0, g and a and we obtain a certain value for a physical – here hadronic – quantity (*e.g.* the pion mass m_π), we have to guarantee that m_π has the same value when decreasing a, which can be done by choosing the coupling and the bare quark mass appropriately.

Apart from this, renormalization is necessary to obtain finite results. In general the renormalization prescription, analogously to Eq. (3.38) in Sec. 3.6, reads

$$\mathcal{O}^R(\mu, a) = Z_{\mathcal{O}}\left(a\mu, g(a)\right)\mathcal{O}(a), \tag{4.25}$$

where $\mathcal{O}(a)$ is the bare lattice operator at a lattice spacing a, and $\mathcal{O}^R(\mu, a)$ is the renormalized operator obtained at a renormalization scale μ. The Z factors are found by imposing appropriate renormalization conditions for each value of a, like in Sec. 3.6. Thus we obtain Z-factors for every value of a, or equivalently $\beta = 6/g^2$. Note that in the continuum limit $\mathcal{O}^R(\mu, a)$ will eventually become independent of a. We would like to stress that this procedure is our choice in this thesis work and that there are other renormalization prescriptions available, such as the Schrödinger Functional scheme (see Ref. [33]) or x-space renormalization [34].

Thus, the non-perturbative renormalization of operators works essentially like in the continuum, apart from the fact that the required Green's functions are computed non-perturbatively using lattice QCD methods. We use the RI′MOM scheme (see Sec. 3.6), where we compute the Z-factors in the limit of zero quark mass, see Ref. [35] for a review. Since we need the Green functions in momentum space, the computation can either be done directly in momentum space or through a Fourier transform of position-space Green's functions.
Four our case of twisted mass fermions, perturbative as well as non-perturbative renormalization constants for the quantities discussed in this thesis are available [36, 37, 38, 39, 40].

Note that, as already explained in Sec. 3.6, we would like to match the renormalization factors obtained in the renormalization scheme of our choice, here RI′MOM [22], to the $\overline{\text{MS}}$ scheme at a typical scale $\mu = 2$ GeV, which requires to make contact to perturbative QCD at some order.

4.3 Quark Propagator, Quark Mass and the Chiral Limit

As mentioned in the last chapter the basis of most lattice calculations involving correlation functions of hadrons – once the gauge field ensembles have been generated – is the quark propagator. We describe in Sec. 4.1 that the quark propagator, on a fixed gauge field configuration, is the inverse of the Dirac matrix M (see Eq. (4.14)),

$$\left[\psi_{x\alpha a}\bar{\psi}_{y\beta b}\right]_U = (M^{-1})_{x\alpha a\, y\beta b}[U]. \tag{4.26}$$

where the Greek indices refer to the Dirac space and a, b are color indices. The lattice sites are labeled by x and y. We often rearrange the indices for better readability and introduce the symbol S for the inverse of M,

$$\left(M^{-1}\right)^{\alpha\beta}_{ab}(x,y) \equiv S^{\alpha\beta}_{ab}(x,y). \tag{4.27}$$

Note that although being strictly correct only in the ensemble average, where the quark propagator vanishes due to the fact that it is a gauge variant quantity, we use the term quark propagator for the inverse of the Dirac matrix M on a single gauge field configuration here. We will also apply this convention to other correlation functions. It becomes clear in the context what is meant.

Having demonstrated that the calculation of a quark propagator amounts to the inversion of a matrix, we have to admit that in practice this is not an easy task. The reason is that the Dirac matrix is huge, possessing 4 (spin) times 3 (color) times the number of lattice sites rows and columns. With a typical lattice size of $32^3 \times 64$ which tends to be a small lattice compared to state-of-the-art calculations, this is already more than 25 millions. In practice, owed to translational invariance, one only needs the solution for a fixed point y. That is, we do not actually calculate the inverse of this matrix, but just solve a set of linear equations, $M(x,y)\phi(x) = \eta(y)$. This process is usually called "inversion", a term we will – by abuse of language – use frequently below, although this is wrong in a strict mathematical sense. The solution of the system of linear equations can be obtained using iterative methods among which are Krylov space solvers like the conjugate gradient algorithm. Preconditioning is most commonly used in order to speed up the calculation. Let us remark that for matrices as big as the Dirac matrix discussed here iterative solvers are faster than and therefore more suitable than exact algorithms.

Clearly, the computational effort it takes to calculate a quark propagator depends on the parameters. As a matter of fact the size of the lattice in units of the lattice spacing has an influence since it determines the size of the matrix M. Also, the lattice spacing affects the inversion time. Most importantly, however, is the influence of the quark mass, which is in principle a

free parameter in lattice QCD and needs to be tuned to achieve a constant physical situation as discussed in the previous section. Generally spoken, the heavier the quark mass the cheaper is the inversion. Typically for the sake of a more feasible calculation observables are computed at heavier quark masses than the physical one and an extrapolation to the latter is performed a posteriori. A prescription for a possible extrapolation is given by chiral perturbation theory (χPT), which is – loosely spoken – an expansion of the QCD Lagrangian around zero pion mass. See Ref. [41] for a review. The extrapolation from pion masses higher than the physical one (by a factor 2 to 4 in most of the reported calculations today) to the physical one is called chiral extrapolation, even though the physical pion mass we extrapolate towards is finite, *i.e.* $m_\pi = 139.57$ MeV [11]. The important point is that χPT yields relations between quark masses and hadronic quantities. For example, the square of the pion mass m_π^2 is proportional to the quark mass to leading order. Therefore we mean the same when we talk about extrapolation to physical quark or physical pion mass. Note, however, that the pion mass is conceptually much cleaner since it can be measured directly in experiment, while the quark mass can only be determined indirectly. While the application of χPT yields reliable extrapolation formulas for light mesons that describe the data well, see *e.g.* [42] for the case of twisted mass fermions, it is unclear whether χPT can be used for a chiral extrapolation of baryonic quantities. We will discuss this at a later point.

Note that a chiral extrapolation is becoming increasingly redundant since several calculations at the physical pion mass are in preparation or already completed [43]. However, in the scope of this thesis, the available pion masses are 225 MeV $\lessapprox m_\pi \lessapprox$ 480 MeV, hence we still need an extrapolation to the physical point.

4.4 Scale Setting

In the preceding sections of this chapter we ignore one important fact. Lattice QCD is performed numerically and thus all numbers we obtain are naturally dimensionless. The correct dimension can be retained by multiplying with appropriate powers of the lattice spacing a. However, choosing some value of the bare parameters β and m_0, the physical size of this unit, say in fm is a priori unknown. In order to determine it – a procedure called scale setting – one needs to compute a (hadronic) quantity in units of the lattice spacing and compare to its experimentally measured value. This of course requires a calculation at the physical quark mass(es) or – more usually – a chiral extrapolation thereto. Since one would like to have a precise determination of the lattice spacing, it is necessary to use a quantity with a small experimental error to set the scale. In addition, the chiral extrapolation of the lattice calculations should have a small uncertainty relative to other hadronic quantities, at a given computational effort. It is therefore advantageous to use a hadronic observable without strong dependence on the quark mass, because in the case of a strong dependence the uncertainty of the chiral extrapolation will be large compared to a quantity possessing a very mild quark mass dependence.

Among the quantities used is the Sommer scale r_0, which is defined via the static quark-antiquark force, the nucleon mass m_N and more recently also the omega baryon mass m_Ω [44].

For the gauge field ensembles relevant for this work the pion decay constant f_π has been used to set the scale, see *e.g.* [42, 45, 46].

4.5 Finite Size Effects

In every numerical calculation involving a discretization one has to restrict to a finite volume, which is a systematic effect, since in a finite volume translational invariance does not hold. One would expect a different behavior of correlation functions involving lattice sites close to the boundary compared to those in the bulk, *i.e.* there is a surface effect, that is expected to vanish when the surface becomes negligible compared to the volume. Using periodic boundary conditions is a good way to reduce such an effect, for one can show that asymptotically (*i.e.* if the lattice is sufficiently big) these finite size effects (FSE) are exponentially suppressed like $\sim \exp(-m_\pi L)$, where L is the physical extent[2]. See *e.g.* Refs. [47, 48] for a numerical study and detailed discussion. Therefore, in order to suppress finite size effects, we need $m_\pi L \gg 1$, *i.e.* we want $m_\pi L$ to be sufficiently large such that finite size effects are suppressed. Note that if the lattice spacing is small the lattice extent in units of the lattice spacing L/a has to be a large number which is strongly limited by memory size and computational power. For example, when we have a lattice extent of say $L = 3$ fm and a lattice spacing of $a = 0.05$ fm, this means we have a lattice size $L/a = 60$, which is rather large but still feasible. In this case, with the physical pion mass, $m_\pi L = 2.1$. Consequently, we cannot realize $m_\pi L \gg 1$ in practice. Note however that in the case where the pion mass is heavier than the physical one, it is easier to realize.
It is a fortune that in lattice QCD, FSE are typically small if $m_\pi L \gtrapprox 4$. This is an empiric rule of thumb, but it has to be taken with care. FSE can be quite different for different quantities and should therefore always be studied carefully.
In the scope of this thesis we use periodic boundary conditions for all fields in spatial directions. Regarding the euclidean time we also employ periodic boundary conditions for (gluonic) gauge fields whereas for quark fields anti-periodic boundary conditions are implemented.
For all quantities computed in this thesis we have several volumes available, which allows us to test for possible finite size effects.

4.6 Lattice Discretization Effects

In this section we would like to complete the discussion of basic aspects of lattice QCD by presenting some general properties of the lattice discretization, before we get to know a particular example thereof in the subsequent chapter.

Like every Quantum Field theory, QCD can be defined via the action, or the Lagrangian, respectively. In lattice QCD, however, we have a large freedom to define the lattice action without

[2]Strictly speaking this statement only holds in cases where m_π is the smallest mass scale.

violating some fundamental properties of field theories such as locality, causality, renormalizability, and the required symmetries in the continuum limit. There is a variety of gauge and fermion actions that have various advantages and disadvantages, see Ref. [25].

They all have some properties in common, on which we concentrate in this paragraph. First of all, there is an exact lattice gauge symmetry. Secondly, any lattice action needs a mechanism to overcome fermion doubling, the emergence of unphysical poles in the lattice fermion propagator in momentum space due to the finite lattice spacing. For Wilson-type fermions the unphysical poles are removed by adding a term that breaks chiral symmetry explicitly, which however is restored in the continuum limit. Finally, there are lattice artifacts as a consequence of the discretization. In approaching the continuum limit, corrections to observables naturally scale as powers of a, the power depending on the action used. In practice one has a leading correction $\mathcal{O}(a)$ or $\mathcal{O}(a^2)$. A systematic description of lattice artifacts that works quite well in practice is given by the Symanzik effective continuum theory [49]. This allows in particular construction of lattice actions that scale with $\mathcal{O}(a^2)$ towards the continuum limit.

For completeness let us now focus on the gauge action. As in the case of the fermionic action the only requirement is to reproduce the continuum QCD action, Eq. (4.2), as $a \to 0$. The simplest way of defining an action satisfying this condition is the plaquette action, Eq. (4.8). In fact, as we approach the continuum limit,

$$S_g^{\text{plaquette}} \to S_g^{\text{cont.}} + \mathcal{O}(a^2). \tag{4.28}$$

It is straightforward to construct actions without $\mathcal{O}(a^2)$ lattice artifacts, using combinations of Wilson loops of different shapes. Conceptually, though, we still build the action from closed and path-ordered loops (products) of gauge links. That is why we can keep the discussion short here and just refer to the standard literature (*e.g.* [25, 26]) and for our particular case to Ref. [50] for further reading.

Concerning the work done in the scope of this thesis the gauge action will never appear directly in the calculations since the gauge field ensembles are provided by our collaboration, the European Twisted Mass Collaboration (ETMC). Apart from the implicit weight of the individual configurations [see Eq. (4.23)], the gauge action does not play a role in the correlation functions we compute.

4.7 Conclusion

In this chapter we have discussed how QCD correlation functions in euclidean space-time can be evaluated numerically by means of lattice QCD. We have learned that observables are estimated by averaging over an ensemble of gauge field configurations.
We have also pointed out several systematic uncertainties arising in lattice calculations, such as finite size effects, finite quark mass and lattice discretization. We emphasize that the gauge field ensembles used in this work are obtained at several values of the lattice spacing, the lattice volume and pion mass. Thus, those systematic effects can be studied and quantified.

5 Technical Aspects of Lattice QCD and Wilson Twisted Mass Discretization

After the preparations made in the previous chapter we are now equipped with all ingredients necessary to obtain the physical observables of interest in this thesis. The general procedure is the following: Firstly, we compute quark propagators on an ensemble of gauge field configurations distributed according to the appropriate path integral weight, Eq. (4.23). Secondly, we build (contract) the nucleon correlation functions of interest from those propagators.
In this chapter we are going through some specifications and methods that are important in connection with the thesis work presented in the following chapters. More precisely, we describe the Wilson Twisted Mass lattice discretization and demonstrate some lattice techniques that we make use of to remove unwanted effects or to have more accurate results at a given computational effort compared to standard methods.

5.1 Wilson Twisted Mass Lattice Discretization

In this work we use Wilson twisted mass fermions (see Ref. [51] for a review). They are defined via the action

$$S_l^{TM} = a^4 \sum_x \bar{\chi}_l(x) \left[D_W + m_0 + i\gamma_5 \tau_3 \mu_l \right] \chi_l(x), \tag{5.1}$$

$$D_W = \frac{1}{2} \left[\gamma_\mu \left(\nabla_\mu + \nabla_\mu^* \right) - ar \nabla_\mu^* \nabla_\mu \right], \tag{5.2}$$

where m_0 is the bare quark mass and μ_l is the twisted mass. Quarks are combined in flavor doublets χ. The l is for light, indicating that Eq. (5.1) is the action for the light doublet (u, d). D_W is the Wilson operator, *cf.* Eq. (4.9). The lattice forward and backward derivatives ∇ and ∇^*, respectively, are defined

$$\nabla_\mu \chi(x) = \frac{1}{a} \left[U_\mu(x) \chi(x + a\hat{\mu}) - \chi(x) \right], \tag{5.3}$$

$$\nabla_\mu^* \chi(x) = \frac{1}{a} \left[\chi(x) - U_\mu^\dagger(x - a\hat{\mu}) \chi(x - a\hat{\mu}) \right], \tag{5.4}$$

$$\bar{\chi}(x) \overleftarrow{\nabla}_\mu = \frac{1}{a} \left[\bar{\chi}(x + a\hat{\mu}) U_\mu^\dagger(x) - \bar{\chi}(x) \right], \tag{5.5}$$

$$\bar{\chi}(x) \overleftarrow{\nabla}_\mu^* = \frac{1}{a} \left[\bar{\chi}(x) - \bar{\chi}(x - a\hat{\mu}) U_\mu(x - a\hat{\mu}) \right]. \tag{5.6}$$

The so-called Wilson parameter r is conventionally chosen to be one. The relation between the twisted quark doublets χ and the physical quark doublet ψ^{phys} is

$$\psi^{\text{phys}}(x) = e^{\frac{i}{2}\omega\gamma_5\tau_3}\chi(x), \quad \bar{\psi}^{\text{phys}}(x) = \bar{\chi}(x)e^{\frac{i}{2}\omega\gamma_5\tau_3}. \tag{5.7}$$

In the above relations the twist angle ω appears. It satisfies $\tan\omega = \mu_l/m_l$, where $m_l = m_0 - m_{\text{crit}}$. m_{crit} is the additive mass renormalization arising from the explicit breaking of chiral symmetry at finite lattice spacing through the Wilson term. Twisted mass fermions are said to be at maximal twist, if the light bare mass is tuned to its critical value, *i.e.* $m_l = 0$, which corresponds to $\omega = \pi/2$. Tuning to maximal twist is a rather technical issue, the basic principle being to find a value m_0 (in practice κ of the corresponding Hopping Parameter Expansion, see Sec. 4.1), such that at given values of the coupling β and the twisted mass μ_l a parity-odd quantity vanishes. If we find such a value, we are at maximal twist, provided the observable is generally non-zero at arbitrary twist angle. The parity-odd observable of choice is the so-called PCAC mass [52, 53, 54]

$$m_{\text{PCAC}} = \frac{\sum_{\vec{x}} \langle \partial_0 A_0^a(\vec{x},t) P^a(0)\rangle}{\sum_{\vec{x}} \langle P^a(\vec{x},t) P^a(0)\rangle}, \quad a = 1,2. \tag{5.8}$$

Here, A_μ and P are the axial current and the pseudo-scalar current, respectively,

$$A_\mu^a(x) = \bar{\chi}_l(x)\gamma_\mu\gamma_5\frac{\tau_a}{2}\chi_l(x), \tag{5.9}$$

$$P^a(x) = \bar{\chi}_l(x)\gamma_5\frac{\tau_a}{2}\chi_l(x), \tag{5.10}$$

where the Pauli matrix τ_a acts in flavor space. If m_{PCAC} is zero all operators that are built from parity-even multiplicatively renormalizable fields are free of $\mathcal{O}(a)$ effects, as demonstrated in Ref. [55]. In particular this means that all operators we use in the context of this work are *automatically* $\mathcal{O}(a)$ improved, *i.e.* no operator-specific improvement has to be done. This fact is a big advantage of the twisted mass formulation of Lattice QCD.
It means that – provided $\mathcal{O}(a^2)$ effects are not too big – we are already close to the continuum limit at moderately large lattice spacing. We would like to state here that empirically we also find that within the statistical accuracy we reach for the observables calculated in the scope of this work, $\mathcal{O}(a^2)$ lattice artifacts are indeed small and sometimes even compatible with zero. In the following we always assume maximal twist since in our calculations we only use gauge field ensembles that were simulated at bare mass values tuned to maximal twist.

5.2 $N_f = 2+1+1$ Twisted Mass Fermions

In the previous section we have only introduced the light quark doublet (u,d). In fact, at the time this thesis work was started also computations with four dynamical quark flavors had

been carried out or were in preparation [56, 45]. Most of the calculations of this thesis were done employing $N_f = 2+1+1$ dynamical quarks. The term $2+1+1$ indicates that we have mass degenerate light quarks plus two non-degenerate flavors of different mass, namely strange and charm quarks.

In the $N_f = 2+1+1$ setup, in addition to the action for the light doublet, we must specify an action for the heavy mass non-degenerate doublet,

$$S_h^{TM} = a^4 \sum_x \bar{\chi}_h(x) \left[D_W + m_{0,h} + i\gamma_5\tau_1\mu_h + \tau_3\mu_\delta \right] \chi_h(x) \tag{5.11}$$

which looks quite similar to the light quark action, Eq. (5.1), The term with μ_δ is responsible for the the mass splitting. As explained in Ref. [57], using this action for the heavy doublet results in the renormalized strange and charm quark masses

$$(m_s)_R = \frac{1}{Z_p}\left(\mu_h - \frac{Z_p}{Z_s}\mu_\delta\right), \tag{5.12}$$

$$(m_c)_R = \frac{1}{Z_p}\left(\mu_h + \frac{Z_p}{Z_s}\mu_\delta\right). \tag{5.13}$$

In the twisted mass action of the heavy doublet, Eq. (5.11), the twisting is done in a flavor non-diagonal fashion, from which a problem arises. The operators creating hadrons with a strange or a charm quark inevitably mix since in physical basis the strange field consists partly of the twisted strange and the twisted charm field in the twisted basis. One way to overcome this mixing is using a different action in the sea sector (*i.e.* in the simulation of the gauge field ensemble) than in the valence quark sector (*i.e.* for the calculation of the propagators needed for the correlation functions of interest). This is discussed in Sec. 5.3.

Apart from tuning to maximal twist, also the masses of the strange and the charm quarks have to be tuned. Again, there are multiple possibilities that only have to satisfy the condition of reproducing the physical strange and charm quark in the chiral limit (and of course also in the continuum limit). The European Twisted Mass Collaboration, providing the gauge field ensembles for this thesis work, follows the strategy of tuning the strange and charm quark masses to values for which the masses of the Kaon and the D meson, m_K and m_D, respectively, assume their physical values.

5.3 Mixed Action Setup

Generally, mixed action has the meaning of using different lattice discretizations (actions) in the valence and sea quark sector. That is, the weight factor $\det M_{\text{sea}}$ in the simulation of the gauge fields is computed using a different action than in the calculation of the quark propagators M_{val}^{-1} from which the correlation functions of interest are constructed. In fact, mixed action is a well-established technique that has been used in various calculations by different lattice collaborations [58, 59, 60, 61].

The main benefit of using a mixed action setup is in general that one can use an action more suitable for the application of interest, *e.g.* possessing better symmetry properties In our particular case mixed action prevents a problematic mixing of the charm and strange flavor mentioned in the previous section.
To this end we use the Osterwalder-Seiler action for the twisted mass heavy doublet in the calculation of quark propagators from which we build our correlation functions. In the simulations of the gauge field ensembles however, the $N_f = 2+1+1$ twisted mass action, Eq. (5.1) and Eq. (5.11), is employed. We refer to the term Osterwalder-Seiler valence fermions on a twisted mass sea for this setup. The Osterwalder-Seiler action reads

$$S^{OS} = a^4 \sum_x \bar{\chi}(x) \left[D_W + m_0^{\mathrm{OS}} + ir\gamma_5 \mu^{\mathrm{OS}} \right] \chi(x), \quad r = \pm 1, \tag{5.14}$$

where m_0^{OS} must be equal to the critical mass m_{crit} of the sea quark action. Notice that this is very similar to the light twisted mass action (5.1), but the quark field χ is no doublet. Of course a matching of the mixed action and the unitary setup has to be performed in order to keep the $O(a)$ improvement. In our case the twisted mass μ^{OS} is tuned such that the values of the Kaon mass m_K and the D meson mass m_D equal the values obtained in the unitary setup, where the action is the same for valence or sea quarks. This can be done directly at the level of the renormalized quark masses, when the ratio Z_p/Z_s is known [see Eq. (5.12) and Eq. (5.13)].

Of course we now have the freedom of choosing the Wilson parameter r in Eq. (5.14). Let us denote the strange (charm) fields in the physical basis associated with $r = +1$ and $r = -1$ s_+ and s_- (c_+ and c_-), respectively. We can use the fields with subscript $+$ or $-$ or combinations of those in the operators of interest. For instance, in the case of the scalar operators $\bar{q}q$ with $q = s, c$ it is advantageous to use a combination of $\bar{q}_+ q_+$ and $\bar{q}_- q_-$, because in this case we do not introduce an additive renormalization constant and therefore not destroy the $O(a)$ improvement [62].

5.4 Calculation of Quark Propagators

As mentioned in one of the previous sections, the lattice quark propagator (on a fixed gauge field configuration) is the inverse of the Dirac matrix [see Eq. (4.27)], a square matrix with

$$\underbrace{4 \times 4}_{\text{spin}} \times \underbrace{3 \times 3}_{\text{color}} \times \underbrace{N_{\mathrm{l}} \times N_{\mathrm{l}}}_{\text{lattice sites}} \tag{5.15}$$

complex entries. This can be a huge number and one may save a lot of effort if not all entries are needed. Let us therefore make the following considerations. In most applications, say for a momentum projection (*cf. e.g.* Eq. (3.3)), we need to sum a propagator $S_{a'a}^{\alpha'\alpha}((\vec{x}', t'), (\vec{x}, t))$ over the sink site $\vec{x}'$. More precisely, we need to Fourier transform with $\sum_{\vec{x}'} \exp[i\vec{p} \cdot (\vec{x}' - \vec{x})]$, *cf.* Eq. (3.3) in combination with Eq. (3.30). For this we need the complete $\vec{x}'$ dependence. Secondly, we are usually – at least that is the case for the work in the scope of this thesis – only

interested in the behavior of correlation functions as a function of the source-sink dependence $t' - t$, so we need the full $x' = (\vec{x}', t')$ dependence. Furthermore, translational invariance tells us that we can simply set x to zero or fix it to some space-time point (lattice site). This amounts to looking for the solution

$$\phi_{a'}^{\alpha'}(x') = S_{a'a}^{\alpha'\alpha}(x', x)\eta_a^\alpha(x)\Big|_{x,\alpha,a \text{ fixed}} \tag{5.16}$$

of the system of linear equations

$$M\phi = \eta. \tag{5.17}$$

Recall again here that the quark propagator S is the inverse of the Dirac matrix M defined in Eq. (4.10). We have suppressed the implicit dependence of ϕ on the choice of x, α and a. $\eta_a^\alpha(x)$ is a spinor field with some normalization condition, here chosen

$$\eta_b^\beta(y)^*\eta_a^\alpha(x) = \delta_{ab}\delta^{\alpha\beta}\delta_{xy}. \tag{5.18}$$

δ is the Kronecker delta symbol with the standard definition. Now we simply need to solve a (huge) system of linear equations for which iterative solvers, *e.g.* the conjugate gradient algorithm, are well-suited. The fact that M is sparse is also particularly helpful. Since the algorithms that solve the system of equations are described in much detail in mathematical standard literature (*e.g.* [63]) we do not discuss the details of these algorithms here.

In fact, solving for fixed x, α and a as in Eq. (5.16) drastically reduces the amount of complex numbers that actually have to be calculated. Hence this approach is particularly advantageous regarding memory management, because in practice we have to store propagators on hard disk, other permanent storage or at least have them in the computer memory (RAM) during the time of the computation.

When the field η in Eq. (5.16) has only support on one lattice site, one generally calls it a point source. However, in order to increase overlap with the ground state (see Sec. 3.5) the source η is often spatially extended by means of gauge invariant quark smearing. The interested reader is pointed to Ref. [64], where more advanced interpolating fields are constructed in order to explore also excited baryons. We still refer to extended point sources as point sources.

It is sometimes useful, in particular when we need the full dependence on the source site x, to estimate the full quark propagator (*i.e.* the full inverse of the Dirac matrix) stochastically. Consider therefore N source vectors with random entries

$$\xi^i = \sum_{x,\alpha,a} \eta_a^{\alpha,i}(x), \quad i = 1, \ldots, N, \tag{5.19}$$

where we impose

$$\lim_{N\to\infty} \frac{1}{N} \sum_{i=1}^{N} \eta_b^{\beta,j}(y)^*\eta_a^{\alpha,i}(x) = \delta_{ab}\delta^{\alpha\beta}\delta_{xy}\delta_{ij}, \tag{5.20}$$

Those are the normalization and statistical independence condition. We call ξ a stochastic source or (stochastic) noise vector. Such a noise vector can be realized by choosing $\eta_a^{\alpha,i}(x)$ randomly and uniformly as ± 1 ($Z(2)$ noise). Other common choices are $Z(4)$ noise $\{\exp(i\,\pi/4)$, $\exp(i\,3\pi/4)$, $\exp(i\,5\pi/4)$, $\exp(i\,7\pi/4)\}$ or $U(1)$ noise, *i.e.* $\exp(i\alpha)$ with α uniformly chosen in $[0, 2\pi]$.

The solutions of the systems of linear equations

$$M\phi^i = \xi^i, \quad i = 1, \ldots, N, \tag{5.21}$$

provides a means for the stochastic estimation of the full propagator,

$$M^{-1} = \lim_{N\to\infty} \frac{1}{N} \sum_{i=1}^{N} \left(\xi^i\right)^* \phi^i, \tag{5.22}$$

which follows from Eqs. (5.19)-(5.21). Of course in practice we always have a finite number of stochastic sources, which introduces an error $\sim 1/\sqrt{N}$. For typical applications $O(10)$ sources per gauge field configuration is often sufficient in order to have an error on the observable of interest that is dominated by the gauge noise, which induces an error $\sim 1/\sqrt{N_{\text{gauge}}}$, see Sec. 4.1. We would like to repeat here that the gauge noise is the error due to averaging over a finite number of gauge field configurations.

The stochastic error can be reduced, in many cases significantly, by imposing some of the Kronecker delta symbols in Eq. (5.20) explicitly in the source which is called dilution. The most common types are

- time slice dilution: $\xi^i_{t_0} = \xi^i \delta_{t t_0}\Big|_{t_0 \text{ fixed}}$
- spin dilution: $\xi^{\alpha_0 i} = \xi^i \delta_{\alpha\alpha_0}\Big|_{\alpha_0 \text{ fixed}}$
- color dilution: $\xi^i_{a_0} = \xi^i \delta_{a a_0}\Big|_{a_0 \text{ fixed}}$

and combinations thereof. It is easy to imagine there is a great variety, *e.g.* spatial dilution in one or more directions, but in the scope of this thesis those dilution types are not important and shall only be mentioned here for completeness.

5.5 Exponential Decrease of the Signal-to-Noise Ratio in Nucleon Correlation Functions

In this section we would like to review a problem affecting correlation functions of the nucleon. In [32] the interested reader can find a sound explanation of the issue, of which we now summarize the basic aspects. Note that the discussion can be taken over to baryons in general, however since this thesis is only concerned with nucleon structure we do not want to extend

the discussion here.

Based on the empiric finding that the quark 2-point correlation function $[q(\vec{x},t)\bar{q}(0)]_{\{U\}}$, *i.e.* the quark propagator on a constant gauge field background has an asymptotic decay like $e^{-m_\pi/2\,t}$ we can argue that the large-t behavior of the nucleon 2-point correlation function in the background of a constant gauge field goes essentially like $e^{-3m_\pi/2\,t}$. Since the nucleon 2-point function in the average over gauge field configurations is known to behave asymptotically like $e^{-m_N\,t}$, where m_N is the nucleon mass, [*cf.* Eq. (3.8)], an additional decrease $e^{-(m_N-3m_\pi/2)\,t}$ must originate from the average over the gauge field configurations.
In the average over (a finite number of) gauge fields, we thus obtain a signal that decreases exponentially with the source-sink separation t. The statistical error due to a finite number of gauge field configurations, though, is independent of t. As a consequence, the signal-to-noise ratio decreases exponentially fast with t, such that in order to achieve a certain precision we need the average over more statistically independent gauge field configurations when the source-sink separation is increased. Since also 3-point functions of the nucleon are affected by this problem, in practice one cannot go beyond a certain source-sink separation when calculating nucleon matrix elements of local operators as done in this thesis.
Therefore, excited state contributions need to be examined and the compromise is often to choose a source-sink separation that is as small as possible to obtain a precise estimate of the matrix element of interest and at the same time as large as necessary such that contributions to excited states are sufficiently suppressed, which usually means small compared to the statistical uncertainty.

In the subsequent section, we outline a method that is usually applied in order to examine the excited state contributions at a fixed source sink separation, and discuss the problems which arise from using this method.

5.6 Excited State Contamination and Plateau Fits

In this section we would like to illustrate conceptually a method usually employed to obtain matrix elements from ratios of 3-point and 2-point correlation functions of the nucleon and at the same time deal with excited states. However, from using this method a problem arises, as we learn in this section.

Consider a ratio of a nucleon 3-point and a 2-point function, which gives a matrix element in the limit of large euclidean time separations, as discussed in Sec. 3.3. As we learn in the previous section the signal-to-noise ratio of those correlation functions decreases exponentially with the source-sink separation and thus in practice we cannot perform this limit. Note that we also have the restriction of a finite lattice extent in time, but this restriction is usually significantly less severe. Hence our ratios are subject to excited state effects, see Sec. 3.4. Often the term excited state contamination is used due to the fact that this is in most applications an unwanted effect.

In practice, as repeatedly discussed in the remaining part of this thesis, one usually works

with a fixed source-sink separation such that the ratio of a 3-point and a 2-point correlation function is only a function of the insertion time τ. According to Eq. (3.24), we should observe contributions from the first excited state – assuming the latter gives the dominant contribution – that decrease exponentially when the distance to source and sink is increased. Therefore, right in the center between source and sink we expect the least contributions. In fact, if the data is (approximately) constant, *i.e.* exhibits a *plateau*, in a range centered between source and sink, we can assume that contributions from excited states are strongly suppressed. We illustrate this with a toy model. In Fig. 5.1 we plot a ratio modeled to behave like Eq. (3.24). The parameters of this toy model are chosen such that the data does not exhibit an good plateau – which is a realistic situation – but one may argue that the data in the middle between is sufficiently flat such that excited state effects are negligible compared to other systematic effects or the statistical accuracy. Then a constant fit of the data in the plateau region yields the matrix element of interest. As we see in the figure, the value obtained from a least squares fit (the solid line), does not agree with the value of the matrix element, which we use as input in our toy model, corresponding to the dashed line. In practice the fit also has an error and its value may agree with the matrix element within errors, but one should be aware that even though a plateau fit has been performed there is still a remaining systematic effect when the plateau is rather short or only approximately a plateau.

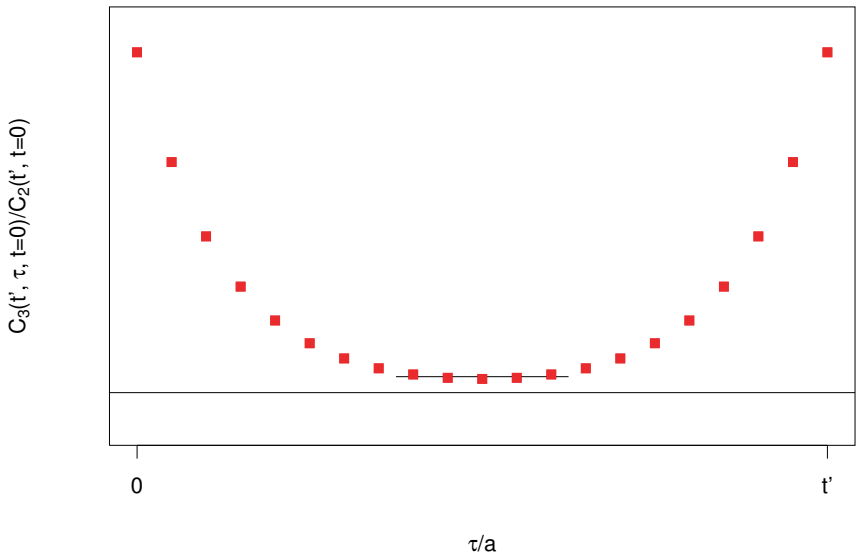

Figure 5.1: Example of a plateau fit. The red squares show the data of a toy model modeling the ratio of a 3-point and a 2-point correlation function including the leading excited state effects [*cf.* Eq. (3.24)]. The solid line indicates a showcase plateau fit and the dashed line indicates the value of the nucleon matrix element, the asymptotic value of the ratio, which is an input parameter in the toy model.

Note that in lattice QCD computations there are statistical fluctuations and we usually have a limited statistical precision. This may result in data to look like a plateau in some range of in-

sertion time but when the precision is increased it may as well turn out not to exhibit a plateau. This means excited state effects can be masked by statistical fluctuation and uncertainty. In order to appropriately account for excited state contamination we therefore need a good statistical accuracy. In addition, one should compare the plateaus from computations using different source-sink separations in order to clarify whether a plateau has been reached. This subject will be discussed in chapters 7 and 8.

5.7 Evaluation of Correlation Functions

In Chapter 3 we have explained how to construct nucleon matrix elements of local operators from suitable ratios of nucleon 2-point and 3-point correlation functions. Moreover, we have demonstrated how those correlation functions read in terms of quark propagators. In practice however, in order to be competitive, one has to make certain restrictions, the reason being that instead of resolving all dependencies in the 3-point function of the nucleon one would rather prefer to fix one or more variables and repeat the calculation for different values of the lattice spacing and pion mass, in order to have a sound chiral extrapolation and to perform the continuum limit properly. We discuss this in detail in this section.

5.7.1 Connected Diagrams

In this section we discuss how to evaluate the connected part of the nucleon 3-point correlation function. For the discussion we restrict to simple case where the operator has the form $\bar{d}(x)Xd(x)$, *i.e.* is a is a local operator, say a γ matrix or a twist-two operator, Eq. (2.25). We also use the interpolating field of the proton, Eq. (3.25) or Eq. (3.27), respectively. Let us rewrite the corresponding 3-point function, Eq. (3.34), in terms of quark propagators.

$$\begin{aligned} C_3^{\alpha'\alpha}(x',y,x)\Big|_{CONN} = \sum_{\{U\}} \bar{\zeta}_{\alpha' B' C' D'} \zeta_{\alpha B C D} \\ \times X^{E'E}(y) \Big\{ S_u^{B'B}(x',x)\big|_{\{U\}} S_d^{C'E}(x',y)\big|_{\{U\}} S_d^{E'C}(y,x)\big|_{\{U\}} S_u^{D'D}(x',x)\big|_{\{U\}} \\ - S_u^{B'D}(x',x)\big|_{\{U\}} S_d^{C'E}(x',y)\big|_{\{U\}} S_d^{E'C}(y,x)\big|_{\{U\}} S_u^{D'B}(x',x)\big|_{\{U\}} \Big\} \end{aligned} \tag{5.23}$$

The symbols (more precisely tensors) ζ and $\bar{\zeta}$ are defined according to Eq. (3.29). Note that the spin and color indices (with exception of α) are combined in the capital Roman indices and we use the flavor as a subscript. In fact, we need the momentum-projected 3-point function, Eq. (3.12), *i.e.* need to sum over x' and y, since we would like to study the momentum dependency of the nucleon form factors related to nucleon matrix elements,

$$C_3^{\alpha'\alpha}(\vec{p}',t',\tau;\vec{p},x)\Big|_{CONN} = \sum_{\vec{x}',\vec{y}} e^{i\vec{p}'\cdot(\vec{x}'-\vec{y})}\; e^{i\vec{p}\cdot(\vec{y}-\vec{x})}\; C_3^{\alpha'\alpha}(\vec{x}'-\vec{y},t'-\tau;\vec{y}-\vec{x},\tau-t). \tag{5.24}$$

As discussed before, due to translational invariance x can be fixed, which is usually done. Therefore, the basic quark propagators we need for the computation of the above 3-point function are the following three,

$$S_u(x',x)\Big|_{x=\text{const}},\ S_d(y,x)\Big|_{x=\text{const}},\ S_d(x',y). \tag{5.25}$$

The first two can be computed as point source propagators, see discussion in Sec. 5.4. For $S_d(x',y)$ we need the propagator from all points y to all points x', otherwise the momentum projection cannot be performed.
Such a propagator is called all-to-all propagator and is typically not easy to calculate. One would either need point source propagators from all the lattice points, which is most certainly unfeasible, because in this case one needs the propagators from all lattice sites of the whole volume on every gauge field configuration, or one needs to estimate the all-to-all propagator stochastically, according to Eq. (5.22). Actually, with the restriction of dilution, the latter can be done, which we demonstrate in Chapter 6. Even though estimating the all-to-all propagator naturally seems the easiest solution, it is predominantly not employed, for reasons that are also explained in Chapter 6.

Let us now outline the standard method for the evaluation of the 3-point function [65], which is not so easy to see from the expression (5.23). We can write the r.h.s. of expression (5.24) for the 3-point contraction Eq. (5.23) as

$$C_3^{\Gamma}(\vec{p}',t',\tau;\vec{p},x)\Big|_{CONN} = \sum_{\vec{x}',\vec{y}} e^{i\vec{p}'\cdot(\vec{x}'-\vec{y})}\ e^{i\vec{p}\cdot(\vec{y}-\vec{x})}\ \Sigma^{C'C}(x',x;\Gamma)\ X^{EE'}\ S_d^{C'E}(x',y)S_d^{E'C}(y,x), \tag{5.26}$$

where we have ignored the summation (integral) over the gauge field configurations since it is not important for the discussion and introduced the shorthand Σ

$$\Sigma^{C'C}(x',x;\Gamma) = \Gamma_{\alpha\alpha'}\,\bar{\zeta}_{\alpha'B'C'D'}\zeta_{\alpha BCD}\left[S_u^{B'B}(x',x)S_u^{D'D}(x',x) - S_u^{B'D}(x',x)S_u^{D'B}(x',x)\right], \tag{5.27}$$

which contains everything that depends on the sink position. We can now define a "generalized propagator" containing everything except the operator and the d quark propagator with source point x and sink at the operator,

$$S_G^{CE}(t',x,y,\vec{p}';\Gamma) = \sum_{\vec{x}'} e^{i\vec{p}'\cdot(\vec{x}'-\vec{y})}\ \Sigma^{C'C}(x',x;\Gamma)\ S_d^{C'E}(x',y). \tag{5.28}$$

We now demonstrate that the generalized propagator is in fact a quark propagator, but of a source that depends on the sink timeslice t', the sink momentum $\vec{p}'$ and the interpolating field (here characterized by the particular form of the symbol ζ) as well as the spin projector Γ. Imagine those variables are fixed. Then in principle y is the only free variable left. We can make use of the γ_5 hermiticity of the Dirac matrix,

$$\gamma_5 S_d^{\dagger}(x',y)\gamma_5 = S_u(y,x'), \tag{5.29}$$

to rewrite the propagator $S_d^{C'E}(x', y)$. Note that in the twisted mass formalism we have a flavor change between d and u, which is not there for plain Wilson fermions.
Defining a slightly modified generalized propagator

$$\tilde{S}_G(t', x, y, \vec{p}'; \Gamma) := \gamma_5 S_G^\dagger(t', x, y, \vec{p}'; \Gamma) \tag{5.30}$$

$$= \sum_{\vec{x}'} e^{-i\vec{p}'\cdot(\vec{x}'-\vec{y})}\ \gamma_5 S_d^\dagger(x', y)\ \Sigma^\dagger(x', x; \Gamma) \tag{5.31}$$

$$= \sum_{\vec{x}'} e^{-i\vec{p}'\cdot(\vec{x}'-\vec{y})}\ S_u(y, x')\ \gamma_5\ \Sigma^\dagger(x', x; \Gamma), \tag{5.32}$$

the 3-point function can be written in a compact form,

$$C_3^\Gamma(\vec{p}', t', \tau; \vec{p}, x)\Big|_{CONN} = \sum_{\vec{y}} e^{i\vec{p}\cdot(\vec{y}-\vec{x})}\ \mathrm{Tr}\ \left[\tilde{S}_G^\dagger(t', x, y, \vec{p}'; \Gamma)\gamma_5 X\, S_d(y, x)\right]. \tag{5.33}$$

Applying the Dirac matrix $M_u(z, y)$ to the generalized propagator $\tilde{S}_G$ we obtain

$$\mathcal{S}(z, x, \vec{p}'; \Gamma) := M_u(z, y)\tilde{S}_G(x', x, y, \vec{p}'; \Gamma) \tag{5.34}$$

$$= \sum_{\vec{x}'} e^{-i\vec{p}'\cdot(\vec{x}'-\vec{y})}\ \delta\left(z, (\vec{x}', t')\right)\ \Sigma^\dagger(x', x; \Gamma), \tag{5.35}$$

which is commonly called sequential source. Thus the calculation of the generalized propagator can be done constructing the sequential source and computing the propagator thereof, because M_u^{-1} applied to $\mathcal{S}$ clearly gives $\tilde{S}_G$. Once this so-called sequential propagator is calculated, the contraction is done in a simple manner, see Eq. (5.33). This contraction does not depend on the particular form of the operator, provided it is of the form $\bar{d}Xd$. However, since we have fixed t' in this approach, we have to examine contributions from excited states. We illustrate the fixed sink method graphically in the left panel of Fig. 5.2, where we represent the sequential propagator by a shaded area. The drawing also indicates why the term "backward propagator" is often used for the generalized propagator. In this spirit, the other propagator that is represented by the line from the source to the operator is called "forward propagator". In fact, we use the terms frequently for all propagators that are not the generalized propagator and originate at the source point.

Note that in principle there is also another way to compute the connected 3-point function using a sequential propagator, where τ, $\vec{p}$ and the operator $\mathcal{O}(y) = \bar{d}(y)Xd(y)$, where $y = (\vec{y}, \tau)$, are fixed. In this case the generalized propagator is defined

$$S_G^{C'C}(x', x, \tau, \vec{p}; X) := \sum_{\vec{y}} e^{-i\vec{p}\cdot(\vec{y}-\vec{x})}\ S_d^{C'E}(x', y) X^{E'E}\ S_d^{E'C}(y, x) \tag{5.36}$$

and therefore the sequential source reads

$$\mathcal{S}(z, x, \tau, \vec{p}; \mathcal{O}) = \sum_{\vec{y}} e^{-i\vec{p}\cdot(\vec{y}-\vec{x})}\ \delta\left(z, (y, \tau)\right)\ X\, S_d(y, x). \tag{5.37}$$

The contraction of the 3-point function in terms of the sequential propagator is written

$$C_3^{\Gamma}(\vec{p}', t' - \tau; \vec{p}, \tau - t)\Big|_{CONN} = \Gamma^{\alpha\alpha'} \bar{\zeta}_{\alpha' B' C' D'} \zeta_{\alpha B C D} \sum_{\vec{x}'} e^{i\vec{p}'\cdot(\vec{x}'-\vec{y})} \Big\{ S_u^{B'B}(x', x) S_G^{C'C}(x', x, \tau, \vec{p}; \mathcal{O}) S_u^{D'D}(x', x) - S_u^{B'D}(x', x) S_G^{C'C}(x', x, \tau, \vec{p}; \mathcal{O}) S_u^{D'B}(x', x) \Big\} \tag{5.38}$$

This method is known as fixed current method. Note that the contraction looks very similar to the 2-point contraction, see Eq. (3.31) and Fig. 3.1. The fixed current method is illustrated in the right panel of Fig. 5.2, where we represent the sequential propagator by a shaded area.

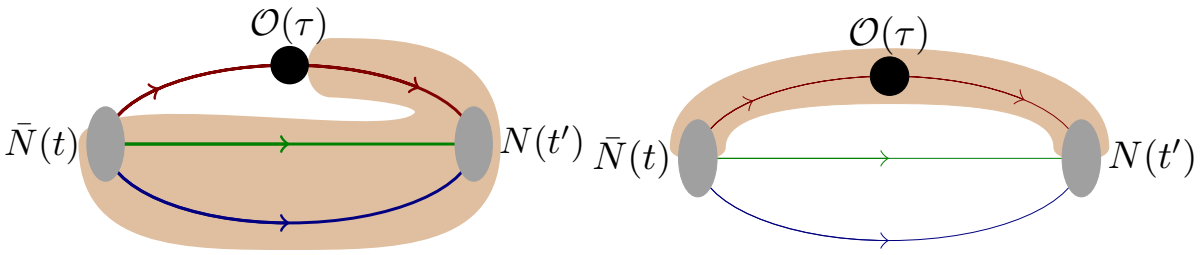

Figure 5.2: left: Illustration of the sequential method with fixed sink. **right:** Illustration of the sequential method with fixed operator/current. In both cases the shaded area indicates the sequential (generalized) propagator.

The generalized propagator for an operator of the form $\bar{u}Xu$ and the proton interpolating field Eq. (3.27) looks more complicated, because there are more contractions. Since it is, however, not essential for the comprehension of the method, we quote the corresponding expressions for the sequential sources, the generalized propagators and the 3-point correlation function in terms of the forward propagators and the generalized propagator in Appendix 3.

5.7.2 Efficient Evaluation of Quark-Disconnected Diagrams

For the computation of quark-disconnected diagrams we inevitably need all-to-all propagators, being typically very noisy. In the Wilson twisted mass formalism we can make use of a special noise-reduction technique for disconnected diagrams of operators of type

$$\bar{u}^{\mathrm{tw}} X u^{\mathrm{tw}} - \bar{d}^{\mathrm{tw}} X d^{\mathrm{tw}}, \tag{5.39}$$

in the twisted basis at maximal twist, where $\bar{q}Xq$ (with $q = u, d$) can be any local operator. Typically and in the scope of this thesis X is a Γ matrix or (the kernel of) a twist-two operator. This noise reduction method, together with another more flexible but less powerful method based on the hopping parameter expansion, is explained in Ref. [42]. Since it is of importance for this thesis, we review its main aspects below.

Before we do so, we would like to state that it is extremely beneficial that the scalar operator $\bar{u}u + \bar{d}d$, which we need to evaluate for the scalar content of the nucleon, falls under this category, since

$$\bar{u}\mathbb{1}u + \bar{d}\mathbb{1}d = \bar{u}^{\mathrm{tw}} i\gamma_5 u^{\mathrm{tw}} - \bar{d}^{\mathrm{tw}} i\gamma_5 d^{\mathrm{tw}}. \tag{5.40}$$

In order to evaluate disconnected diagrams thereof, in twisted basis we basically need to estimate the difference of two propagators (multiplied by the part X of the operator) in order to obtain a small number, which is is demanding in a numerical calculation since the noise of the two terms adds up whereas there are cancellations in the signal. However, we can use the following trivial identities of the Dirac matrix $M_{u,d}$ in twisted basis

$$M_u - M_d = 2i\gamma_5\mu_l, \tag{5.41}$$

$$M_u^{-1} - M_d^{-1} = -M_d^{-1}\left(M_u - M_d\right)M_u^{-1} \tag{5.42}$$

to obtain

$$\begin{aligned} M_u^{-1} - M_d^{-1} &= -2i\mu_l M_d^{-1}\gamma_5 M_u^{-1}, \\ &= -2i\mu_l\gamma_5\left(M_u^{-1}\right)^\dagger M_u^{-1}. \end{aligned} \tag{5.43}$$

The dagger in the second row affects spin, color and lattice sites and we have used the identity $\gamma_5(M_u^{-1})^\dagger\gamma_5 = M_d^{-1}$ which holds for the light twisted mass doublet. Thus we have replaced the difference of two propagators by the product of the two propagators. To fully appreciate the advantages resulting from this equality, we consider the stochastic estimate of the r.h.s of Eq. (5.43).

Recalling the stochastic estimate of a quark propagator, Eq. (5.22), we obtain

$$\mathrm{Tr}\left[X\left(M_u^{-1} - M_d^{-1}\right)\right] = -2i\mu_l\,\mathrm{Tr}\left[X\left(\xi^*\phi\right)^\dagger\left(\xi^*\phi\right)\right], \tag{5.44}$$

$$= -2i\mu_l\,\mathrm{Tr}\left[X\phi^\dagger\phi\right]. \tag{5.45}$$

In the last line we have used $\xi^*\xi = 1$ and we assumed implicitly a sum over stochastic sources and suppressed the spin, color and lattice site indices. Expression (5.45) contains no stochastic noise vector and therefore exhibits significantly less noise than in the case where we estimate both propagators in the difference on the l.h.s. of Eq. (5.44) separately using Eq. (5.22).
Strictly speaking, the equality Eq. (5.44) holds in the limit of infinitely many stochastic sources. In practice, as we will see later, a finite number of stochastic sources is fully sufficient when dealing with a finite number of gauge field configurations, since we have a statistical error independent of the number of sources.
This method enables us to give a precise result for observables that have quark-disconnected pieces or are even purely disconnected, as we demonstrate in Chapter 8.

5.7.3 The Generalized Eigenvalue Method

In this section we would like to review a useful variational method capable of dealing with excited states. It can be employed to determination of their energies or to eliminate excited state contributions in hadronic 2-point functions and matrix elements, the latter being of interest in the work presented in Chapter 7. This tool even allows for the calculation of excited hadron matrix elements, which however is beyond the scope of this thesis. It was first developed in [66] and later refined in [67, 68]

The basic principle of the generalized eigenvalue (GEV) method is to solve the eigenvalue problem $Av = \lambda Bv$ of two arbitrary matrices A and B, where v is a generalized eigenvector and λ the respective generalized eigenvalue. For our purposes it is more convenient to write it in the following way,

$$C(t)v_n(t_0,t) = \lambda_n(t_0,t)C(t_0)v_n(t_0,t), \tag{5.46}$$

It relates the $N \times N$ matrix of correlation functions $C(t)$ at euclidean time t to the matrix of the same correlation functions $C(t_0)$ at some fixed time t_0. Provided none of the eigenvalues is degenerate, which we implicitly assume from now on, we have N different eigenvalues and eigenvectors $v_n(t_0,t), \lambda_n(t_0,t), n \in 1,\ldots,N$. Clearly, when C is a matrix of (spin-projected) hadronic 2-point functions it possesses a spectral representation, *cf.* the spectral representation of the nucleon 2-point function, Eq. (3.4),

$$\begin{aligned} C_{ij}(t) &= \sum_{n=1}^{\infty} e^{-E_n t} \left(\Omega_n\right)_i \left(\Omega_n^*\right)_j, \\ i,j &= 1,\ldots,N, \quad E_n < E_{n+1}. \end{aligned} \tag{5.47}$$

Then the generalized eigenvalues that solve the generalized eigenvalue problem (5.46) are obviously

$$\lambda_n(t_0,t) = e^{-E_n(t-t_0)}. \tag{5.48}$$

This means that the solution of the $N \times N$ GEV problem yields the energies E_n of the first N eigenstates, in the sense of Eq. (3.4). This statement is only strictly correct if there are exactly N eigenstates, though. In general there are corrections $\mathcal{O}(e^{-(E_{N+1}-E_n)t})$ which however vanish exponentially as t grows. In practice this means that when we choose a t_0 where contributions from energy levels E_n, $n \geq N$ are sufficiently suppressed, we can trust the first $N-1$ solutions. The corrections to the energy E_N of the N^{th} eigenstate, however, may not be negligible if $E_{N+1} - E_N$ is small. Let us emphasize that these statements are of rather qualitative nature and the size of the corrections always has to be inspected in practice, since the factors Ω_n and in most cases also the energies above the lowest-energy state E_n, $n > 1$ are a priori unknown.

As a side remark, when those higher energy levels are known experimentally the energy of a state in a lattice QCD calculation can still be affected by systematic factors like lattice artifacts, finite size effects or unphysical quark mass. Hence the GEV method is extremely useful for

excited hadron spectroscopy on the lattice.

In addition to energy levels the GEV method is also capable of calculating hadronic matrix elements. This procedure, detailed in Ref. [67], works as follows. As a first step the GEV is solved for the correlation matrix $C_{ij}^{(2)}(t)$ of the 2-point function yielding the eigenvectors $\lambda_n(t_0, t)$ and the eigenvectors $v_n(t_0, t)$ of the first N eigenstates. In a second step the eigenvectors of the GEV problem are used to diagonalize the 3-point correlation matrix,

$$C^{(3),\mathrm{opt}}(t) = V^T C_{ij}^{(3)}(t) V, \quad V = \{v_1(t_0, t), v_2(t_0, t), ..., v_N(t_0, t)\}\,. \tag{5.49}$$

This of course implies the correlation matrices $C^{(2)}$ and $C^{(3)}$ are constructed using the same set of hadron creation and annihilation operators, *i.e.* the same set of interpolating fields for the hadron states of interest. To put it another way: we use the solution of the eigensystem of the 2-point function to construct an optimal operator that creates only the first N eigenstates of interest, up to corrections. The corrections to the matrix elements are of the order $\mathcal{O}(e^{-(E_{N+1}-E_n)t_0})$, see the aforementioned reference [67]. This suggests not only to choose t_0 moderately large but also to repeat the GEV analysis for different t_0 in order to have an estimate on the size of the corrections.

6 New Computational Strategies for Connected Nucleon 3-point Functions

In chapters 7 and 8 we discuss the computation of nucleon matrix elements as the asymptotic limit of ratios of nucleon 2-point and 3-point correlation functions. We outline in Sec. 5.7 how the 3-point functions can be evaluated in lattice QCD. In this chapter we explain the technical aspects of the computation of connected nucleon 3-point correlation functions in more detail and in particular focus on a new stochastic method.

Some of the methods to calculate connected nucleon 3-point functions were outlined in Chapter 4 and have been applied in Chapter 7 and Chapter 8. Software development for application and testing of the stochastic method mentioned in Sec. 5.7, *i.e.* the stochastic estimation of the all-to-all propagator appearing in the expression Eq. (5.26), has been an important part of this thesis work. Therefore – despite the fact that it is a rather technical issue – this chapter is devoted to this aspect of the work presented in this thesis. After all, in lattice QCD investing large effort in code development as well as new algorithms and methods is an essential and most important element.

We start with reviewing the 3-point function with the all-to-all propagator stochastically estimated in Sec. 6.1. There, we also point out advantages and and disadvantages compared to the standard method, the sequential source method with fixed sink, see Sec. 5.7.1. We perform a feasibility test in Sec. 6.2 and conclude with discussing and testing other beneficial properties in Sec. 6.3.

6.1 Stochastic Method vs. Sequential Source Method

Let us consider the connected piece of the nucleon 3-point function [see *e.g.* Eq. (5.23)], which we rewrite here for convenience

$$C_3^{\Gamma}(\vec{p}', t, \vec{p}, \tau)\Big|_{conn} = \sum_{\vec{x}', \vec{y}} e^{-i\vec{p}'\cdot\vec{x}'} e^{-i\vec{p}\cdot\vec{y}} C_3^{\alpha'\alpha}\left((\vec{x}', t'), (\vec{y}, \tau), 0\right)\Big|_{CONN}, \tag{6.1}$$

where we have fixed the source point x to zero. As explained in Sec. 5.7.1, the application of the sequential method involves the calculation of sequential propagators where the momentum $\vec{p}'$ at the sink, the sink time slice t' and the source position x are fixed. Thus, in order to vary $\vec{q} = \vec{p}' - \vec{p}$ we can vary $\vec{p}$, whereas for every new value of $\vec{p}'$ new sequential propagators have to be computed. The same is true for the spin projector Γ. One would have to compute

a full basis of 16 Γs in order to resolve the entire spin structure of the 3-point function. The stochastic estimation of the all-to-all propagator appearing in the 3-point function frees us from choosing a sink momentum and a spin projector. For better comprehension we illustrate both the sequential method with fixed sink and the stochastic method in Fig. 6.1.

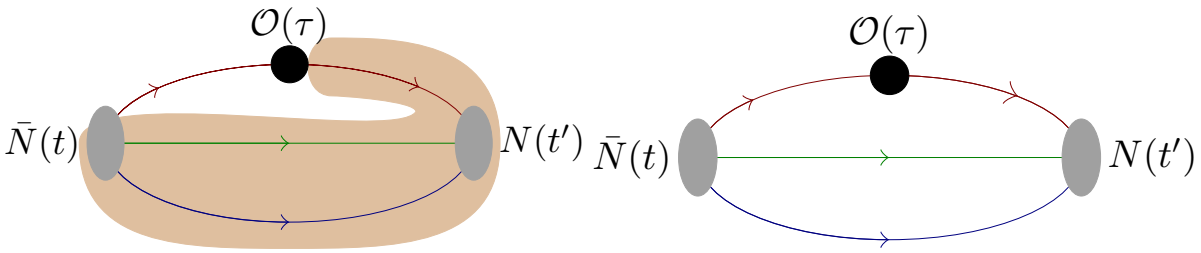

Figure 6.1: left: Illustration of the sequential method with fixed sink. The sequential propagator is indicated by the shaded area. **right:** Illustration of the stochastic method. The dashed line corresponds to the stochastically estimated propagator.

When using the stochastic method, a sizable stochastic noise may make it necessary, though, to fix the sink time slice. Note that we use point source forward propagators and therefore the source position x is fixed. Nevertheless, in principle one can add forward propagators (see Sec. 5.7.1 for the notation) from different source positions. Provided that there is not too much correlation between two or more positions (on the same time slice), we can use additional forward propagators to add statistics (and consequently reduce the gauge noise) without the need of new stochastic propagators.

Another important aspect is the variation of the source-sink separation. In the previous chapters it has become clear that in order to properly account for excited state contributions, one needs more than one source-sink separation. In principle when using stochastic sources that have support on the whole lattice volume, we can resolve any source-sink separation, but given the more realistic case of time slice stochastic sources (at the sink) one can still do so by just moving the point source away from the sink. This of course requires new inversions concerning the forward propagators, but the stochastic propagators, of which we need more than one for a corresponding point source and which therefore provide the main computational effort, can be reused.

It is worthwhile mentioning that in the sequential method also the hadron, more precisely the interpolating field, has to be fixed, a restriction that we are free of when using the stochastic method. Thus the stochastic method would be the most natural choice if one plans to calculate 3-point functions of several hadrons or use different interpolating fields for the same hadron, say in order to apply a variational method like the generalized eigenvalue (GEV) method that could be employed to resolve excited state effects or even to compute excited hadron matrix elements.

The main disadvantage of the stochastic method is as a matter of fact the stochastic noise, which can result in more computational effort compared to the standard method (using a single projector, source-sink separation and interpolating field). Note however that – taking into

account the freedom and versatility mentioned above – one may be willing to invest additional computational effort, even say about two orders of magnitude.

Thus, all considerations lead to the question what the size of the stochastic noise is and how it depends on the parameters of the lattice calculation. In particular, the most important aspect one should worry about is the volume dependence, because there is no reason to believe that the stochastic noise depends on the lattice spacing and the quark mass on which however the gauge noise is expected to depend.

6.2 Test of the Stochastic Method - Feasibility Study

Inspired by a study by another group, where this method was applied [69], we use stochastic time slice sources at the sink time slice. In principle one could as well put the stochastic noise vector at the operator insertion time slice τ, but note that when we use time slice sources this prevents us from varying τ, moreover we want to compare to the usual fixed sink method, where the sink time slice is fixed. We would like to remark here that in terms of full inversions, one spin and color diluted stochastic source per configuration corresponds to approximately the same computational effort as the standard method when neglecting the computational cost of generating the sequential source, which is a good approximation, since this procedure is mostly negligible compared to the inversions.

The size and the volume scaling of the stochastic noise cannot easily be predicted analytically, *e.g.* as in the case of the one-end trick for light pseudo-scalar mesons, the reason being that only one part (the all-to-all propagator) in the 3-point is actually estimated stochastically, whereas all the other propagators are calculated "exactly".

The most important questions here are on the one hand how many stochastic sources we need in order to be competitive with the standard method with respect to the error, when using the same number of gauge field configuration in both approaches. In other words, how many inversions of stochastic noise vectors are needed in order to render the stochastic noise negligible compared to the gauge noise? On the other hand we would like to know how the stochastic noise scales with the volume. Or correspondingly, do we need more or less stochastic sources to make the stochastic noise negligible compared to gauge noise, when the volume is increased. Recall that the statistical error for stochastic estimates consists of gauge noise and stochastic noise. The only fact we know is that in the limit of infinitely many stochastic sources the stochastic noise is absent. In practice for most applications the gauge noise is dominating already for $O(10)$ stochastic sources.

We do not expect the stochastic noise to depend crucially on the number of dynamical flavors. We can thus perform a study in the $N_f = 2$ formalism and expect the conclusion to hold also in the case of four dynamical flavors of twisted mass fermions, $N_f = 2 + 1 + 1$. The reason is that in the $N_f = 2$ case we have a series of different volumes at the same value of the lattice spacing, $a \approx 0.080$ fm, and the pion mass, $m_\pi \approx 300$ MeV, at our disposal. The corresponding gauge field ensembles were generated by the ETM collaboration [42]. This allows us to thoroughly

study the volume dependence of the stochastic noise. Of course the stochastic noise depends on the operator that appears in the 3-point function. Hence we consider a simple quantity first, the nucleon axial charge g_A, see Sec. 2.2.1.

A standard analysis using $N_f = 2$ twisted mass fermions at maximal twist including the calculation of g_A exists and was published in [70]. We performed an analysis using the stochastic method on a fixed number of gauge field configurations $N_{\text{gauge}} = 200$. Results are shown in Fig. 6.2 where we show the relative error of g_A (to be understood as the error of the plateau fits) as a function of the number of stochastic sources for three lattice volumes, $V = L^3 \times T$, with $T = 2L$ and $L/a = 16, 24, 32$. The source-sink separation is $12a$, corresponding to about 0.96 fm in physical units. We compare to the sequential method for the two larger volumes, where calculations with the same source-sink separation of $12a$ are available. We use a fixed number of gauge field configurations $N_{\text{gauge}} = 200$ in all cases in order to study the scaling of the stochastic noise. Note that we do not show errors of the errors, since the latter are hard to estimate reliably, and we are only interested in the qualitative scaling with the number of sources. We observe that already at a number of stochastic sources, $N_S \gtrsim 3$, the level of the sequential error is reached, *i.e.* the gauge noise is dominant.

It can be clearly seen that the stochastic method is equivalent to the sequential method when using 4 or more stochastic sources. It should be mentioned however that we have averaged over proton and neutron correlation functions and used 3 operators, $\gamma_5\gamma_k$, $k = 1, 2, 3$, and correspondingly 3 spin projectors, $1/2\,(1 + \gamma_0)i\gamma_5\gamma_k$, $k = 1, 2, 3$, for the calculation of g_A, which effectively reduces the error by a factor $\sqrt{6}$. In the sequential method this was not done. The reason is that still 1 stochastic source corresponds to the same computational effort as the sequential method if the time spent for contractions is neglected, because we do not need to fix the nucleon interpolating field nor the spin projector.

As a second step we consider $\langle x \rangle_{u-d}$. As before, we carried out the analysis using the stochastic method. Note that this required only a set of new contractions, since the propagators from the g_A analysis described above were available. In Fig. 6.3 we show the relative error as a function of the number of stochastic sources N_s for a fixed number of gauge field configurations $N_{\text{gauge}} = 200$.

We used the correlators of proton and neutron in the analysis of the stochastic method, thus effectively boosting statistics by a factor of 2. We did not use different operators in order to estimate $\langle x \rangle_{u-d}$ because at zero momentum transfer $A_{20}(q^2)$ has no support from another operator than the twist-two operator $\mathcal{O}^{44}$, *cf.* Eq. (2.25). The points in Fig. 6.2 and Fig. 6.3 clearly show a convergence towards the error of the sequential method. In the case of $\langle x \rangle_{u-d}$, though, a convergence to the error of the sequential method is indicated, but in order to reach it, more stochastic sources are needed. We expect convergence for $N_S \sim \mathcal{O}(10)$.

We show the scaling of the signal-to-noise ratio (the relative error) as a function of the lattice volume $V = L^3$ for the three lattice extents $L/a = 16, 24, 32$ in Fig. 6.4. In the plot we also indicate the qualitative scaling of the sequential method. The results for $\langle x \rangle_{u-d}$ indicate that the scaling is at least not worse than the one of the sequential method. Note that the errors also have a systematic uncertainty, which however we do not analyze here. Thus, even though the

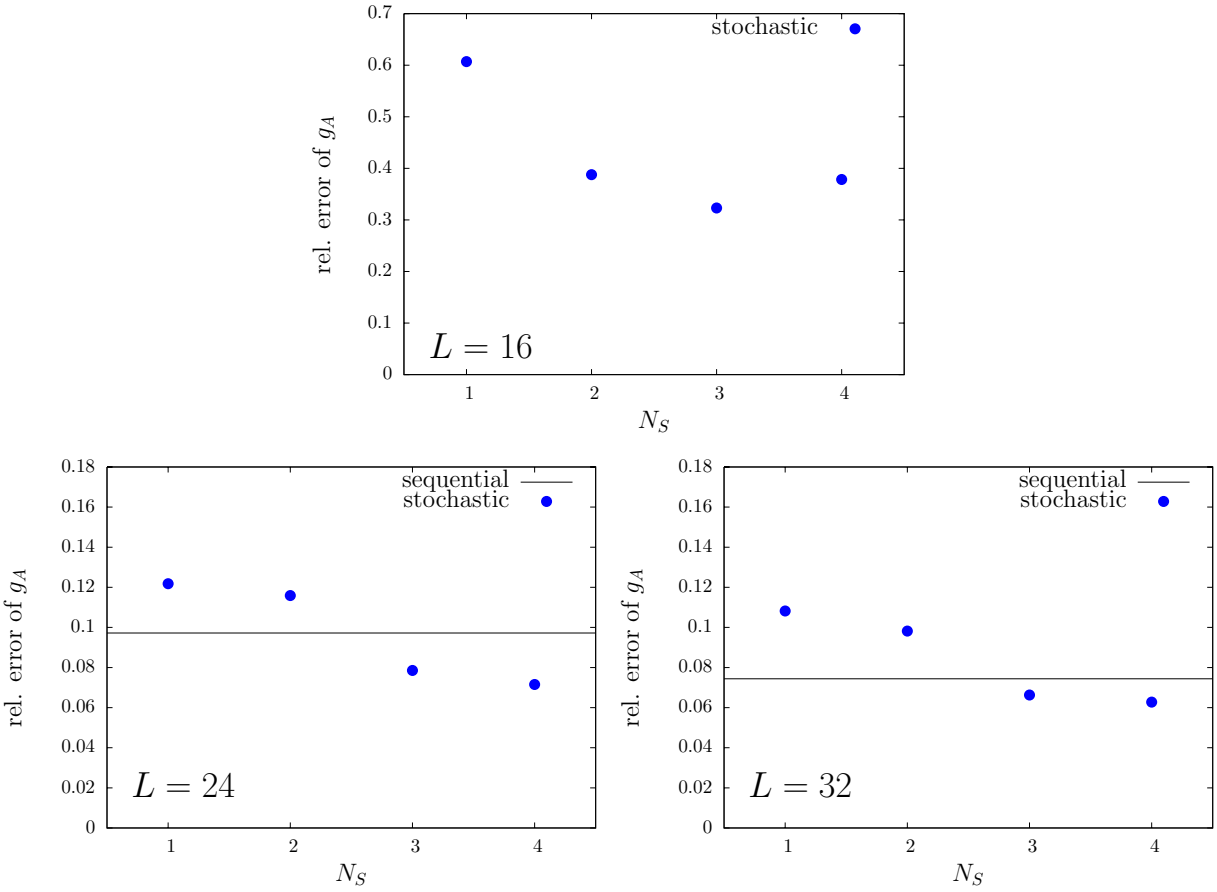

Figure 6.2: Relative error (gauge noise and stochastic noise) of the plateau value of g_A as a function of the number of stochastic sources N_s for three different volumes $V = L^3 \times T$ with $T = 2L$ and $L/a \in \{16, 24, 32\}$. The lattice spacing is $a \approx 0.08$ fm and the pion mass is about 300 MeV. For the volumes where the sequential method was applied as well, we show the error of the sequential method. In all cases the number of gauge field configurations is fixed to $N_{\text{gauge}} = 200$. Note the different scale on the vertical axis for the smallest lattice size, $L = 16$.

data for g_A is scattered more strongly around the dashed line, we expect the same scaling also in this case.

In conclusion one can say that with respect to the error the stochastic method is competitive with the standard method when one invests about $O(10)$ times the computational effort. Given the various advantages and the great versatility of the method explained in the previous section, one can say that this effort pays off when investigating matrix elements of other baryons or when using different interpolating fields for the nucleon.

Moreover, the gauge fields can be better exploited, which means that with a fixed number of stochastic noise vectors on a fixed number of gauge field configurations the gauge noise can

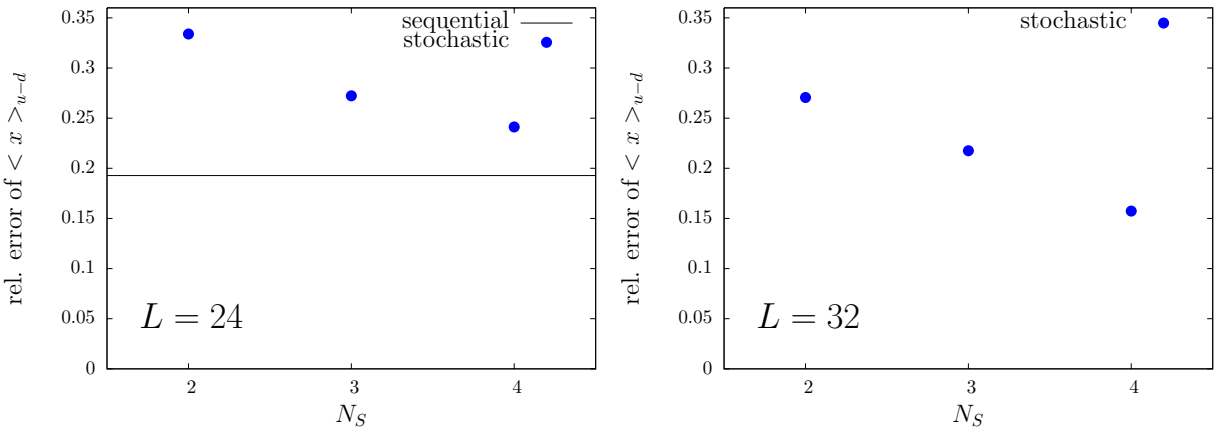

Figure 6.3: Relative error of the plateau values $< x >_{u-d}$ (gauge noise and stochastic noise) as a function of the number of stochastic sources N_s for two different volumes $V = L^3 \times T$ with $T = 2L$ and $L/a \in \{24, 32\}$. The lattice spacing is $a \approx 0.08$ fm and the pion mass is about 300 MeV. For the volume $L = 24$, where results using the sequential method with the same source-sink separation are available from a previous calculation, we show the error of the sequential method. In all cases the number of gauge field configurations is fixed to $N_{\text{gauge}} = 200$. We do not show results for the smallest lattice size available at the same value of the pion mass and lattice spacing, $L = 16$, and for $N_S = 1$, since we do not obtain reasonable plateaus when using only one stochastic source per gauge field configuration, and in the case $L = 16$ there are no reasonable plateaus for $N_S < 4$. With $N_S = 4$, the situation is better in the $L = 16$ case, such that we can obtain a plateau with a relative error of slightly above 50%.

be reduced, by adding additional forward propagators from different source positions on the same gauge field. We discuss this issue in the subsequent section.

6.3 Exploiting the versatility of the stochastic method

In this section we address a few benefits of the stochastic method and convince ourselves whether they work in practice.

First of all, we note that in the sequential method (see Sec. 5.7.1) the sequential source, Eq. (5.34), depends on the source position and therefore if the latter is varied, we need new inversions not only for the forward propagator but also for the backward propagator. In contrast, when we estimate the all-to-all propagator that appears in the expression (5.23) with a stochastic propagator that has support on the sink time slice, and we want to vary the source position while keeping the source-sink separation fixed, apart from the forward propagator computation no new inversions have to be done. In particular, if we have computed a number of stochastic propagators on a fixed number of gauge field configurations, we may compute additional forward propagators to be used in combination with the same set of stochastic propagators.

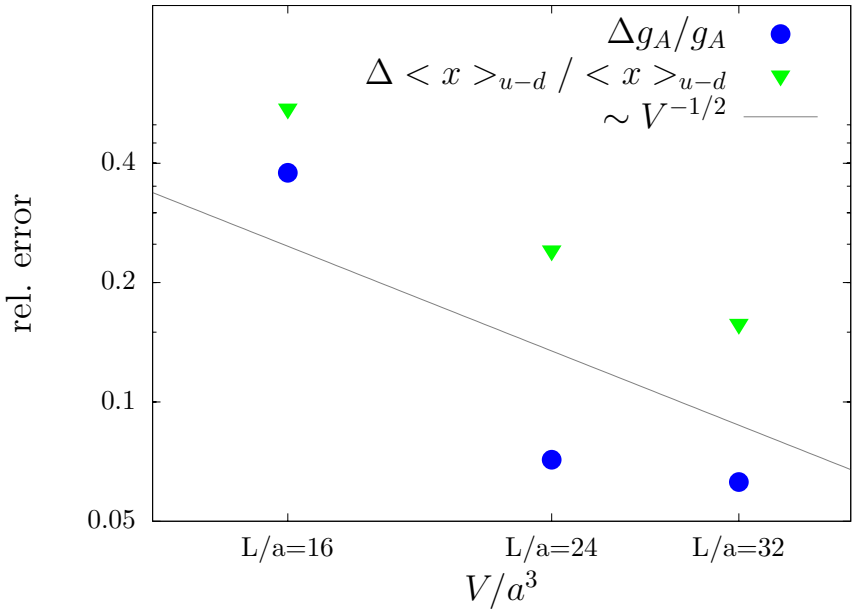

Figure 6.4: Volume scaling of the signal-to-noise ratio in the stochastic method. The blue circles show the relative error of the value obtained for g_A when using $N_S = 4$ stochastic sources per gauge field configuration and $N_{\text{gauge}} = 200$, *cf.* Fig. 6.2, where the same data points appear in different subplots. The green triangles show the relative error for $\langle x \rangle_{u-d}$ obtained in the same manner, *cf.* the data from the subplots of Fig. 6.3. Notice the logarithmic scale. The dashed gray line indicates the asymptotic volume scaling of the sequential method with fixed sink [71] and is meant to guide the eye.

As an example, in Fig. 6.5 we show the connected piece of the bare ratio of the scalar light quark content, see Eq. (8.18), obtained with a source-sink separation of $16a$ and a fixed number of spin-color diluted stochastic time slice sources $N_S = 3$, a number for which the gauge noise is already dominant compared to the stochastic noise, similar to the case of g_A discussed in the previous section. We use up to four point source positions per gauge field configuration and a fixed number of gauge field configurations $N_g = 495$. The first point source position is always chosen uniformly randomly and the subsequent positions are chosen such that they are sufficiently separated in space, in order to minimize correlations, but on the same time slice to be able to reuse the stochastic time slice propagators and still preserve the fixed source-sink separation. In table 6.1 we detail the spatial distances used in each direction. The lattice size is $L = 32$, $T = 64$, note that periodic boundary conditions apply in spatial directions.

The results shown in the figure, where the statistical error decreases about a factor of 2 when using 4 point source positions compared to a single point source position, demonstrate that it is indeed possible to effectively increase statistics, *i.e.* reduce the gauge noise, by adding more point source positions to be used in combination with the same number of stochastic sources, when the stochastic method is applied.

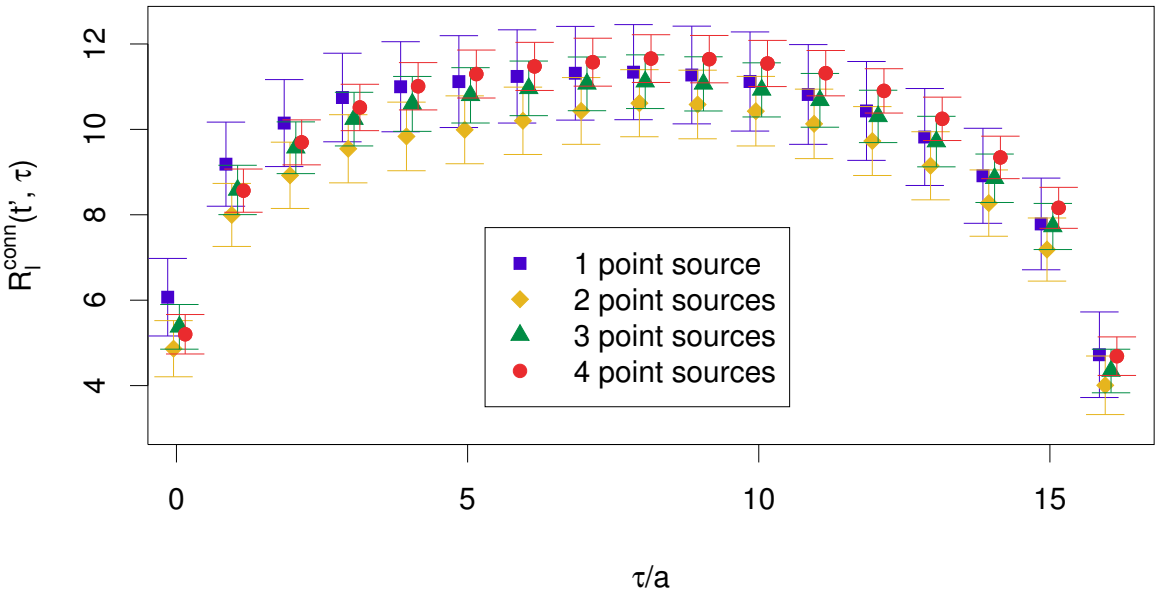

Figure 6.5: The connected piece of the bare ratio of the nucleon 3-point function with scalar operator $\bar{u}u + \bar{d}d$ and the nucleon 2-point function (R_l, see Eq. (8.18)) obtained employing the stochastic method using a fixed number of stochastic sources $N_S = 3$ and a fixed number of gauge field configurations $N_g = 495$. We show results obtained from using one to four point source positions per gauge field configuration. The pion mass is $m_\pi \approx 380$ MeV and the lattice spacing is $a \approx 0.078$fm and we have used a gauge field ensemble obtained from a simulation employing $N_f = 2 + 1 + 1$ twisted mass fermions at maximal twist.

position index	x	y	z
0	x_0	y_0	z_0
1	$x_0 + L/2$	$y_0 + L/2$	$z_0 + L/2$
2	$x_0 + L/2$	$y_0 + L/4$	z_0
3	x_0	$y_0 + L/4$	$z_0 + L/2$

Table 6.1: Scheme for choosing point source positions. x_0, y_0 and z_0 are chosen from a uniform distribution of the interval of integers $[0, L-1]$ and periodic boundary conditions apply.

In the previous section we have already mentioned one particularly noteworthy gain of the stochastic method. In comparison with the sequential method with fixed sink, where we have to fix the hadron (interpolating field), the choice of a different interpolating field does not require new inversions, provided that the definition of the quark fields, *i.e.* in most applications the smearing parameters used to extend the quark field and to increase the ground state overlap of the interpolating field, remain the same. Let us note at this point that the change of the smearing parameters would not require new computations of stochastic propagators, since one only needs to smear the stochastic source and still use the propagator of a local source, but this is just a technical side note. The freedom of choosing the hadron interpolating field at the level

of the contractions has an immediate consequence for nucleon matrix elements, namely we can use the correlation functions of the proton and the neutron. Because we are working with twisted mass fermions this is just an isospin breaking effect that enters the $\mathcal{O}(a^2)$ corrections, and we have not found a hint of large lattice artifacts when comparing the proton and neutron correlation functions. Thus, twice the statistics can be essentially obtained "for free". However, one should be cautious with this statement since the number of individual contractions can be large, when *e.g.* many different lattice momenta or many different operators are used. In this case the computational effort of the contractions may not be small compared to the one of the inversions. In addition – in order to exploit the versatility of the method – one may want to do the contractions using as many hadrons as possible. Therefore, contractions can actually be more costly concerning computational effort than the computation of the quark propagators.

There are more advantages that can be exploited, such as the combination of different momenta at the sink ($\vec{p}'$) and at the operator insertion ($\vec{p}$) that yield the same $\vec{q} = \vec{p}' - \vec{p}$, in order to increase statistics and improve the signal for observables at non-zero momenta. This is due to the fact that in contrast to the fixed sink momentum in the sequential method with fixed sink we can freely choose the sink momentum at the contraction level.
Thus we believe that the stochastic method is very promising and has the potential to reduce significantly the computational cost for calculating hadronic matrix elements.

7 Moments of Parton Distribution Functions

In this chapter we present results from lattice QCD computations of moments of parton distribution functions. The calculations performed here are motivated by the situation at the beginning of this thesis work in 2009, which is outlined in Sec. 7.1. Particular focus is on the understanding, treatment and elimination of systematic effects, with which we deal in the remaining sections. Most effort is spent on excited state effects arising from finite euclidean time separations in the correlation functions from which observables are obtained, see Sec. 3.4.

7.1 Situation at the Beginning of this Thesis

The situation at the beginning of this thesis work in 2009 was the following: Lattice QCD calculations of various quantities related to nucleon structure were available, among which moments of PDFs and various form factors. Despite the huge variety of results even for simple moments like g_A or $< x >_{u-d}$ there was a tension between experimental results and the numbers from lattice calculations of many different collaborations. Concerning the nucleon axial charge g_A, for instance, the experimentally measured value differs roughly 5 to 10% from the lattice results. To illustrate the situation, we show some of lattice results for g_A obtained from a range of pion masses and different lattice spacings using $N_f = 2$ twisted mass fermions at maximal twist in Fig. 7.1. The experimental value is also shown in this plot.

The experimental value from the Particle Data Group [11] has an uncertainty of order one per mill. The statistical accuracy of the lattice calculations is at the few per cent level. The values obtained from lattice calculations typically differ by about 10% from the experimentally measured one. In addition, there is a very mild dependence of g_A on the pion mass.

The tension is even more drastic for the first non-trivial moment of the unpolarized parton distribution in isovector flavor combination, $< x >_{u-d}$. See Fig. 7.2, where we compare the lattice data of the ETM collaboration with results obtained from global analyses of experimental data. There is a spread in the lattice data between the different groups which is larger than the typical error. Note, however that only the statistical error is shown. Systematic uncertainties are discussed later. The numbers from phenomenology account for a theoretical error (arising from the fit of the PDFs to experimental data as well as the uncertainty of the experimental data itself. The relative deviation between the results obtained by the various groups performing the global analysis of deep inelastic scattering data is less than 10%. It should be seen as a systematic error originating from the parametrization of the fits and the selection of the data to be fitted. The data from lattice calculations are typically of order 40 to 60% higher than the phenomenological results and show practically no or only very mild dependence on the pion

mass.

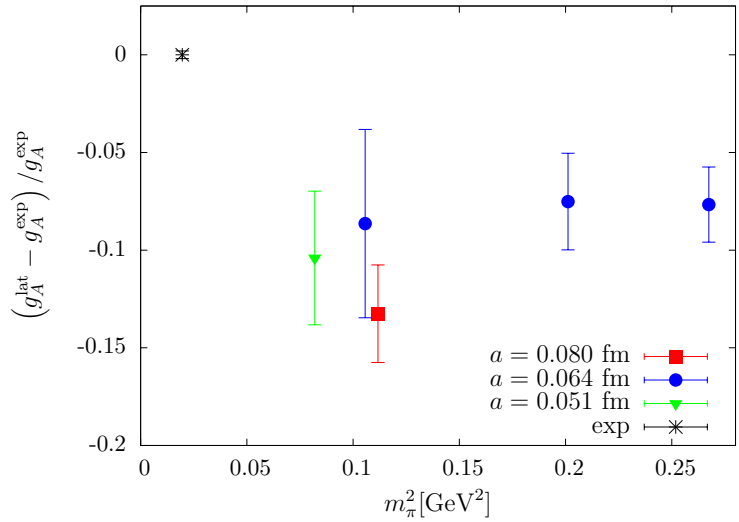

Figure 7.1: The filled symbols show the relative deviation of lattice computations of g_A using $N_f = 2$ maximally twisted mass fermions at three different lattice spacings for a range of pion masses [70] from the world average of the experimental results [11]. This experimental result corresponds to the black star.

Given this situation a calculation of quantities that have not been computed before are even more complicated than $< x >_{u-d}$ or g_A or continuing an even broader nucleon structure physics program did not seem prudent before understanding better the simpler quantities. Thus, we considered a careful analysis of systematic effects entering in the calculation of the nucleon matrix elements related to the simple quantities mentioned before indispensable.

7.2 Systematic Effects

The tension between results for observables related to nucleon structure obtained from analyses of experimental data and lattice calculations leads to the conclusion that either a conceptual mismatch in the different ways of determination exists, or the lattice calculations must be subject to systematic effects of the order of or greater than the statistical errors.
We would like to emphasize that different systematic effects can come with different signs, and they depend on the parameters of the simulation, such as the lattice spacing and volume or the pion mass. Therefore, it is mandatory to control the influence of all possible systematic effects, in order to have a credible result.
We start with a discussion of the systematic effects mentioned in Chapter 4.

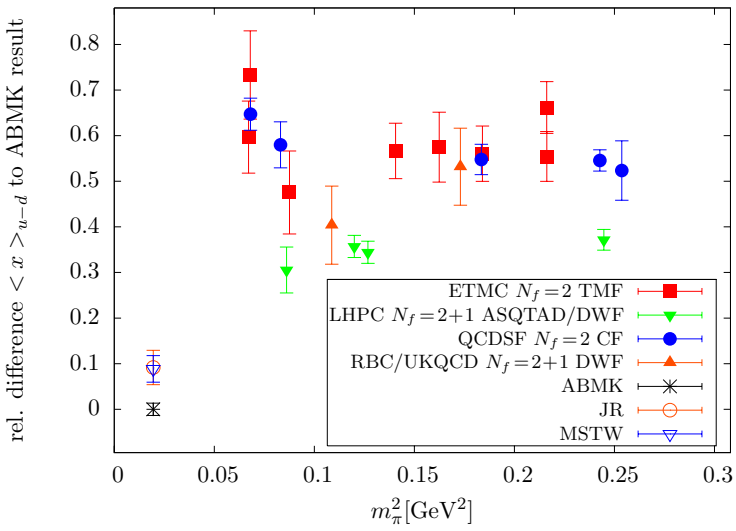

Figure 7.2: The filled symbols show the relative deviation of the values of $\langle x \rangle_{u-d}$, *i.e.* $|\langle x \rangle_{u-d} - < x >_{u-d}^{(\mathrm{ABMK})} | / < x >_{u-d}^{(\mathrm{ABMK})}$ obtained from various lattice calculations compared to the result from the ABMK analysis [7]. The open symbols show the relative deviation of the phenomenological results (JR) [9] and (MSTW) [72] as compared to ABMK [7]. In the lattice calculations, different lattice actions have been employed: twisted mass fermions (TMF) [73], a hybrid action of domain wall fermions (DWF) on a staggered sea [60], Clover fermions [74, 75] and DWF [76]. In order to exclude strong finite volume effects, only the lattice results obtained from ensembles with $m_\pi L > 3.5$ are shown.

7.2.1 Lattice Discretization, Unphysical Quark Masses and Finite Volume

The most obvious systematic effect is lattice artifacts, *i.e.* discretization errors. As mentioned in Sec. 4.2, the lattice spacing provides a momentum cut-off and thereby a regularization which has to be removed in order to obtain physical results. This means in practice that every quantity has to be calculated at several lattice spacings. Provided those are sufficiently small, one can safely extrapolate to the continuum limit, however in the way explained in Sec. 4.2. This is most commonly done by performing a linear fit to the data as a function of the lattice spacing. In this case the slope of the line is then a measure of the size of the corrections arising from discretization. Note that when $\mathcal{O}(a)$ effects are absent, which is true for the quantities discussed here, one takes the data as a function of a^2, more general as a function of a^n where n is the power of the expected leading correction.

Discretization effects depend strongly on the particular lattice action used. Therefore, in order to control the systematic effect of discretization errors, carrying out the continuum limit is crucial. It allows to compare results from calculations where different lattice actions are employed. Consistent results in the continuum limit will largely increase the trust of the various lattice calculations.

As an example, for a test of the continuum limit, we show $\langle x \rangle_{u-d}$ obtained from a lattice computation with $N_f = 2$ maximally twisted mass fermions [73] at three different lattice spacings as a function of the square of the lattice spacing (made dimensionless by dividing by the hadronic scale r_0) in Fig. 7.3 for a range of pion masses. The data points agree within statistical errors with the extrapolated limit. That is, the expected $\mathcal{O}(a)^2$ effects from the $N_f = 2$ Wilson twisted mass calculation at maximal twist are small and even compatible with zero, at least within the large statistical uncertainties for the quantities discussed here. Hence we consider finite lattice spacing effects not pivotal for the explanation of the tension between lattice calculation and experiment.

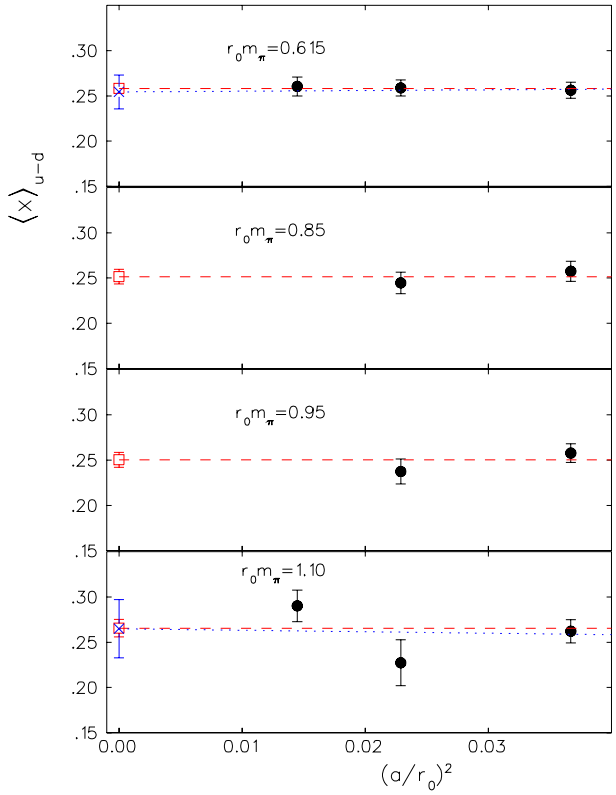

Figure 7.3: $\langle x \rangle_{u-d}$ obtained from $N_f = 2$ ensembles for a range of pion masses from 260 MeV $\lessapprox m_\pi \lessapprox$ 470 MeV at three different lattice spacings 0.05 fm $\lessapprox a \lessapprox$ 0.08 fm. Figure taken from Ref. [73].

As a second systematic effect we focus on finite volume effects. In the case of ETMC there exists a finite volume study of the quantities related to nucleon structure [70, 73] discussed here. In Fig. 7.4, we show g_A and $\langle x \rangle_{u-d}$ obtained from two different volumes at a pion mass of $m_\pi \approx 300$ MeV and a lattice spacing $a \approx 0.08$ fm. The physical lattice extents are $L = 1.9$ fm and $L = 2.6$ fm, corresponding to values $m_\pi L$ of 3.3 and 4.3, respectively. We observe that the calculations agree within statistical precision. This holds for other nucleon structure observables and results from other groups, see Refs. [70, 73] and references therein. Drawing a

brief conclusion, we consider finite volume effects to be sufficiently small and not contributing strongly to the tension between lattice QCD results and experiments, at least for pion masses as low as 300 MeV considered so far.

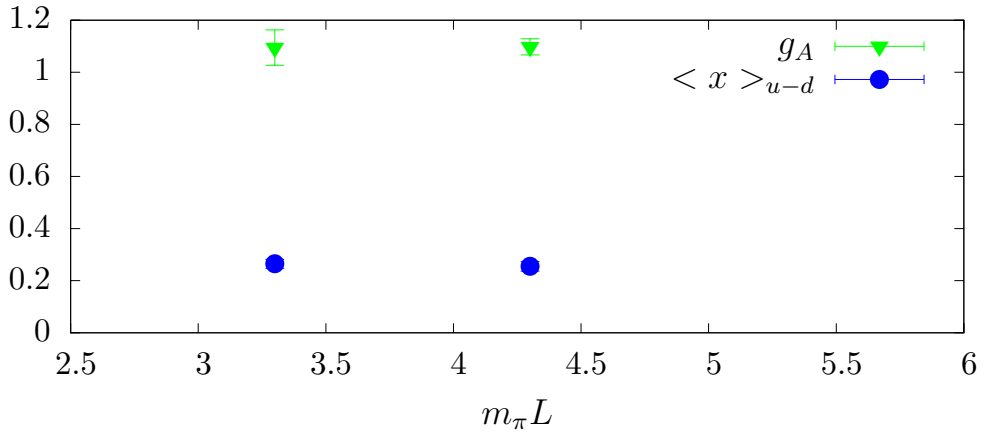

Figure 7.4: g_A and $\langle x \rangle_{u-d}$ obtained from $N_f = 2$ ensembles for two different volumes at a pion mass $m_\pi \approx 300$ MeV [70, 73].

When comparing the results of different lattice QCD collaborations (see also Fig. 7.2) one observes a smooth and basically flat dependence on m_π. Chiral perturbation theory however suggests a curvature towards the physical point [77]. Given the current data it remains an open issue whether a curvature will be seen at very low pion mass. It is therefore questionable whether χPT gives a good description of the data for the nucleon structure quantities discussed in this thesis.
Note that most recent results obtained at almost physical values of the pion mass [78] that appeared during the completion of this thesis confirm this picture, such that the tension remains. Computations at the physical point with a careful and comprehensive study of systematic effects are thus necessary in order to ultimately resolve the situation, which is becoming more and more puzzling.

7.2.2 Number of Dynamical Quark Flavors

Most of the current lattice calculations have been performed with $N_f = 2$ dynamical flavors. There are also $N_f = 2 + 1$ calculations employing a dynamical strange quark, see Fig. 7.2 and references in the caption. Given the good agreement between those calculations, the systematic effect of not taking into account the heavier quark degrees of freedom in the simulations is expected to be negligible or at least small. In addition, it seems unnatural that it depends on the particular lattice action used, in contrast to the lattice discretization effects. Nevertheless the effect of partial quenching for the observables related to nucleon structure has to be examined also for twisted mass fermions. Therefore, on behalf of the European Twisted Mass (ETM) collaboration, we performed an $N_f = 2 + 1 + 1$ calculation, employing dynamical up, down,

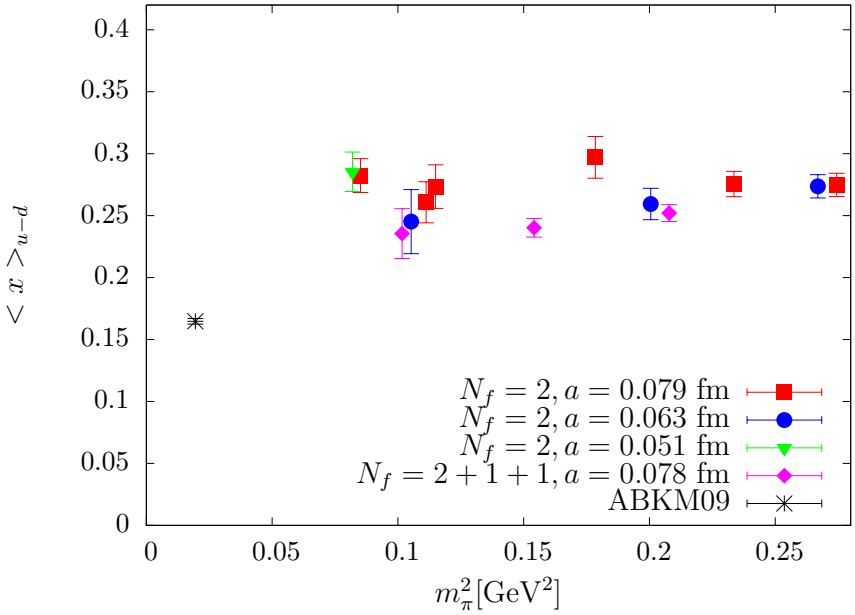

Figure 7.5: $\langle x \rangle_{u-d}$ obtained from $N_f = 2$ [73] and from $N_f = 2+1+1$ ensembles for a range of pion masses compared to the phenomenological value taken from the ABKM09 analysis [7].

strange and charm quarks, at a single lattice spacing. In Fig. 7.5 we show the results for $< x >_{u-d}$ and compare to previous $N_f = 2$ results. They agree within statistical precision, thus indicating that there is no strong effect stemming from ignoring the strange and charm quark in the simulations of dynamical fermions. To our best knowledge this is the first calculation of a nucleon matrix element in a four-flavor setup. The results presented above were first published in Ref. [79].

7.3 Ratios of Matrix Elements

A simple and convenient way to milden systematic effects is by building ratios of matrix elements, with the hope that some of the systematic effects cancel in the ratio. Moreover, if the quantities in the ratio are similar to each other, there might be a cancellation of gauge-dependent fluctuations and thus the gauge noise could be reduced compared to the individual quantities. It is particularly useful to this end to take ratios of observables renormalizing in the same way, *i.e.* having the same Z-factor, since then already the systematic effect of non-perturbative renormalization is canceled out automatically. This is for instance the case for the ratio $R_g = g_{A,oct}/g_A$, where $g_{A,oct} = \langle 1 \rangle_{\Delta u + \Delta d - 2\Delta s}$ and we recall $g_A = \langle 1 \rangle_{\Delta u - \Delta d}$ (*cf.* Sec. 2.2.1). The phenomenological value for R_g is 0.46(3) [80, 11], in the $\overline{\mathrm{MS}}$ scheme at a scale $\mu^2 = (2\ \mathrm{GeV})^2$. It can be shown for maximally twisted mass fermions that they have the same renormalization constant, *cf.* the discussion in the appendix of [62]. Thus the ratio is free of renormalization. However, the calculation of $g_{A,oct}$ requires disconnected diagrams that

are considered hard to evaluate numerically. Nevertheless, applying the twisted-mass specific noise reduction technique outlined in Sec. 5.7.2 renders the calculation more feasible. We discuss in detail now how this is done.

The relevant 3-point correlation functions for R_g are

$$C^{\Gamma_k}_{3,\mathcal{O}_{A,k,q}}(t',\tau) = \sum_{\vec{x}',\vec{y}} \mathrm{Tr}\,\left[\Gamma_k \left\langle N(\vec{x}',t')\mathcal{O}_{A,k,q}(\vec{y},\tau)\bar{N}(0)\right\rangle\right] \tag{7.1}$$

$$\mathcal{O}_{A,k}\,(y \equiv (\vec{y},\tau)) = \bar{q}(y)\gamma_5\gamma_k q(y), \quad \Gamma_k = \frac{i}{2}\,(1+\gamma_0)\,\gamma_5\gamma_k, \quad k = 1,2,3 \tag{7.2}$$

in the physical basis. For a graphical illustration see Fig. 3.4 and Fig. 3.3 concerning the connected piece and Fig. 3.2 concerning the disconnected piece of (7.1). Disconnected pieces are discussed in more detail in Chapter 8, therefore we want to keep the discussion short here.

When working in the mixed action setup (see Sec. 5.3), we can avoid mixing of the physical strange and charm quark and still preserve the automatic $\mathcal{O}(a)$ improvement that holds for twisted mass fermions at maximal twist. Moreover, by using the freedom of choosing the Wilson parameter in the Osterwalder-Seiler action for the strange quark in the valence sector, we can use the operators

$$\mathcal{O}_{A,k,\mathrm{iso}} = \mathcal{O}_{A,k,u} - \mathcal{O}_{A,k,d}, \tag{7.3}$$

$$\begin{aligned}\mathcal{O}_{A,k,\mathrm{oct}} &= \mathcal{O}_{A,k,u} + \mathcal{O}_{A,k,d} - 2\mathcal{O}_{A,k,s} \\ &= \left(\mathcal{O}^{\mathrm{tw}}_{A,k,u} - \mathcal{O}^{\mathrm{tw}}_{A,k,s_+}\right) + \left(\mathcal{O}^{\mathrm{tw}}_{A,k,d} - \mathcal{O}^{\mathrm{tw}}_{A,k,s_-}\right).\end{aligned} \tag{7.4}$$

Here, the label "iso" indicates the isospin vector flavor combination $u-d$. We would like to note that the operators appearing on the l.h.s. of the the above equation are the same physical basis, *i.e.* $\mathcal{O}^{\mathrm{tw}}_{A,k} = \mathcal{O}_{A,k}$, since we work at maximal twist. For completeness let us note that in terms of the correlation functions we use the definition

$$R_g(t',\tau) \quad = \quad \frac{\sum_k C^{\Gamma_k}_{3,\mathcal{O}_{A,k,\mathrm{oct}}}(t',\tau)}{\sum_k C^{\Gamma_k}_{3,\mathcal{O}_{A,k,\mathrm{iso}}}(t',\tau)}, \tag{7.5}$$

$$R_g(t',\tau) \quad \longrightarrow \quad R_g \quad \text{for} \quad t' \to \infty, \quad \tau \to \infty \quad \text{and} \quad (t'-\tau) \to \infty \tag{7.6}$$

where we have set the source point $(\vec{x},t) = 0$ for convenience. Eqs. (7.3) and (7.4) imply that we can use the noise reduction technique, since we need to evaluate differences between quark propagators of quarks that are related to different Wilson parameters in the action. Although this is not obvious to see from (7.4), it is possible to apply the variance reduction technique as described in App. 4.
The experimental value of R_g is 0.46(3) [80, 11].

We also compute the ratio $R_x = \langle x\rangle_{\mathrm{oct}}/\langle x\rangle_{u-d}$, where $\langle x\rangle_{\mathrm{oct}} = \langle x\rangle_{u+d-2s}$, in the right panel of

Fig. 7.7. For this quantity the relevant correlation functions are

$$C_{3,\mathcal{O}_{1\mathrm{D},q}}(t',\tau) = \sum_{\vec{x}',\vec{y}} \mathrm{Tr}\ \left[\Gamma \left\langle N(\vec{x}',t')\mathcal{O}_{1\mathrm{D},q}(\vec{y},\tau)\bar{N}(\vec{x},t)\right\rangle\right] \tag{7.7}$$

$$\mathcal{O}_{1\mathrm{D},q}\left(y \equiv (\vec{y},\tau)\right) = \bar{q}(y)\gamma_{\{\mu}D_{\mu\}}q(y), \quad \Gamma = \frac{1}{2}\left(1+\gamma_0\right) \tag{7.8}$$

where the definition of C is analogous to the one in Eq. (7.1), but with a different operator. The operator $\mathcal{O}_{1\mathrm{D}}$ is a twist-two operator, as in Eq. (2.25) the braces mean a symmetrization and subtraction of parts proportional to $g_{\mu\nu}$. Apart from the difference of having a derivative in the operator, the statements of the discussion made before about R_g concerning the cancellation of systematic effects essentially carry over to R_x, defined via

$$R_x(t',\tau) \quad = \quad \frac{C_{3,\mathcal{O}_{A,\mathcal{O}_{1\mathrm{D}},\mathrm{oct}}}(t',\tau)}{\left\langle C_{3,\mathcal{O}_{1\mathrm{D},\mathrm{iso}}}(t',\tau)\right\rangle}, \tag{7.9}$$

$$R_x(t',\tau) \quad \longrightarrow \quad R_x \quad \text{for} \quad t' \to \infty, \quad \tau \to \infty \quad \text{and} \quad (t'-\tau) \to \infty. \tag{7.10}$$

Here, the operators $\mathcal{O}_{1\mathrm{D,iso}}$ and $\mathcal{O}_{1\mathrm{D,oct}}$ are defined in complete analogy to Eqs. (7.3) and (7.4),

$$\mathcal{O}_{1\mathrm{D,iso}} = \mathcal{O}_{1\mathrm{D},u} - \mathcal{O}_{1\mathrm{D},d}, \tag{7.11}$$

$$\mathcal{O}_{1\mathrm{D,oct}} = \mathcal{O}_{1\mathrm{D},u} + \mathcal{O}_{1\mathrm{D},d} - 2\mathcal{O}_{1\mathrm{D},s}. \tag{7.12}$$

The value obtained from a phenomenological global analysis is $R_x = 2.89(9)$ [81].

We show the disconnected pieces which appear in the denominators of R_g and R_x, *i.e.* in $g_{A,\mathrm{oct}}$ and $\langle x\rangle_{\mathrm{oct}}$ in Fig. 7.6. They are compatible with zero due to a large relative error, see Fig. 7.6. Moreover, they seem to be small compared to the connected pieces of $g_{A,\mathrm{oct}}$ and $< x >_{\mathrm{oct}}$, which are of order 1.
For a complete and sound analysis, the disconnected pieces will be needed with a higher precision, however, since here we just want to present an explorative study, we omit them in the calculation of the ratios discussed here, because they are negligible would only increase the statistical error without changing the values significantly. In Fig. 7.7 we show the ratio $R_g(t',\tau)$ in the left panel and the ratio $R_x(t',\tau)$ in the right panel, as a function of the operator insertion time τ. In both cases we have fixed $t' = 16a$. the asymptotic values R_g and R_x are expected to be assumed in the middle between source and sink, *i.e.* around $\tau = t'/2 = 8a$, when a plateau is seen, see the discussion in 5.6. The experimental values are indicated by a dark gray band in the figure. The values obtained from the fits indicated with the light gray band are $R_g(m_\pi \approx 380\ \mathrm{MeV}) = 0.48(5)$ and $R_x(m_\pi \approx 380\ \mathrm{MeV}) = 2.46(24)$.

As can be seen from Fig. 7.7, the ratios are closer to the experimental values than g_A or $\langle x\rangle_{u-d}$ themselves. In the case of R_g the lattice calculation is even compatible within errors with the experimental result. For R_x the discrepancy is significantly decreased to about 15%, compared to $\langle x\rangle_{u-d}$, where it is roughly 50%, at value of the pion mass of $m_\pi \approx 380$ MeV used in the calculations described here.

Although this is a promising result, let us note that building ratios does actually not resolve

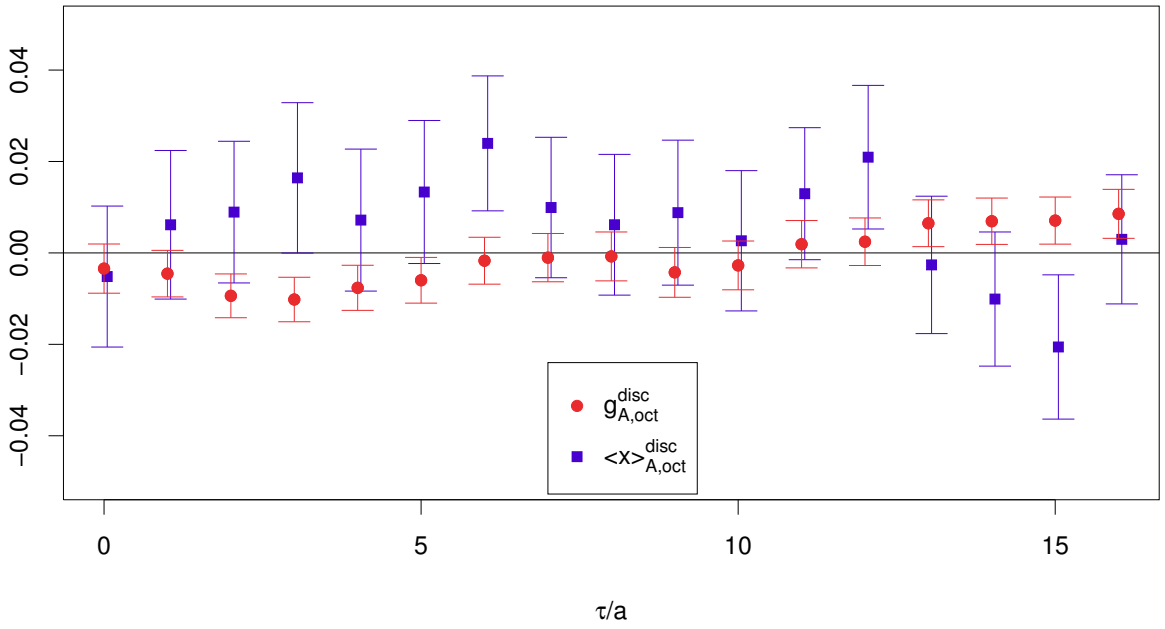

Figure 7.6: Disconnected contributions of $g_{A,\mathrm{oct}}$ (red circles) and $\langle x \rangle_{\mathrm{oct}}$ (blue squares), which appear in the ratio R_g and R_x, respectively, as a function of the operator insertion time slice, the source-sink separation was fixed to $16a$, with a lattice spacing of $a \approx 0.078$ fm. We use 2428 statistically independent measurements in the $N_f = 2+1+1$ twisted mass setup at maximal twist using a pion mass of $m_\pi \approx 380$ MeV.

which particular systematic effect is most responsible for the difference between experimental results for g_A and $\langle x \rangle_{u-d}$ and their counterparts from lattice QCD calculations. Moreover, it is unclear in which way the systematic effects cancel, since most effects are additive corrections. The ratios R_g and R_x therefore "conceal" the systematic effects somewhat. Nevertheless the compatibility of lattice and phenomenology results for the ratios suggests that indeed systematic uncertainties are responsible for the tension in g_A and $\langle x \rangle_{u-d}$ discussed above.
Note that a chiral extrapolation might be easier for the ratios, if systematic effects depending the pion mass cancel. In order to properly account for systematic effects, we need to know which effects are dominant and which are negligible, though.
Hence we consider a dedicated study of the effect that is very likely to explain at least part of the tension, namely excited state contributions, worthwhile and necessary. This is subject of the subsequent section.

7.4 Excited State Effects and Dedicated High Precision Analysis

One systematic effect on which an intense focus has been laid also by other lattice QCD collaborations, see *e.g.* [82, 83, 84], are from excited state effects. As outlined in Sec. 3.4, they arise

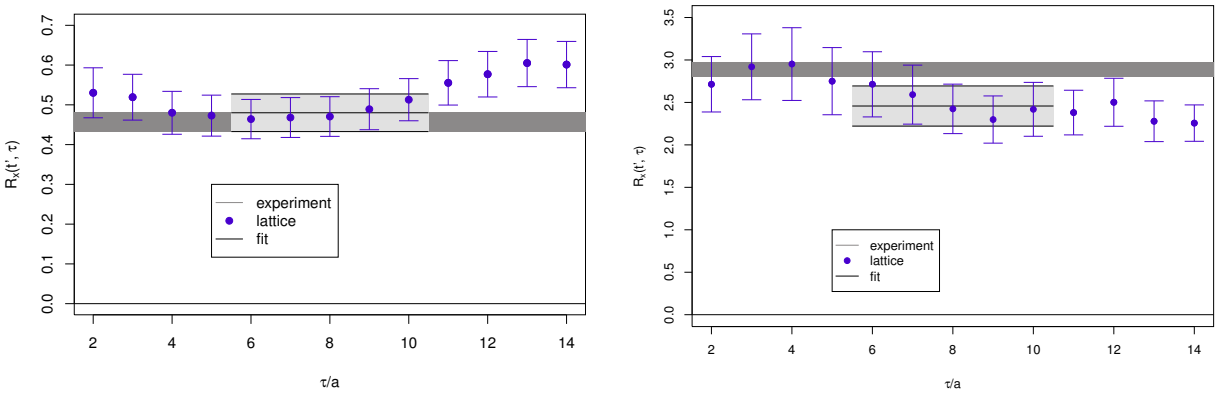

Figure 7.7: We show the ratios $R_g(t', \tau)$ (left) and $R_x(t', \tau)$ (right) as a function of the operator insertion time slice. The source-sink separation t' is fixed to $16a$. We use a lattice spacing of $a \approx 0.078$ fm in both cases, and 1911 statistically independent measurements in the $N_f = 2 + 1 + 1$ twisted mass setup at maximal twist with a pion mass of $m_\pi \approx 380$ MeV. The fits that yield the asymptotic values R_g and R_x are indicated by the light gray band and experimental results of R_g and R_x are shown with a dark gray band. In the computation of the ratios, only the connected pieces of the octet currents have been used, since the disconnected piece is small compared to the connected one and about compatible with zero within statistical precision, see Fig. 7.6.

from contributions of excited states in the spectral representation of the euclidean 2-point and 3-point correlation functions used to calculate nucleon matrix elements. Since excited states effects are physical they do not depend on the lattice action used and are thus expected to be universal. Hence our results, even though the analyses discussed here were done employing Wilson twisted mass fermions at maximal twist, are of relevance also for lattice QCD collaborations employing different lattice discretizations.

As a consequence of the situation explained before we decided to thoroughly look at excited state effects. Typically, in order to do so one would like to increase the source-sink separation in the usual fixed-sink method, which we outline in Sec. 5.7.1, and then compare the plateau values obtained from fits (see Sec. 5.6). This naturally requires an increased statistics for the larger source-sink separation, due to the exponential decrease of the signal-to-noise ratio of nucleon correlation functions, explained in Sec. 5.5.
However, since we would like to investigate the dependence of the matrix element, more precisely the matrix element plus contributions from excited states [*cf.* Eq. (3.24)], on the source-sink separation, we employed the open sink (or fixed current) method. This method is explained in Sec. 5.7.1 and requires the operator as well as the the insertion time slice to be fixed. Thus using the open sink method we can only hope to obtain the source-sink separation dependence for a small number of operators or observables. On the other hand we have the freedom to accumulate statistics, *i.e.* to evaluate the correlation functions on an increasing number of gauge fields (corresponding to statistically independent measurements), in order to have a precise result at a (possibly large) source-sink separation where excited state contributions are

negligible.

We consider it very useful for a first serious approach to determine the size of excited state contributions to have a precise result for only a few observables. Of course such a calculation needs a substantial amount of computational resources, since we aim to overcome an exponentially decreasing signal-to-noise ratio with high statistics. Consequently, we would like to do the analysis on a single gauge field ensemble only, that is at fixed values of the lattice spacing, quark mass and volume. It is therefore absolutely necessary to choose sound values for those parameters in order to have a meaningful result. If our findings indicate that there are substantial excited state contributions in the current calculations and that beating the exponentially decreasing signal-to-noise ratio with a huge statistics is not feasible we need to develop better techniques to resolve the excited state contributions at a more reasonable cost.

As a starting point we would like to look at excited state contributions in g_A. We decided to do the analysis at a value of the lattice spacing $a \approx 0.078$ fm, a pion mass m_π of about 380 MeV and a lattice volume $L^3 \times T$ with $L/a = 32$ and $T/a = 64$. For this choice of parameters, $m_\pi L \approx 5$, such that finite volume effects are sufficiently suppressed. The corresponding gauge field configurations were generated by the ETM collaboration using $N_f = 2 + 1 + 1$ twisted mass fermions at maximal twist [45]. The choice of the pion mass, $m_\pi \approx 380$ MeV guarantees that the computational cost for computing quark propagators, which increases when the pion mass is lowered, is feasible on the one hand and on the other hand it is not too high to have a meaningful result that is not too far from the physical situation.

First we need to establish a reference value for g_A. To this end we perform a fixed sink analysis of this observable, using a source-sink separation of 12 lattice spacings corresponding to about 0.94 fm in physical units. The correlation functions needed to evaluate g_A are given by the 3-point function Eq. (7.1) (in isovector combination) and by the nucleon 2-point function. We use only the 3-point correlation function with $k = 1$.
The result of such a calculation, with a number of gauge fields $N_g = 460$ is $g_A = 1.17(3)$ which differs by roughly 8% from the PDG value of 1.270(3) [11] and has a relative statistically error of about 2.5%. Of course the lattice result cannot be considered a physical one because a sound treatment of systematic effects is missing. In particular without a calculation at several values of the pion mass no chiral extrapolation is possible and accordingly we are subject to the systematic effect of having an unphysical pion mass. Looking at Fig. 7.5 we observe that in the $N_f = 2$ calculations the pion mass dependency is very mild and even compatible with being absent. Hence we can hope for this systematic effect to be small and in particular not to spoil the conclusions drawn from the dedicated excited state analysis presented in this section.

In the next step, we perform a free sink analysis of g_A. We decide to fix the operator insertion time $\tau = 9a$, *i.e.* we put the operator insertion nine time slices away from the location of the source (which we fix to zero for convenience in all expressions), aiming to have a result at a source-sink separation of $18a$ with the same statistical accuracy as obtained using the fixed sink method and a source-sink separation of $12a$. In this case the operator insertion is situated right in the middle between source and sink and the influence of excited states coming from the source is suppressed with the same exponential factor as the one coming from the sink, see Eq. (3.24) with $\tau = t'/2$ in the second and third term and the discussion in Sec. 3.4.

As a matter of fact, due to the aforementioned exponential suppression of the signal-to-noise ratio of nucleon correlation functions, we expect to require a substantial amount of statistically independent measurements, *i.e.* evaluation of the correlation functions on statistically independent gauge field configurations. We roughly estimate this number to be of order $5,000$ to $10,000$, which exceeds the number of configurations available[1], being of order $2,500$. Therefore we decide not only to extend the gauge field ensemble to about $5,000$ physically stored configurations, but also to use more than one point source position per configuration. In order to avoid correlations we choose the source positions on each gauge field configuration totally randomly from a uniform distribution. To equal the precision of the fixed sink analysis, in which we use 460 measurements, we have to collect 7500 statistically independent measurements of the correlation functions. Hence we use up to two randomly chosen point source positions per gauge field configuration. With this procedure we can guarantee that correlations are in fact negligible.

We show our result in Fig. 7.8 (left), where we compare the open sink analysis for a range of source-sink separations ranging from about 0.9 fm to 1.5 fm with the fixed sink analysis at a fixed source-sink separation of about 0.94 fm. We also show the experimental value in the plot. Clearly, within statistical uncertainty we do not see a difference which leaves us with the conclusion that excited state contributions are sufficiently suppressed when using a source-sink separation of 0.94 fm along with the values of lattice spacing, volume and pion mass listed above in the text.

We can make an even stronger statement. Even though the operator insertion is done at $\tau = t + 9a$, at a sink position $t' = t + 11$ we obtain a value for g_A that is compatible within errors with the value the fixed sink analysis yields. This means that in principle we could use a much smaller source-sink separation and still have a value in which excited state contributions are small compared to the statistical accuracy.

Nevertheless we would like to mention that it does not seem implausible that the 8% relative difference to the experimental value can be bridged by properly accounting for excited state effects and other systematic effects emerging at pion masses very close to the physical point. This will be subject of future investigations.

After the analysis of excited state effects for g_A we would like to address those effects in the observable $\langle x \rangle_{u-d}$ at the same values of lattice spacing, volume and pion mass as used before. Motivated by a study by another lattice QCD collaboration [85], we expect a sizable effect for this observable.

As in the case of g_A we establish a reference value from a fixed sink analysis with source-sink separation $12a$. We use $1,300$ measurements to obtain $\langle x \rangle_{u-d} = 0.250(6)$. Note that this value differs by more than 50% from the phenomenological value obtained in the ABKM analysis [7], $0.1627(22)$, which is much greater than the relative statistical precision of 2.4%.
Once the reference value is established for $\langle x \rangle_{u-d}$, we perform a free sink analysis of this quantity. In deviation from the free sink analysis of g_A we put the operator insertion $\tau = 11$ time

[1] The number of gauge field configurations from an ensemble generated by our collaboration which is physically stored on permanent storage media, typically hard disks or tape systems.

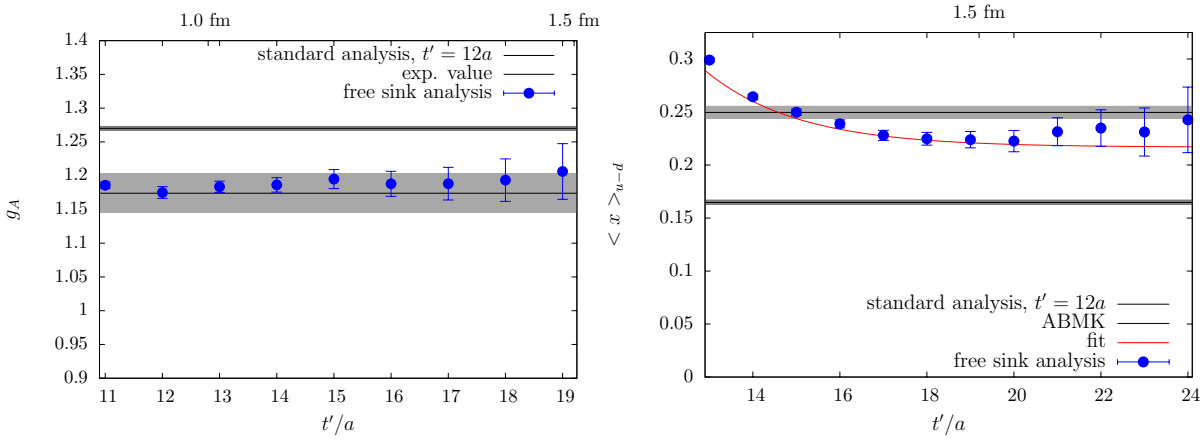

Figure 7.8: left: g_A as a function of the source-sink separation. The insertion time was fixed to $9a$. For comparison the value obtained from a fixed sink calculation with source-sink separation $12a$ is indicated by the light gray band. The experimental value Ref. [11] is shown by the dark gray band. **right:** $< x >_{u-d}$ as a function of the source-sink separation using a fixed insertion time of $11a$. The dark gray band shows a phenomenological result [7] and the value obtained from a fixed sink calculation with source-sink separation $12a$ is indicated by the light gray band. The red curve represents a fit of the asymptotic behavior, see Eq. (7.13).
The lattice calculations were performed on an $N_f = 2 + 1 + 1$ ensemble with a pion mass of about 380 MeV and a lattice spacing $a \approx 0.078$ fm

slices away from the source in order to safely suppress excited state effects originating from the source. Eventually, we want to have a precise result at a source-sink separation of $22a$, even though this would require estimated $50,000$ statistically independent measurements. In the end we perform only $23,000$ statistically independent measurements, for which we have to use up to 5 randomly chosen point source positions per gauge field configuration. We think that a further increase of statistics would not change the findings of the analysis.

The result of the free sink analysis is displayed in the right panel of Fig. 7.8, where we also indicate the value obtained from the fixed sink analysis and its error with a light gray band and the result from the global analysis of experimental data with a dark gray band. We observe that the data from the free sink analysis seems to assume a plateau value below the fixed sink analysis result. At a source-sink separation of $18a$ we reach about the same statistical accuracy as in the fixed sink analysis, where $1,300$ measurements are performed. However, it is not clear whether a plateau has been assumed at this value of the source-sink separation. For this reason we try to fit the exponential behavior [*cf.* Eq. (3.24)] to obtain an asymptotic value for infinitely large source-sink separation.

$$\langle x \rangle_{u-d}(t') = \langle x \rangle_{u-d}(\infty) + A \exp\left[\Delta M(t' - \tau)\right] \tag{7.13}$$

Here, A is an unknown constant depending on the details of the nucleon interpolating field and on the transition matrix element between first excited state and ground state of the nucleon.

Note that we ignore excited state contributions from the source, because they are supposed to be almost quadratically suppressed compared to those coming from the sink, see Sec. 3.4. We show a typical fit by the red curve in Fig. 7.8. Such a fit gives $\langle x \rangle_{u-d}(\infty) = 0.22(1)$. The error is estimated by varying the fit range and additionally by comparing the fits using a free parameter ΔM and the physical mass difference between the proton and the lowest-lying excited state, the $N(1440)$ resonance, which is about 500 MeV. Let us remark that the ΔM we obtain from a fit is roughly (1200 ± 400) MeV, which is greater than the physical value but considering the big error and the typically poor significance of this parameter in the fit, not to mention the fact that we use a pion mass heavier than the physical one, one cannot say that it is inconsistent with the physical mass difference.

The asymptotic value obtained for $\langle x \rangle_{u-d}$ in this way is 12% lower than the value obtained from the analysis using a fixed source-sink separation of $12a$, indicating that the excited state effects are indeed significant for this observable. Still, although accounting for excited states reduces the discrepancy with respect to the experimental result from about 50% to about 40% in our case, it does not resolve the puzzle. One may conjecture, though, that at lower pion masses the effect can increase significantly such that the remaining gap is bridged. However, this clearly needs to be demonstrated by calculations at almost physical pion masses as will be available for our collaboration in the future.

Let us emphasize again that compared to the fixed sink method, the open sink method is not practical when one has to compute a number of operators. The study presented here shows that the impact of excited states has always to be taken into account. Particular cautiousness is due when approaching the physical pion mass since excited states effects might even be stronger, which is for instance the case if the mass difference between the first excited depends on the pion mass, *i.e.* $\Delta M = \Delta M(m_\pi)$, and $\Delta M(m_\pi \approx 380 \text{ MeV}) > \Delta M(m_\pi \approx 140 \text{ MeV})$. We conclude with the note that the main aspects of this section are published in Refs. [86, 87].

7.5 The Generalized Eigenvalue Method as a Countermeasure to Excited State Contamination

In the previous section we have learned that in order to safely suppress excited state contributions an investment of one order of magnitude in terms of computing resources, compared to a standard fixed sink calculation where the source-sink separation is not large enough to safely suppress excited states, might be necessary. This is the case if the contributions are to be confronted by just using larger distances in euclidean time in the correlation functions of interest. It would be desirable, however, to face those effects in a more analytic way. A promising candidate for such an analytic method, which is capable of resolving the contributions from excited states, is given by the generalized eigenvalue (GEV) method. It was developed in Ref. [66] and recently employed and refined in Refs. [67, 68, 88]. Its main aspects are summarized in Sec. 5.7.3.

With the goal of reproducing a result similar to that of the high precision analysis of $\langle x \rangle_{u-d}$

described in the previous section we carry out a GEV analysis using a different number of smearing iterations for the APE and the Gaussian smearing to construct an operator basis with $N = 3$ operators. The statistics is 520 gauge field configurations and the largest number of smearing iterations corresponds to the standard analysis of the previous section. Note that the GEV analysis for a 3×3 problem takes at least 6 times the computational effort of a standard analysis, at worst 9 times, the details depending on the computing strategy and technical details. Assuming that the correlation matrix is symmetric, for instance, one only needs to calculate the upper or lower triangle thereof.

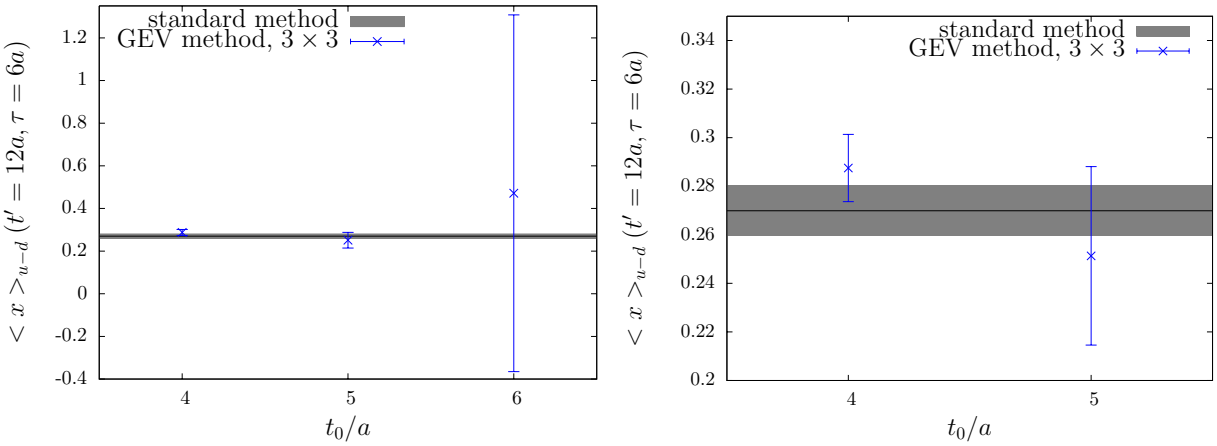

Figure 7.9: Comparison between the value obtained from a standard calculation of $\langle x \rangle_{\text{u-d}}$ using a fixed source-sink separation of $t' = 12a$ (gray band) and preliminary results from a GEV analysis (blue crosses). The plot on the right is a zoom of the plot on the left. We use the same source-sink separation as in the standard method in the GEV method and show results for values of the GEV parameter t_0 ranging from $4a$ to $6a$. The operator insertion time is $\tau = 6a$, corresponding to the time slice in the middle between source and sink. In both analyses the statistics is 520 gauge field configurations.

In Fig. 7.9 we compare the results from the GEV analysis described above using different values for the parameter t_0, which determines the size of the corrections due to finite N, see Sec. 5.7.3 and Ref. [67], to a value obtained from a standard calculation. The numbers obtained from the GEV analysis clearly agree with the one from the standard analysis, when using a source-sink separation of $12a$. This means that the excited state contribution cannot be resolved. There are several reasons for that. First of all, one has to note that with the operator basis used, the ground state contribution is dominant in all channels, the overlap with the first excited state is about one order of magnitude less.
Using a different operator that has a bigger overlap with the first excited state may improve the situation significantly. This has been tried by our group, but it turned out that the operators we used were very noisy, such that very high statistics is necessary in order to improve the statistical precision [89].

Therefore, as a precautious conclusion, it is unclear whether the generalized eigenvalue method

can resolve a contribution of excited states for matrix elements of the nucleon, when using a reasonable amount of computational effort.

It is worthwhile mentioning that there are several other methods like the plateau summation method which can also be used in combination with the GEV method [88] or the Generalized Pencil-of Function [90], as demonstrated in Ref. [91].

Yet one statement can be safely made. In order to determine the size of the excited state contribution or to safely suppress the latter in the correlation functions of interest, a price has to be paid in terms of computing resources. A credible calculation of nucleon matrix elements will need a significant investment of computational effort, and/or the development of new techniques to better resolve or suppress excited states.

8 The Scalar Quark Content of the Nucleon

While the problem concerning the moments of parton distribution functions discussed in the previous section has not been completely resolved, despite the very careful analysis of systematic effects we have performed, the situation is much clearer for another quantity related to the structure of the nucleon, namely the scalar quark content. In Sec. 2.3 we give an introduction to the subject. Here in this chapter, we concentrate on the technical details of the computation and the results.

When using a lattice discretization with an explicit breaking of chiral symmetry, mixing between the bare scalar strange and charm quark content occurs under renormalization, the reason being a flavor non-diagonal twist, see Eq. (5.11). Fortunately we can avoid mixing – up to $\mathcal{O}(a^2)$ effects – when using maximally twisted mass fermions in the mixed action setup, see Sec. 5.1 *ff* and in particular Sec. 5.3.
Using the $N_f = 2+1+1$ twisted mass formulation, employing dynamical up, down, strange and charm quarks, we are even capable of studying the charm quark content. Note that in principle it is possible to calculate the scalar strange and charm quark content without having a dynamical strange or charm quark in the sea quark action. However, this partial quenching would yield an uncontrolled systematic effect originating from neglecting s and c quark loops as vacuum fluctuations. Since the strange and charm quark contents of the nucleon are by definition very sensitive to the presence of dynamical strange and charm quark degrees of freedom, including those is mandatory when we want to obtain reliable results.

As pointed out in Sec. 3.3, nucleon matrix elements like the scalar quark content of the nucleon can be obtained from suitable ratios of 3-point and 2-point correlation functions of the nucleon. Here, for the case of the scalar quark content, the necessary correlation functions are the spin-projected version of the nucleon 2-point function Eq. (3.1) at zero momentum, which we rewrite here for convenience,

$$C_2^{\pm}(t') = \sum_{\vec{x}'} \mathrm{Tr}\left[\frac{1}{2}\left(1 \pm \gamma_0\right)\left\langle N(\vec{x}', t')\bar{N}(0)\right\rangle\right] \tag{8.1}$$

and the 3-point functions,

$$C_{3,f}^{\pm}(t', \tau) = \sum_{\vec{x}', \vec{y}} \mathrm{Tr}\left[\frac{1}{2}\left(1 \pm \gamma_0\right)\left\langle N(\vec{x}', t')\mathcal{O}_f(\vec{y}, \tau)\bar{N}(0)\right\rangle\right], \tag{8.2}$$

where we fix the source position to zero for better readability.

The scalar operators $\mathcal{O}_f$, $f = l, s, c$ used in the 3-point correlation functions are

$$\mathcal{O}_l = \bar{u}u + \bar{d}d, \quad \mathcal{O}_s = \bar{s}s, \quad \mathcal{O}_c = \bar{c}c. \tag{8.3}$$

In the twisted basis, we use the operators

$$\mathcal{O}_f^{\mathrm{tw}} = i\bar{\chi}_f \gamma_5 \tau^3 \chi_f, \quad f = l, s, c \tag{8.4}$$

$$\chi_l = (u, d), \quad \chi_s = (s_+, s_-), \quad \chi_c = (c_+, c_-), \tag{8.5}$$

where the fields with the subscripts $+$ and $-$ correspond to using different signs of the Wilson parameter in the Osterwalder-Seiler action, when using the mixed action setup, as explained in Sec. 5.3.
Using these operators we obtain multiplicatively renormalizable and $\mathcal{O}(a)$ improved matrix elements [62]. They correspond to the operators in physical basis in the following way

$$\mathcal{O}_f^{\mathrm{tw}} \Leftrightarrow \begin{cases} \mathcal{O}_l, & f = l \\ 2\mathcal{O}_s, & f = s \\ 2\mathcal{O}_c, & f = c. \end{cases} \tag{8.6}$$

Since those operators have a non-vanishing vacuum expectation value, which we however are not interested in when computing the scalar quark content of the nucleon, we define a vacuum-subtracted correlation function, where we subtract the vacuum expectation value,

$$C_{3,f}^{\pm,\mathrm{sub}}(t', \tau) = C_{3,f}^{\pm}(t', \tau) - C_2^{\pm}(t') \sum_{\vec{y}} \left\langle \mathcal{O}_f(\vec{y}, \tau) \right\rangle, \tag{8.7}$$

We also differentiate between connected and disconnected contributions of $C_{3,f}^{\pm,\mathrm{sub}}$, since in practice we use different techniques to calculate them.

$$C_{3,f}^{\pm,\mathrm{sub}} = \mathcal{C}_f^{\pm} + \mathcal{D}_f^{\pm}, \tag{8.8}$$

$$\mathcal{C}_f^{\pm} = \sum_{\vec{x}', \vec{y}} \mathrm{Tr} \left\{ \frac{1}{2} (1 \pm \gamma_0) \left\langle \left[N(\vec{x}', t') \mathcal{O}_f(\vec{y}, \tau) \bar{N}(0) \right]_{\mathrm{conn}} \right\rangle \right\} \tag{8.9}$$

$$\begin{aligned} \mathcal{D}_f^{\pm} = & \sum_{\vec{x}', \vec{y}} \mathrm{Tr} \left\{ \frac{1}{2} (1 \pm \gamma_0) \left\langle \left[N(\vec{x}', t') \bar{N}(0) \right]_{\mathrm{conn}} \left[\mathcal{O}_f(\vec{y}, \tau) \right]_{\mathrm{conn}} \right\rangle \right\} \\ & - \sum_{\vec{x}'} \mathrm{Tr} \left\{ \frac{1}{2} (1 \pm \gamma_0) \left\langle \left[N(\vec{x}', t') \bar{N}(0) \right]_{\mathrm{conn}} \right\rangle \right\} \sum_{\vec{y}} \left\langle \left[\mathcal{O}_f(\vec{y}, \tau) \right]_{\mathrm{conn}} \right\rangle \end{aligned} \tag{8.10}$$

Here, $[\cdots]_{\mathrm{conn}}$ denotes all connected Wick contractions of the fermionic fields, and as usual $\langle \cdots \rangle$ denotes the average over gauge field configurations. For the discussion of connected and disconnected 3-point correlation functions see also Sec. 3.5.
The correlation functions are connected by the symmetry (due to the anti-periodic boundary

conditions for fermionic fields in euclidean time, see *e.g.* [26]),

$$C_2^+(t') = -C_2^-(T-t'), \quad C_{3,f}^+(t',\tau) = -C_{3,f}^-(T-t',T-\tau), \tag{8.11}$$

which we exploit in order to effectively increase the number of measurements for the disconnected piece without additional computational effort. In the above expression T is the time extent of the lattice. We will drop the superscript $+$ and $-$ for the remainder of this chapter and always use the average of the 2-point and 3-point correlation functions on the left and right hand sides of (8.11). Moreover, we can average over proton and neutron correlation functions, because those only differ at $\mathcal{O}(a^2)$ due to the isospin symmetry breaking of the twisted mass action. In general there no are indications of large cut-off effects from isospin breaking for twisted mass fermions, with the so far only detected exception of the neutral pion mass [92, 93]. Also for the quantities considered here, we do not observe such an effect within statistical accuracy. Thus we can effectively gain a factor of 4 in statistics by exploiting the time symmetry, Eq. (8.11) *f*, and averaging over the correlation functions of the proton and the neutron.

In terms of quark propagators, the contraction $[\mathcal{O}_f(y)]_{\text{conn}}$ reads

$$[\mathcal{O}_l(y)]_{\text{conn}} = \text{Tr}\left[M_u^{-1}(y,y) + M_d^{-1}(y,y)\right], \tag{8.12}$$

$$[\mathcal{O}_s(y)]_{\text{conn}} = \text{Tr}\left[M_s^{-1}(y,y)\right], \tag{8.13}$$

$$[\mathcal{O}_c(y)]_{\text{conn}} = \text{Tr}\left[M_d^{-1}(y,y)\right], \tag{8.14}$$

where the trace acts in Dirac and color space and M is the Dirac matrix of the corresponding flavor, *i.e.* the quark propagator, see Sec. 5.4. Note that when working in twisted basis, those contractions look different

$$\left[\mathcal{O}_l^{\text{tw}}(y)\right]_{\text{conn}} = \text{Tr}\left\{i\gamma_5\left[M_u^{-1}(y,y) - M_d^{-1}(y,y)\right]\right\} \tag{8.15}$$

$$\left[\mathcal{O}_s^{\text{tw}}(y)\right]_{\text{conn}} = \text{Tr}\left\{i\gamma_5\left[M_{s_+}^{-1}(y,y) - M_{s_-}^{-1}(y,y)\right]\right\}, \tag{8.16}$$

$$\left[\mathcal{O}_c^{\text{tw}}(y)\right]_{\text{conn}} = \text{Tr}\left\{i\gamma_5\left[M_{c_+}^{-1}(y,y) - [M_{c_-}^{-1}(y,y)\right]\right\}, \tag{8.17}$$

where M now denotes the Dirac matrix in the twisted basis. The bare nucleon matrix element $\langle N|\mathcal{O}_f|N\rangle_{(\text{bare})}$ is then obtained as the asymptotic limit of the ratio (see the corresponding discussion in Sec. 3.3)

$$R_f(t',\tau) = \frac{C_{3,f}^{\text{sub}}(t',\tau)}{C_2(t')}, \tag{8.18}$$

$$R_f(t',\tau) \to \langle N|\mathcal{O}_f|N\rangle_{(\text{bare})} \quad \text{for} \quad t' \to \infty, \quad \tau \to \infty \quad \text{and} \quad (t'-\tau) \to \infty. \tag{8.19}$$

In order to obtain the renormalized matrix element, the bare one has to be multiplied by the renormalization factor of the scalar current, Z_s, which we can take *e.g.* from Ref. [36]. Note that when we work with twisted mass fermions, we usually compute the matrix element in

the twisted basis. In this case the renormalization factors of the bare matrix element is the inverse of the quark mass renormalization factor (see Ref. [35]), such that the quantity $\sigma = \langle N|m_u\bar{u}u + m_d\bar{d}d)|N\rangle$, which is related to the light quark content is free of renormalization. Note that in our lattice action, we have mass-degenerate light quarks, $m_u = m_d \equiv m_l$ Since also the y parameter, related to the strange quark content, is renormalization free, we will only use the bare matrix elements in the following.

For the light quark content disconnected and connected diagrams contribute whereas for the 3-point correlation functions that yield the strange and charm quark content connected contributions are absent. The connected contributions can be evaluated using standard techniques, either employing the sequential source method or a stochastic evaluation of an all-to-all propagator (see Sec. 5.7.1). Due to the form of the scalar operators in twisted basis, Eq. (8.4), and the form of the contractions Eq. (8.15), we can employ the powerful noise reduction method outlined in Sec. 5.7.2.

8.1 Light quark content and the pion-nucleon sigma term

The connected part of the light quark content can be computed with the method outlined in Sec. 2.3. Clearly, the more demanding computation is the disconnected piece. We would like to establish first of all a technical benchmark at the values of lattice spacing, volume and pion mass used in the previous chapter, employing the noise-reduction technique outlined in Sec. 5.7.2. In Fig. 8.1 we show the connected piece of the ratio R_l for a source-sink separation of $16a$ using 1980 statistically independent measurements and compare to a calculation at a source-sink separation of $12a$ using 520 measurements. The number of measurements was chosen such as to reach a statistical precision of less than 3% in both cases. For the disconnected piece, which is shown in Fig. 8.2, obtained with a statistics of 1911 measurements at a source sink separation of $12a$, we obtain a relative statistical error of 20%.

We note that the disconnected piece is almost negligible compared to the connected piece (note the scale of the vertical axes). Although it is plausible that the same situation occurs at smaller pion masses, we cannot be sure that this is still the case when a computation at the physical pion mass is done.
With the pion mass used here, $m_\pi \approx 380$ MeV, and using a source-sink separation of $12a$ to keep the statistical errors small in the disconnected piece, we obtain a value

$$\langle N|\bar{u}u + \bar{d}d|N\rangle_{\text{(bare)}} = 11.0(6). \tag{8.20}$$

The pion-nucleon sigma term, $\sigma_{\pi N} = \langle N|m_l(\bar{u}u + \bar{d}d)|N\rangle$, obtained with this result is

$$\sigma_{\pi N}\Big|_{m_\pi \approx 380\ \text{MeV}} = 153(8)\ \text{MeV}. \tag{8.21}$$

This is rather large compared to the phenomenological results already mentioned in Sec. 2.3 $\sigma_{\pi N} = 79(7)$ MeV [19] or $\sigma_{\pi N} = 59(7)$ MeV [20], but note that we neither perform an extrapo-

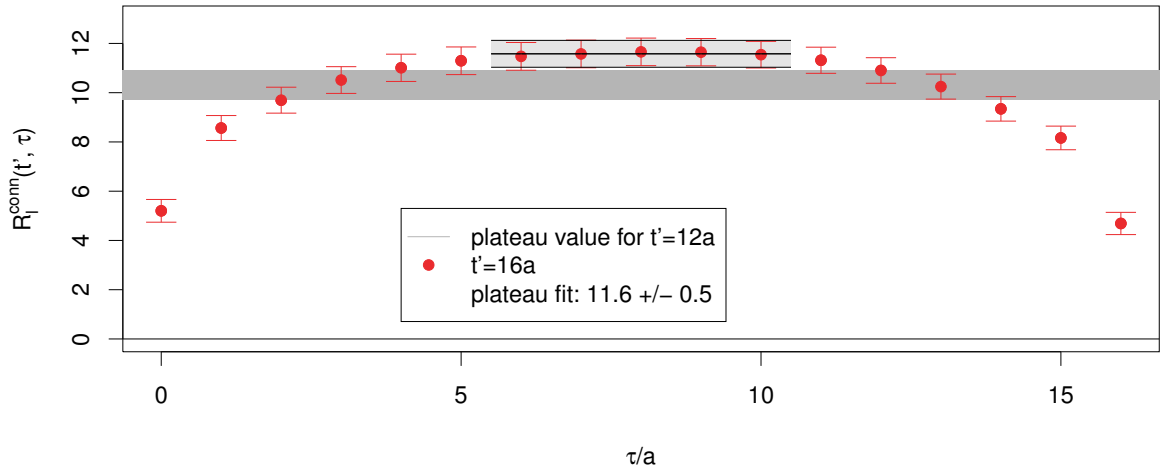

Figure 8.1: Connected piece of the bare matrix element $\langle N|\bar{u}u + \bar{d}d|N\rangle_{(\text{bare})}$. The source-sink separation was fixed to $16a$, with a lattice spacing of $a \approx 0.078$ fm. We use a pion mass of $m_\pi \approx 380$ MeV in the $N_f = 2+1+1$ twisted mass setup at maximal twist. 1980 statistically independent measurements are made for the estimate. We also compare to a calculation at a source-sink separation of $12a$ using 520 independent measurements

lation to the physical pion mass here, nor a continuum limit.
Preliminary results [94] indicate that the $\sigma_{\pi N}$ decreases with decreasing pion mass and lattice discretization errors are not seen within statistical accuracy.

Of course the plateau in the disconnected piece of the ratio R_l is rather short, assuming that we have reached a plateau at all. This already raises the suspicion that the source-sink separation was chosen too small to sufficiently suppress contributions from excited states. We would like to emphasize, though, that the source-sink separation of 12 lattice spacings was chosen to test whether the calculation of the light quark content including also disconnected diagrams is feasible at all. Having demonstrated that this is indeed the case, we now want to check for excited state effects.

In Fig. 8.1 we show the connected piece of the bare ratio R_l for a somewhat larger source-sink separation of $16a$ and compare to the result obtained from the calculation with a source-sink separation of $12a$. The plateau extends over a relatively large range of insertion times, giving us confidence that excited state contribution are in fact negligible, at least within the statistical accuracy, when using this larger source-sink separation, even though the value differs by about 10% from the reference result.

Addressing excited state effects in the disconnected piece of the ratio R_l, $R_l^{(\text{disc})}$, is technically much easier in our setup compared to the connected one, since no new correlation functions need to be computed when increasing the source-sink separations. Due to the method we employ to compute the disconnected piece of the 3-point function Eq. (8.10), where we use stochastic volume sources to estimate the quark loops Eq. (8.15) *ff*, we obtain the disconnected 3-point function for all combinations of t' and τ with the corresponding statistical error of the

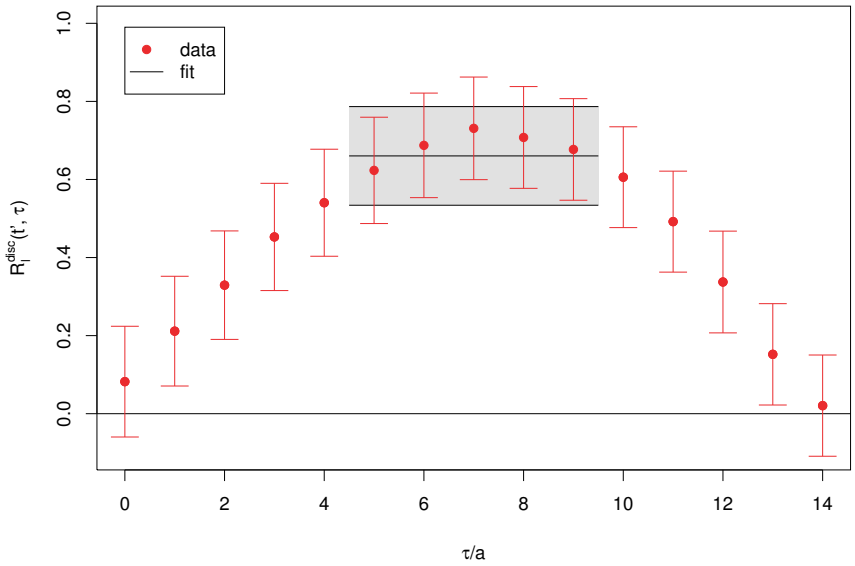

Figure 8.2: Disconnected piece of the bare matrix element $\langle N|\bar{u}u + \bar{d}d|N\rangle_{(\text{bare})}$. We fixed the source-sink separation to $12a$, with a lattice spacing of $a \approx 0.078$ fm. We use a pion mass of $m_\pi \approx 380$ MeV in the $N_f = 2+1+1$ twisted mass setup at maximal twist. We collected 1900 statistically independent measurements. Note that the disconnected piece is about one order of magnitude smaller than the connected one, see Fig. 8.1.

correlation functions. However, the gauge noise increases with the source-sink separation, such that in practice we are restricted by this statistical accuracy. We show $R_l^{(\text{disc})}$ for a number of source-sink separations in Fig. 8.3.

Compared to the source-sink separation $12a$ used initially, we observe that the plateau lies slightly higher when the source-sink separation is increased to $15a$, and the values of the plateaus do not seem to agree within errors. When using a source-sink separation of $18a$, corresponding to an increase of 50%, due to the large statistical uncertainty one can hardly identify a plateau, but the data seems to be even a bit higher.
This indicates that also for the disconnected piece of R_l there are sizable excited state contributions, which might be an even larger effect than for the connected piece. However, due to the absolute value of the disconnected piece compared to the connected piece, the impact on the total ratio R_l is moderate. Clearly, to make a statement about the size of the excited state contamination, a higher statistical precision is needed. With the current precision we can only state that excited state effects are non-negligible in the disconnected piece, which in turn however contributes very little to the total ratio.

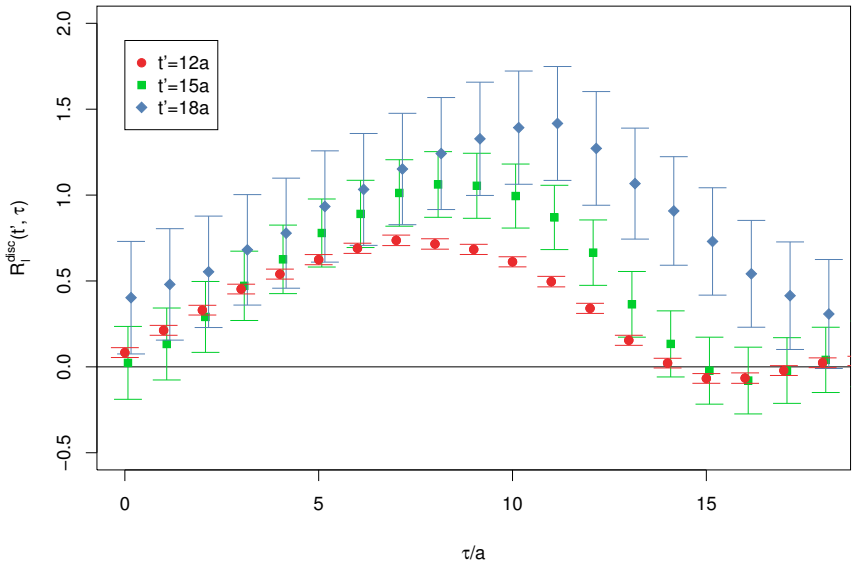

Figure 8.3: The disconnected piece $R_l^{(\mathrm{disc})}$ of the bare ratio R_l as a function of the operator insertion time, for 3 different source-sink separations, namely the source-sink separation $12a$ used before, and a 25% and 50% increased source-sink separation, $15a$ and $18a$, respectively. Other parameters are the same as before, see Fig. 8.2 and the text above.

8.2 Strange quark content and the y parameter

Using the nucleon interpolating field, Eq. (3.25), connected pieces are absent for quark contents of flavors other than the light ones, so in particular for the scalar s quark content. Hence, we only need to compute the disconnected piece of the corresponding 3-point function, $\mathcal{D}_s$, see Eq. (8.10). As mentioned before, a particular advantage when using the mixed action setup is avoiding mixing of the strange and the charm quark content and a solely multiplicative renormalization of the matrix element.
As in the case of the light quark content we perform a feasibility study at a source-sink separation of $12a$. Using 1900 statistically independent measurements we are able to obtain a value with a relative error of 14%. This accuracy is clearly significantly better than for other results published for this quantity, see *e.g.* [95, 96, 97].

Fitting a plateau to the data we obtain

$$\langle N|\bar{s}s|N\rangle_{(\mathrm{bare})} = 0.41(6), \tag{8.22}$$

which together with the matrix element of the light scalar current gives a y parameter

$$y = \frac{2\langle N|\left(\bar{s}s\right)|N\rangle}{\langle N|\left(\bar{u}u + \bar{d}d\right)|N\rangle} = 0.075(15). \tag{8.23}$$

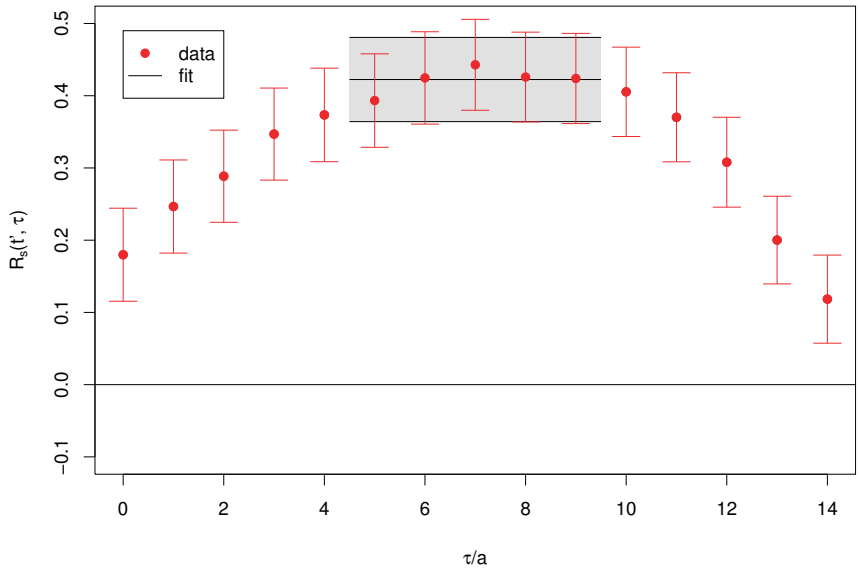

Figure 8.4: The bare ratio R_s as a function of the operator insertion time. The source-sink separation was fixed to $12a$, with a lattice spacing of $a \approx 0.078$ fm. We use a pion mass of $m_\pi \approx 380$ MeV in the $N_f = 2+1+1$ twisted mass setup at maximal twist. With a statistics of 1900 statistically independent measurements we obtain a relative precision of 14%.

Note that we do not give systematic errors here, because we would like to examine excited state effects first. To this end, we increase the statistics to 15141 measurements. This is only possible since, due to a heavier mass, the strange quark propagators needed for the 3-point correlation functions appearing in the ratio R_s are computationally significantly cheaper than the light quark propagators. In addition, the 2-point functions appearing in the numerator of the ratio were available from another calculation (to be more specific, the high precision computations performed in the scope of Sec. 7.4).
In Fig. 8.5 we show the ratio R_s for several source-sink separations. Compared to the source-sink separation $12a$, the data is systematically higher when using a larger source-sink separation. At a source-sink separation of $18a$ the plateau lies roughly 50% higher than the value obtained from a plateau fit with a source-sink separation of $12a$, and not compatible within statistical precision.

Our results thus indicate that excited state effects are sizable, however we cannot reliably determine their size, even with the large statistics used in the analysis. Assuming that a source-sink separation of $18a$ is sufficient to reach a plateau value for R_s where excited state contributions are small (compared to the statistical accuracy), the value of $\langle N|\bar{s}s|N\rangle$ would change by about 50%. If we then make the reasonable assumption that the value of the scalar light quark content $\langle N|\bar{u}u + \bar{d}d|N\rangle$ does not increase by more than of order 10% compared to the value quoted above, we can expect that accounting for excited state effects yields a value for the y parameter that is 25% higher than the value quoted above in (8.23). Thus the impact of excited states is of about the same order as the statistical uncertainty, which is about 20%. Of course in order

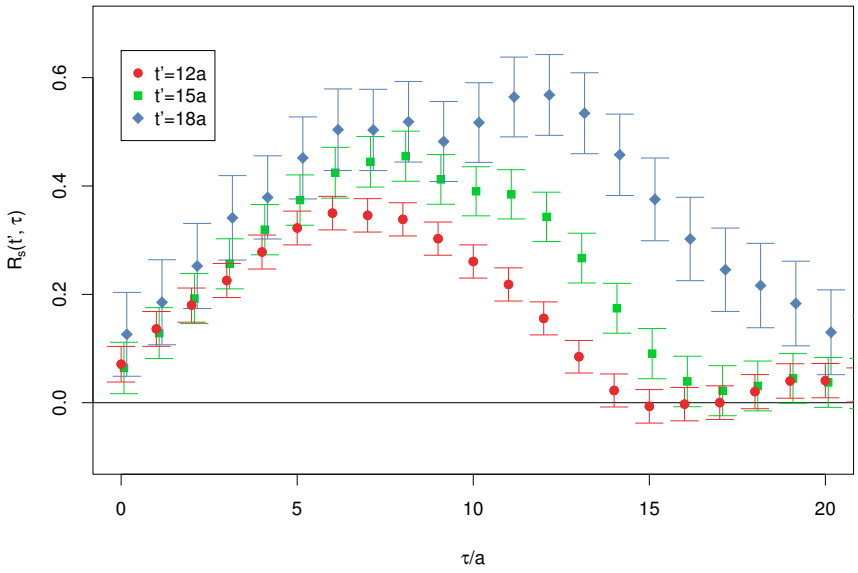

Figure 8.5: The bare ratio R_s as a function of the operator insertion time, for 3 different source-sink separations, namely the source-sink separation $12a$ used before, and a 25% and 50% increased source-sink separation. Other parameters are the same as before, see Fig. 8.4 and the text above.

to make a firm statement, the statistics has to be further increased. With the unclear situation here, we do not intend to perform a chiral extrapolation here. Preliminary results for the y parameter [94] indicate that the $\sigma_{\pi N}$ does not show a sign of discretization errors within statistical accuracy.

8.3 Charm quark content

With the mixed action setup used for the strange quark content we are also capable of studying the charm quark content. The only thing we need to do is to choose the matching mass for the sea charm quark mass. Note that this is the first lattice study of the scalar c quark content where a dynamical charm quark was used in the simulations.

In Fig. 8.6 we show the ratio R_c and compare to the ratio R_s obtained before. The statistical uncertainty is large and the data is compatible with zero within a 2σ range. That is why we do not attempt to perform a fit. However, R_c shows a tendency to be positive and smaller than R_s.

We thus conclude that the scalar charm content is at least not much greater than the scalar strange quark content.

$$\langle N|\bar{c}c|N\rangle \lesssim \langle N|\bar{s}s|N\rangle \tag{8.24}$$

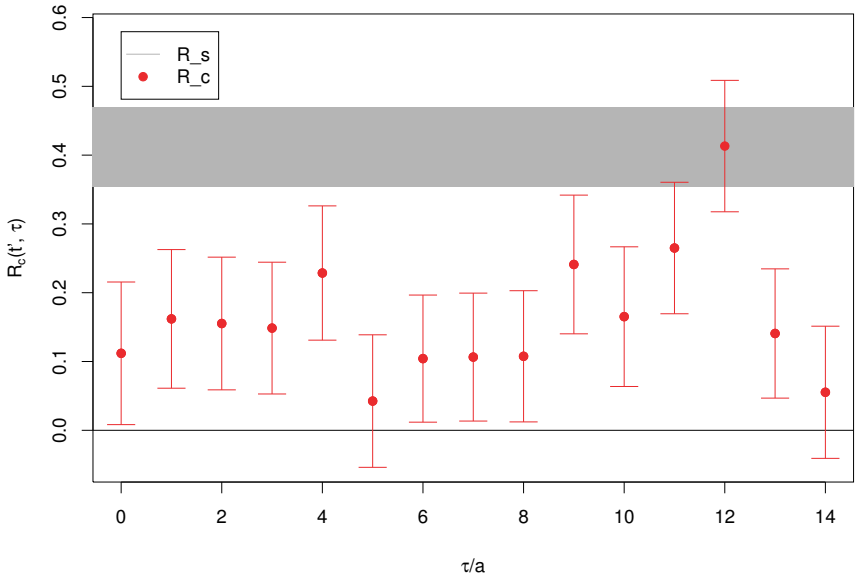

Figure 8.6: The bare ratio R_c as a function of the operator insertion time. The source-sink separation was fixed to $12a$. We use a pion mass of $m_\pi \approx 380$ MeV in the $N_f = 2+1+1$ twisted mass setup at maximal twist with a lattice spacing of $a \approx 0.078$ fm. Using a statistics of 1900 statistically independent measurements for the estimate of R_c. The ratio R_s related to the strange quark content is indicated by the gray band.

However we do not know whether excited state effects are large for the scalar c quark content and we cannot possibly resolve such an effect given the current data with poor accuracy. Therefore we have to perform a careful study of excited state contamination. Yet, the relation in Eq. (8.24) presumably holds nevertheless, since excited state effects are expected to be similar for both quantities.

8.4 Conclusion

We have performed a lattice QCD feasibility study of nucleon scalar matrix elements. Using a noise-reduction technique specific to twisted mass fermions, we obtain in a first computation values for the phenomenologically significant observables $\sigma_{\pi N}$, including the disconnected diagrams, with a relative error of 5% and the y parameter with a relative error of 20%. However, there are significant excited state effects as shown for the strange quark content using a huge statistics of 15141 independent measurements. We would like to mention that we have performed computations at different pion masses and lattice spacings, but at the time of the completion of this thesis the precision of those results is not as good as for the feasibility study presented here. Given this situation, where we have no good control over excited state effects, we do not attempt to perform an extrapolation to the physical point or a continuum limit. However, we have shown that using the twisted-mass specific noise-reduction technique, the cal-

culation of (disconnected pieces of) scalar matrix elements is in principle feasible, even though being very demanding. We have also tried to estimate the charm quark content, but due to a poor precision and possibly large excited state contamination we can only make the qualitative statement that it is not much larger than the strange quark content.

9 Summary

In this thesis we have presented lattice QCD calculations of observables related to nucleon structure with particular focus on understanding a discrepancy of lattice computations and global phenomenological determinations of these quantities as it existed at the beginning of this thesis. To this end, a comprehensive and detailed study of systematic effects has been carried out. All calculations have been performed employing $N_f = 2$ and $N_f = 2+1+1$ Wilson twisted mass fermions at maximal twist, a formulation of lattice QCD which possesses the advantage of automatic $\mathcal{O}(a)$ improvement for the quantities considered here.

A first and major part of this thesis is concerned with moments of parton distribution functions (PDFs). It is most important to understand nucleon structure from a first principles QCD calculation, since it is only possible to directly access this non-perturbative information through lattice computation. In addition, as stated in the introduction, there exists an unresolved puzzle concerning moments of PDFs. Namely, there is a difference between results obtained from analyses of experimental data and from lattice QCD calculations of such moments. For example, the tension between experimental results and lattice QCD computations is of order 10% for g_A (one of most easy to compute PDF moments), which is significantly larger than the quoted uncertainties. Concerning the first moment of the unpolarized parton distribution (in the isovector flavor combination) $\langle x \rangle_{u-d}$, which is also a rather easy to compute moment, the tension is even stronger, roughly of order 50%, while the quoted error is only about a few per cent.
Our goal was to clarify the situation by a careful analysis of systematic effects in the lattice computations.
In particular, the systematic effects investigated are lattice discretization errors, finite size effects, the number of dynamical quark flavors, unphysical pion mass, problems in the non-perturbative renormalization as well as excited state contamination.
From previous studies employing $N_f = 2$ Wilson twisted mass fermions at maximal twist [73, 70], we conclude that for the values of pion masses 270 MeV $\lessapprox m_\pi \lessapprox$ 480 MeV, lattice discretization errors are negligible, at least for the case of twisted mass fermions considered in this thesis, and hence do not explain the tension. Also, since calculations from different volumes agree within precision [73, 70], finite size effects cannot explain the tension on their own. Furthermore, we have compared computations where $N_f = 2$ [73, 70, 74], $N_f = 2+1$ [76, 60] and $N_f = 2+1+1$ dynamical flavors have been employed. Since we have found that the numbers agree within precision, we conclude that the influence of a dynamical strange and charm quark mass, in the range of the pion masses used in our analysis with $N_f = 2+1+1$ twisted mass fermions, 310 MeV $\lessapprox m_\pi \lessapprox$ 490 MeV, cannot be responsible for the tension. Therefore, from the list of possible systematic effects, non-perturbative renormalization and excited states are

left.
In order to address the influence of excited states we perform a dedicated high precision analysis of dependence on the the source-sink separation for our two benchmark observables g_A and $\langle x \rangle_{u-d}$. For the computation of the the necessary 3-point correlation functions we use a variant of the sequential method where the operator (corresponding to the observable of interest) has to be fixed, but the correlation functions are obtained for all source-sink separations. Since we need a high number of statistically independent measurements to be able to obtain data at relatively large source-sink separation with a good precision, we perform this computation only on one gauge field ensemble. We choose a gauge field ensemble with a pion mass $m_\pi \approx 380$ MeV a lattice spacing $a \approx 0.078$ fm and a lattice size $L \approx 2.5$ fm, corresponding to $m_\pi L \approx 5$.
For g_A we do not observe an excited state effect within statistical accuracy when comparing results from source-sink separations between 12 and 18 lattice spacings, corresponding to 0.94 fm and 1.4 fm. We have used about 7,500 statistically independent measurements to reduce the statistical errors at the source-sink separation $18a$ to about 2.5%. We can thus conclude that this systematic effect is negligible in current calculations of g_A at pion masses around the one used in this analysis. Hence the tension for g_A remains.
Concerning $\langle x \rangle_{u-d}$ we find excited state effects of the order of 10%, when comparing the result from a source-sink separation of $12a$ to the asymptotic value obtained by a fit to data from different source-sink separations up to $24a$. We have used about 23,000 measurements in this calculation to obtain a statistical precision of about 2.5% at a source-sink separation of $18a$. The observed excited state effect of 10% however does not explain the difference of 50% to results from phenomenology. Thus also for $\langle x \rangle_{u-d}$ the tension remains.
In conclusion, the tension between experimental and lattice determinations of the nucleon structure observables g_A and $\langle x \rangle_{u-d}$ remains. We remark that the number of measurements performed here is the highest statistics used for these quantities world-wide. Note that our statement concerning the excited state effects became only possible with this high statistics.
To test effects of non-perturbative renormalization, we have calculated renormalization free ratios of matrix elements, such as $R_g = g_{A,oct}/g_A$ and $R_x = \langle x \rangle_{u+d-2s}/\langle x \rangle_{u-d}$. We have used a twisted-mass discretization specific noise reduction technique in order to evaluate the disconnected contributions to the relevant 3-point functions for $g_{A,oct}$ and $\langle x \rangle_{u+d-2s}$.
We have found that at value of the pion mass of $m_\pi \approx 380$ MeV used in this study, the computed ratio R_g is compatible within errors with the experimental result. R_x differs by 15% from the phenomenological result, which is significantly milder than the difference for $\langle x \rangle_{u-d}$ at the same value of the pion mass, which is about 50%. This suggests that the tension between lattice computations and experimental determinations of g_A and $\langle x \rangle_{u-d}$ is due to systematic effects and not to a conceptual issue.
Note however that the ratios hide systematic effects such that we cannot tell from this study, which is the dominant one.
Ultimately, only a lattice computation at the physical pion mass where all systematic effects, in particular excited state contributions, are properly taken into account, can fully clarify whether the difference of the available lattice computations to results determined from analyses of experimental data is owed solely to systematic effects in present lattice calculations. This may require algorithmic improvements to render such a calculation feasible, since a very high pre-

cision is needed to resolve an excited state contamination. If the tension still remained, when all systematic effects are well-controlled, it would represent a really fundamental puzzle.

Of course, instead of using simply a high statistics it would be desirable to have a more economical method, such as a variational method. Therefore we tried generalized eigenvalue (GEV) method. Here, the goal was to obtain the same information as in the high precision analysis, but with less computational effort and using a more flexible method. We find that, when using an operator basis relying only on variations in the smearing of the quark fields, the first excited state of the nucleon cannot be sufficiently resolved to be able to reliably determine the contribution thereof. Using operators that couple better to the first excited state results in noisy correlation functions that require a high precision, though. It is therefore questionable whether the GEV method can help resolving excited state effects in nucleon structure calculations.

Another key target of this thesis is the computation of scalar quark-antiquark matrix elements of the nucleon, $\langle N|\bar{q}q|N\rangle$ with $q = u, d, s, c$. The main difficulty of such a calculation is the inclusion of quark-disconnected contributions. Here we could employ a noise-reduction technique specific to twisted mass fermions. With this technique we have obtained in a feasibility study using a pion mass of $m_\pi \approx 380$ MeV, a lattice spacing $a \approx 0.078$ fm and a lattice extent $L \approx 2.5$ fm a precise value for the pion-nucleon sigma term, $\sigma_{\pi N} = \langle N|\frac{1}{2}(m_u + m_d)(\bar{u}u + \bar{d}d)|N\rangle = 153(8)$ MeV. For the y parameter, $y = 2\langle N|\bar{s}s|N\rangle / \langle N|\bar{u}u + \bar{d}d|N\rangle$, we obtain a value $0.075(15)$. Note that we have achieved a (statistical) precision of 20%, which is significantly more precise than the results from other groups. Of course, a study of systematic effects for these quantities is still needed.
We have therefore addressed the effects of excited states in the scalar quark content. For the connected piece of the matrix element $\langle N|\bar{u}u + \bar{d}d|N\rangle$, we find that excited states are of order 10%, wheras for the disconnected piece we find indications for excited states effects, but with the precision obtained using 1900 statistically independent measurements, we cannot determine their size reliably. In the case of the scalar strange quark content, $\langle N|\bar{s}s|N\rangle$, we were able to increase the statistics significantly and with more than 15000 measurements, we observe that when using a source-sink separation of $18a$ the plateau value is roughly 50% higher than with a source-sink separation of $12a$. Due to the statistical uncertainty we cannot tell whether an asymptotic plateau value has been reached even with the source-sink separation $18a$, corresponding to about 1.4 fm. However, our results provide a clear warning that excited state effects may be sizable and need to be thoroughly investigated when computing the scalar quark content of the nucleon.
With a dynamical charm quark employed in the simulations, we can in principle also estimate the charm quark content. Due to a poor statistical precision however, and with the knowledge about possibly significant excited state effects for the strange quark content, we can only state $\langle N|\bar{c}c|N\rangle \lesssim \langle N|\bar{s}s|N\rangle$, which means that the scalar charm quark content is at least not much greater than the scalar strange quark content.
Given the influence of excited states and the high statistics needed in order to obtain a precise result, we do not attempt an extrapolation to the physical pion mass or a continuum limit, even though we have preliminary results at other pion masses and lattice spacings.

Nevertheless, we have demonstrated that scalar matrix elements of the nucleon can be determined in lattice QCD at good precision with reasonable cost, such that it will eventually become possible to perform the desired chiral extrapolation.

Apart from the calculation of physical quantities we also focus on a technical subject. The evaluation of the connected piece of nucleon 3-point correlation functions can be done using a so-called sequential, or generalized propagator, or with a stochastic estimate of an all-to-all quark propagator. The first method is typically applied in most computations of nucleon matrix elements, for the reason that the stochastic method can be computationally more expensive. However, a benefit of the stochastic method is its great versatility, since it does not require fixing the sink momentum and the spin projector, and in principle not the source-sink separation, either.
In order to clarify the additional cost quantitatively, we have carried out a feasibility study using gauge field ensembles with a pion mass $m_\pi \approx 300\,\mathrm{MeV}$ and a lattice spacing of $a \approx 0.080\,\mathrm{fm}$ and 3 different volumes $V = L^3 \times T$ with $T = 2L$ and $L = 16, 24, 32$. Using a fixed number of gauge field configurations $N_{\mathrm{gauge}} = 200$ and spin-color diluted time slice noise vectors, we have found found that for the quantity g_A about four times the computational effort must be spent compared to the sequential method to reach the same statistical accuracy. For $\langle x \rangle_{u-d}$ the number is larger, we have estimated it to be $\mathcal{O}(10)$.
Given the great flexibility of the stochastic method that does not require fixing the hadron nor the sink momentum nor the spin projector, we can easily compensate for this factor when computing multiple quantities that, say, require different spin projectors or matrix elements of other hadrons. We have also shown that the signal-to-noise ratio does not become worse compared to the sequential method when the volume is increased. Furthermore we have demonstrated how to reduce gauge noise and vary the source-sink separation, which should always be done to check for excited state contamination, with comparatively little computational effort.
We are establishing the stochastic method as the method of choice of our collaboration for our future hadronic matrix element calculations. Concluding, we can state that first-principles calculations of the nucleon structure in lattice QCD are possible and can to provide insight into the structure of the nucleon and thus help to understand the interaction of quarks and gluons at low energies analytically. In order to demonstrate that lattice QCD calculations can indeed yield reliable results, comparisons of "benchmark" observables between lattice QCD calculations and phenomenological determinations have to be made, which requires that all systematic effects in the lattice calculations are well-controlled. However, this is not an easy task, since in particular the elimination of excited state effects requires a high precision in the calculations and thus a significant amount of computing time. Algorithmic and technical improvement as well as the development of new methods can improve this situation, such that in the future the here discussed question about systematic effects as the cause of the discrepancy concerning moments of PDFs can be clarified. Moreover, also a precise lattice determination of the scalar quark content of the nucleon with controlled systematic errors will be available.

Appendix A

1 Light Cone Dominance

In this section we show that the dominant contibution to the integral in Eq. (2.12), which we rewrite here for convenience

$$W_{\mu\nu}(P,q) = \int d^4z\, e^{iq\cdot z} \langle P| \left[J^\mu(z), J^\nu(0)\right] |P\rangle\,, \tag{1}$$

for the DIS process at large Q^2 comes from the region where z^2 vanishes, *i.e.* from the light cone. To this end we choose the rest frame ot the target proton and the z-axis along the momentum transfer $\vec{q}$

$$P = (m, 0, 0, 0) \tag{2}$$

$$q = \left(\nu, 0, 0, \sqrt{\nu^2 + Q^2}\right) \tag{3}$$

Moreover, we choose light cone coordinates for convenience.

$$v = (v^+, v^-, v^1, v^2), \quad v_\pm = \frac{1}{\sqrt{2}}\left(v_0 \pm v_3\right) \tag{4}$$

$$v, w \quad \text{4-vectors} \quad \Rightarrow v\cdot w = v^+ w_- + v^- w_+ - v_1 w_1 - v_2 w_2 \tag{5}$$

In the Bjorken limit, *i.e.* $Q^2 \to \infty$ and x fixed, we have

$$q_3 \to \nu + mx. \tag{6}$$

We have used $Q^2 = 2m\nu x$ and the taylor expansion of the square root to obtain the above equation. Furthermore, in light cone coordinates and in the Bjorken limit, respectively, the momentum tranfer reads

$$q_+ = \frac{1}{\sqrt{2}}\left(2\nu + mx\right) \to \sqrt{2}\nu, \tag{7}$$

$$q_- = \frac{-mx}{\sqrt{2}}, \tag{8}$$

$$\Rightarrow q\cdot z = q^+ z_- + q^- z_+ \to \sqrt{2}\nu z_- - \frac{-mx}{\sqrt{2}} z_+, \tag{9}$$

such that the integral in $W_{\mu\nu}$ becomes

$$\int d^4z\, e^{iq\cdot z}\cdot \to \int dz_-\, e^{iq_+z_-} \int dz_+\, e^{iq_-z_+} \int dz_1 dz_2 \cdots . \tag{10}$$

If q^+z_- or q^-z_+ are large, the contribution of the integrand to the integral are suppressed by rapid oszillations. If we therefore impose the condition $|q^{\pm}z_{\mp}| \lesssim 1$, it follows

$$|z_+| \lesssim \frac{\sqrt{2}}{-mx} \quad \text{and} \quad |z_-| \lesssim \frac{1}{\sqrt{2}\nu}, \tag{11}$$

or equivalently

$$|z_0^2 - z_3^2| = |z|^2 \lesssim \frac{1}{Q^2}. \tag{12}$$

Due to causality the commutator in Eq. (1) must vanish for $z^2 < 0$. Therefore, in the Bjorken limit contributions with $z^2 \to 0$, *i.e.* the space-time region on and very close to the light cone dominate the hadronic tensor. Recall that in this limit the current product $J_\mu(z)J_\nu(0)$ is not well defined, but can be related to local operators by means of the operator product expansion, which is the subject of the subsequent section.

2 Light Cone Expansion

In the previous section we have learned that the dominant part of the integral in the hadronic tensor $W_{\mu\nu}$, Eq. (1), comes from the light cone region, where z^2 vanishes. We want to evaluate the time-ordered product of the hadronic currents, $\mathcal{T}[J_\mu(z)J_\nu(0)]$, appearing in Eq. (2.15). Generally, the product of two operators (to be understood as composite operators built from the fundamental quark and gluon fields), say $O_1(x)O_2(y)$ is not well-defined as $|x-y|^2 \to 0$. However by means of the operator product expansion (OPE) [98], it can be expressed as a sum of local operators $\mathcal{O}_i((x+y)/2)$ that are regular (in the sense that they can be renormalized in the standard way) and a set of complex coefficient functions $C_i(x-y)$ that may become singular as $x \to y$,

$$O_1(x)O_2(y) = \sum_i C_i(x-y)\mathcal{O}_i(\frac{x+y}{2}) \tag{13}$$

A simple dimensional counting suggests that the contributions dominant at large Q^2 are from the operators with the most singular coefficient functions. A more detailed discussion can be found in Refs. [99, 100].

Consider the Wick contraction of $\mathcal{T}[J_\mu(z)J_\nu(0)]$, where for simplicity we restrict to the current

of a single quark flavour with unit charge, that is $J_\mu = \bar{q}\gamma_\mu q$,

$$\begin{aligned}\mathcal{T}[J_\mu(z)J_\nu(0)] = \quad & \left(g_{\mu\nu} - 2\frac{z_\mu z_\nu}{z^2}\right)\frac{z^2}{\pi^4(z^2-i\varepsilon)^4} \\ & + \sigma_{\mu\lambda\nu\rho}\underbrace{:\bar{q}(z)\gamma^\rho q(0) - \bar{q}(0)\gamma^\rho q(z):}_{=:\mathcal{O}^\rho_V(z,0)}\frac{iz^\lambda}{2\pi^2(z^2-i\varepsilon)^2} \\ & + \epsilon_{\mu\lambda\nu\rho}\underbrace{:\bar{q}(z)\gamma^\rho\gamma_5 q(0) - \bar{q}(0)\gamma^\rho\gamma_5 q(z):}_{=:\mathcal{O}^\rho_A(z,0)}\frac{z^\lambda}{2\pi^2(z^2-i\varepsilon)^2} \\ & + \cdots . \end{aligned} \tag{14}$$

Here, we have used the sigma tensor $\sigma_{\mu\lambda\nu\rho} = g_{\mu\lambda}g_{\nu\rho} - g_{\mu\nu}g_{\lambda\rho} + g_{\mu\rho}g_{\nu\lambda}$, and the totally antisymmetric epsilon tensor with $\epsilon_{0123} = +1$. In addition, we dropped the normal-ordered product of 4 quark fields, which is of higher dimension as $\mathcal{O}^\rho_{A,V}(z,0)$ and is therefore less relevant in the OPE since it comes with a less singular coefficient function. The first term is a disconnected term independent of the target hadron. Hence, the most relevant contributions for the DIS process shown in Fig. 2.1 in the Bjoerken limit are those from the operators $\mathcal{O}^\rho_V(z,0)$ and $\mathcal{O}^\rho_A(z,0)$. They are "bi-local" which means that they involve the quark field at two different space-time points separated by a light-like distance.

Using the definition of the time ordered product, the hermiticity of the electromagnetic current and the identity

$$\frac{1}{(z^2-i\varepsilon)^2} = \frac{\mathcal{P}}{z^4} - i\pi\delta^1(z^2) \tag{15}$$

where $\mathcal{P}$ means principal value and δ^1 is the first derivative of the Dirac delta function, we obtain the expression

$$\begin{aligned} W_{\mu\nu} &= 2\,\mathrm{Im}\,T_{\mu\nu} \\ &= \frac{1}{2\pi}\int dz\, z^\lambda \varepsilon z_0 \delta^1(z^2)\,\langle N|\,\sigma_{\mu\lambda\nu\rho}\mathcal{O}^\rho_V(z,0) - i\epsilon_{\mu\lambda\nu\rho}\mathcal{O}^\rho_A(z,0)\,|N\rangle\,. \end{aligned} \tag{16}$$

In order to demonstrate how the OPE relates those bilocal operators to local ones, we outline the derivation here in a somewhat sloppy way. A stringent calculation can be found in the the standard QFT books, *e.g.* [4], Section 18.5.

Consider the terms $\bar{q}(z)\Gamma_\mu q(0)$, where $\Gamma^\mu = \gamma^\mu, \gamma^\mu\gamma_5$, that appear in the bilocal operators

$\mathcal{O}^{\rho}_{A,V}(z,0)$. We Taylor-expand $\bar{q}(z)\Gamma_\mu q(0)$ around $z=0$:

$$\bar{q}(z)\Gamma^\mu q(0) = \sum_{n=0}^{\infty} \frac{1}{n!}(z\cdot\partial)^n \bar{q}(z)\Big|_{z=0} \Gamma^\mu q(0) \tag{17}$$

$$= \left(\bar{q}(z)\sum_{n=0}^{\infty}\frac{1}{n!}(z\cdot\overleftarrow{\partial})^n\right)\Big|_{z=0}\Gamma^\mu q(0) \tag{18}$$

$$= \sum_{n=0}^{\infty}\frac{1}{n!} z_{\mu_1}\cdots z_{\mu_n}\bar{q}(z)\ \overleftarrow{\partial}^{\mu_1}\cdots\overleftarrow{\partial})^{\mu_n}\Big|_{z=0}\Gamma^\mu q(0) \tag{19}$$

In principle Eq. (16) is gauge invariant only in the light cone gauge where $A\cdot z = 0$. To make it generally gauge invariant a path-ordered product of the gauge fields along the line between 0 and z has to be inserted in $\mathcal{O}^{\rho}_{A,V}(z,0)$. We now account for gauge invariance by replacing the derivative ∂_μ by the covariant derivative $D_\mu = \partial_\mu + ig_0 A_\mu$. Also, together with the z^λ that appears in the integral, we formally have a term $z_\mu\Gamma_\mu$.

$$\bar{q}(z)\Gamma^\mu q(0) = \bar{q}(0)\sum_{n=0}^{\infty}\frac{1}{n!} z_{\mu_0}z_{\mu_1}\cdots z_{\mu_n}\Gamma_{\mu_0}\overleftarrow{D}^{\mu_1}\cdots\overleftarrow{D}^{\mu_n}\Gamma^\mu q(0) \tag{20}$$

$$= \sum_{n=0}^{\infty}\frac{1}{n!} z_{\mu_0}\cdots z_{\mu_n}\mathcal{O}^{\mu_0\cdots\mu_n}(0), \tag{21}$$

Here, $\mathcal{O}^{\mu_0\cdots\mu_n}(x) = \bar{q}(x)\Gamma_{\mu_0}\overleftarrow{D}^{\mu_1}\cdots\overleftarrow{D}^{\mu_n}q(x)$ are local twist-two operators. Note that in principle there are contributions of higher twist coming from the terms omitted in Eq. (14), but those are strongly suppressed as indicated before. Since $z^2 = 0$ $z_{\mu_0}\cdots z_{\mu_n}$ has to be traceless in the sense that the trace over a pair of indices vanishes. Therefore, in practice one takes only the traceless piece of the operators $\mathcal{O}^{\mu_0\cdots\mu_n}$. Note also, that we have a second term $\bar{q}(0)\Gamma^\mu q(z)$ in the definition of the bi-local operators $\mathcal{O}^{\rho}_{A,V}(z,0)$. The Taylor expansion of this term leads to a derivative that acts to the right side. Both terms then give rise to a symmetric derivative.

Now the moments of the integral in Eq. (16), which are directly related to the moments of parton distributions via Eq. (2.13) correspond to the single terms in Eq. (21).

Appendix B

3 Evaluation of Correlation Functions using the Sequential Method

In this section we give the expressions that have been omitted in Sec. 5.7.1. We start by considering the connected piece of a 3-point function of the nucleon with an operator $\mathcal{O} = \bar{u}(x)Xu(x)$ [*cf.* Eq. (3.35)], where X may be a combination of gamma matrices or a twist-two operator, but generally $\mathcal{O}$ must be a local operator. We write the connected piece of the 3-point function in terms of propagators and drop the gauge average since our discussion here does not depend thereof.

$$\begin{aligned} C_3^{\alpha'\alpha}(x',y,x)\Big|_{CONN} &= \bar{\zeta}_{\alpha'B'C'D'}\,\zeta_{\alpha BCD}\,X^{EE'}\,S_d^{C'C}(x',x) \\ &\times\Big\{S_u^{B'B}(x',x)S_u^{D'E}(x',y)S_u^{E'D}(y,x) - S_u^{B'D}(x',x)S_u^{D'E}(x',y)S_u^{E'B}(y,x) \\ &\quad + S_u^{D'D}(x',x)S_u^{B'E}(x',y)S_u^{E'B}(y,x) - S_u^{D'B}(x',x)S_u^{B'E}(x',y)S_u^{E'D}(y,x)\Big\} \end{aligned} \tag{22}$$

Here the ζ symbols are defined according to Eq. (3.29), which we write again below,

$$\zeta_{\alpha BCD} = \varepsilon^{bcd}\delta_{\alpha\beta}\,(\mathcal{C}\gamma_5)_{\gamma\delta}\,, \quad \bar{\zeta}_{\alpha BCD} = \varepsilon^{dcb}\,(\mathcal{C}\gamma_5)_{\delta\gamma}\,\delta_{\beta\alpha}, \tag{23}$$

where $B = (\beta, b)$, $C = (\gamma, c)$ and $D = (\delta, d)$ are used as combined indices for better readability. In practice we need the momentum and spin projected 3-point function,

$$C_3^{\Gamma}(\vec{p}\,',t',\tau;\vec{p},x) = \Gamma^{\alpha\alpha'}\sum_{\vec{x}',\vec{y}} e^{i\vec{p}'\cdot(\vec{x}'-\vec{y})}\;e^{i\vec{p}\cdot(\vec{y}-\vec{x})}\;C_3^{\alpha'\alpha}(x',y,x)\Big|_{CONN}. \tag{24}$$

Following the discussion in Sec. 5.7.1 we write the 3-point function as

$$C_3^{\Gamma}(\vec{p}\,',t',\tau;\vec{p},x) = \sum_{\vec{x}',\vec{y}} e^{i\vec{p}'\cdot(\vec{x}'-\vec{y})}\;e^{i\vec{p}\cdot(\vec{y}-\vec{x})}\;\Sigma^{F'F}(x',x;\Gamma)\;X^{EE'}(y)\;S_u^{F'E}(x',y)S_u^{E'F}(y,x), \tag{25}$$

where

$$\begin{aligned} \Sigma^{F'F}(x',x;\Gamma) = \Gamma_{\alpha\alpha'}\,\bar{\zeta}_{\alpha'B'C'D'}\,\zeta_{\alpha BCD}\;S_d^{C'C}(x',x) \\ \Big[S_u^{B'B}(x',x)\delta^{F'D'}\delta^{FD} - S_u^{B'D}(x',x)\delta^{F'D'}\delta^{FB} \\ + S_u^{D'D}(x',x)\delta^{F'B'}\delta^{FB} - S_u^{D'B}(x',x)\delta^{F'B'}\delta^{FD}\Big] \end{aligned} \tag{26}$$

contains now all the parts of $C_3^{\Gamma}(\vec{p}', t', \tau; \vec{p}, x)$ depending explicitly on the sink position.
The generalized propagator is then defined

$$S_G^{FE'}(t', x, y, \vec{p}'; \Gamma) = \sum_{\vec{x}'} e^{i\vec{p}'\cdot(\vec{x}'-\vec{y})}\ \Sigma^{F'F}(x', x; \Gamma)\ S_u^{F'E}(x', y). \tag{27}$$

Using the γ_5-hermiticity of the quark propagator, Eq. (5.29), where we emphasize that there is a flavour change when we work in the twisted basis, we can define a modified generalized propagator

$$\begin{aligned}\tilde{S}_G(t', x, y, \vec{p}'; \Gamma) &= \gamma_5 S_G^{\dagger}(t', x, y, \vec{p}'; \Gamma) &(28)\\ &= \sum_{\vec{x}'} e^{-i\vec{p}'\cdot(\vec{x}'-\vec{y})}\ \gamma_5 S_u^{\dagger}(x', y)\ \Sigma^{\dagger}(x', x; \Gamma) &(29)\\ &= \sum_{\vec{x}'} e^{-i\vec{p}'\cdot(\vec{x}'-\vec{y})}\ S_d(y, x')\ \gamma_5 \Sigma^{\dagger}(x', x; \Gamma) &(30)\end{aligned}$$

Now the 3-point function can be rewritten as

$$C_3^{\Gamma}(\vec{p}', t', \tau; \vec{p}, x) = \sum_{\vec{y}} e^{i\vec{p}\cdot(\vec{y}-\vec{x})}\ \mathrm{Tr}\left[\tilde{S}_G^{\dagger}(t', x, y, \vec{p}'; \Gamma)\gamma_5 X\, S_u(y, x)\right]. \tag{31}$$

The sequential source is obtained by applying the Dirac operator, more precisely, the Dirac matrix M_d, to $\tilde{S}_G$.

$$\mathcal{S}(z, x, t', \vec{p}'; \Gamma)\ = \sum_{\vec{x}'} e^{-i\vec{p}'\cdot(\vec{x}'-\vec{y})}\ \delta_{zx'}\ \Sigma^{\dagger}(x', x; \Gamma), \tag{32}$$

$\mathcal{S}$ is non-zero only on the sink timeslice t'. Calculating the propagator of this sequential source yields $\tilde{S}_G$ and hence the 3-point is obtained according to Eq. (31).
We remind the reader that t' and p' (and also Γ) are fixed when using this method, which is why it is often refered to as fixed sink method.

The corresponding fixed current method, where the timeslice τ of the operator insertion and the operator itself are fixed, see Sec. 5.7.1 for the case of an operator of type $\mathcal{O} = \bar{d}(x)Xd(x)$, works as follows when the operator is of the type $\bar{u}(x)Xu(x)$. The generalized propagator is defined as

$$S_G^{F'F}(x', x, \tau, \vec{p}; X) := \sum_{\vec{y}} e^{-i\vec{p}\cdot(\vec{y}-\vec{x})}\ S_u^{F'E}(x', y) X^{EE'}(y)\ S_u^{E'F}(y, x), \tag{33}$$

the sequential source reads

$$\mathcal{S}(z, x, \tau, \vec{p}; X) = \sum_{\vec{y}} e^{-i\vec{p}\cdot(\vec{y}-\vec{x})}\ \delta_{zy} O(y)\ S_u(y, x) \tag{34}$$

and the 3-point function is obtained using the generalized propagator obtained by inversion of

the sequential source,

$$C_3^{\Gamma}(\vec{p}', t', \tau; \vec{p}, x) = \Gamma^{\alpha\alpha'} \bar{\zeta}_{\alpha' B' C' D'} \zeta_{\alpha B C D} \sum_{\vec{x}'} e^{i\vec{p}'\cdot(\vec{x}'-\vec{y})} \; S_d^{C'C}(x', x) \\ \Big\{ S_u^{B'B}(x', x) S_G^{D'D}(x', x, \tau, \vec{p}; \mathrm{X}) - S_u^{B'D}(x', x) S_G^{D'B}(x', x, \tau, \vec{p}; \mathrm{X}) \\ + S_u^{D'D}(x', x) S_G^{B'B}(x', x, \tau, \vec{p}; \mathrm{X}) - S_u^{D'B}(x', x) S_G^{B'D}(x', x, \tau, \vec{p}; \mathrm{X}) \Big\}, \quad (35)$$

cf. Eq. (5.38).

Appendix C

4 A variant of the twisted mass noise reduction technique

In this section we give the details of the noise-reduction technique (vv-method) that we can use when dealing with disconnected pieces of SU(3) isospin octet currents

$$\mathcal{O}_8 = \bar{u}Xu + \bar{d}Xd - 2\bar{s}Xs. \tag{36}$$

The disconnected pieces require the evaluation of quark loops, which read

$$X\left(\frac{1}{M_u} + \frac{1}{M_d} - \frac{2}{M_s}\right) = X\left(\frac{1}{M_u} - \frac{1}{M_s}\right) + X\left(\frac{1}{M_d} - \frac{1}{M_s}\right) \tag{37}$$

In twisted basis (at maximal twist) we can use different fields for the physical s quark fields. Hence the expression reads

$$X^{\mathrm{tw},+}\left(\frac{1}{M_u} - \frac{1}{M_{s_+}}\right) + X^{\mathrm{tw},-}\left(\frac{1}{M_d} - \frac{1}{M_{s_-}}\right), \tag{38}$$

$$X^{\mathrm{tw},\pm} = e^{\pm i\frac{\pi}{4}\gamma_5} X e^{\pm i\frac{\pi}{4}\gamma_5} \tag{39}$$

where s_+ (s_-) correspond to using the Wilson parameter $r = +1$ ($r = -1$) in the heavy valence quark action in the mixed action setup, see Sec. 5.3. Note that in the expressions above we have the Dirac matrices M_q in the twisted basis but do not label this explicitly. We can now derive [*cf.* Eq. (5.41) *ff*]

$$(M_u - M_{s_+}) = 2i\kappa a(\mu_l - \mu_s)X\gamma_5, \tag{40}$$

$$\Rightarrow \frac{1}{M_u} - \frac{1}{M_{s_+}} = \frac{M_{s_+}}{M_u M_{s_+}} - \frac{M_u}{M_u M_{s_+}} \tag{41}$$

$$= -\frac{1}{M_u}\left(M_u - M_{s_+}\right)\frac{1}{M_{s_+}} = -2i\kappa a\left(\mu_l - \mu_s\right)\frac{1}{M_u}\gamma_5\frac{1}{M_{s_+}} \tag{42}$$

$$= -2i\kappa a\left(\mu_l - \mu_s\right)\gamma_5\left(\frac{1}{M_d}\right)^\dagger\frac{1}{M_{s_+}}. \tag{43}$$

For the second term in the r.h.s. of Eq. (37), we obtain accordingly

$$\frac{1}{M_d} - \frac{1}{M_{s_-}} = -2i\kappa a \left((-\mu_l) - (-\mu_s)\right) \gamma_5 \left(\frac{1}{M_u}\right)^\dagger \frac{1}{M_{s_-}} \tag{44}$$

$$= 2i\kappa a \left(\mu_l - \mu_s\right) \gamma_5 \left(\frac{1}{M_u}\right)^\dagger \frac{1}{M_{s_-}}. \tag{45}$$

Thus, we obtain

$$X\left(\frac{1}{M_u} + \frac{1}{M_d} - \frac{2}{M_s}\right) = \\ - 2i\kappa a \left(\mu_l - \mu_s\right) \left(X^{\mathrm{tw},+}\gamma_5 \left(\frac{1}{M_d}\right)^\dagger \frac{1}{M_{s_+}} - X^{\mathrm{tw},+}\gamma_5 \left(\frac{1}{M_u}\right)^\dagger \frac{1}{M_{s_-}}\right) \tag{46}$$

and we can estimate the product of the propagators appearing in the r.h.s. of the above expression using stochastic sources,

$$\left(\frac{1}{M_d}\right)^\dagger \frac{1}{M_{s_+}} = \phi_d^* \phi_{s_+}, \tag{47}$$

$$\left(\frac{1}{M_u}\right)^\dagger \frac{1}{M_{s_-}} = \phi_u^* \phi_{s_-}, \tag{48}$$

$$\phi_q = \frac{1}{M_q}\xi, \tag{49}$$

where ξ is a stochastic noise vector, see Sec. 5.4, and we implicitly assume a sum over stochastic noise vectors. Strictly speaking, equality holds in the limit of infinitely many stochastic sources.

One noteworthy property of the identity (46) is that in the limit $\mu_s \to \mu_l$, the $SU(3)$ isospin limit, disconnected contributions to the octet current vanish, even at finite lattice spacing and unphysical pion mass. Since in our setup, where the mass of the strange quark is fixed to approximately the physical strange quark mass, the mass difference $\mu_l - \mu_s$ becomes larger in the physical limit of the pion mass, we expect disconnected contributions to increase when decreasing the light quark mass (and correspondingly the mass of the pion) to its physical value.

Bibliography

[1] M. Breidenbach, J.I. Friedman, H.W. Kendall, E.D. Bloom, D.H. Coward, et al. Observed Behavior of Highly Inelastic electron-Proton Scattering. *Phys.Rev.Lett.*, 23:935–939, 1969.

[2] E.D. Bloom, G. Buschhorn, R.L. Cottrell, D.H. Coward, H.C. DeStaebler, et al. Recent Results in Inelastic Electron Scattering. 1970. 15th International Conference on High Energy Physics, Kiev, USSR.

[3] J.D. Bjorken and E.A. Paschos. Inelastic Electron Proton and gamma Proton Scattering, and the Structure of the Nucleon. *Phys.Rev.*, 185:1975–1982, 1969.

[4] M.E. Peskin and D.V. Schroeder. An Introduction to quantum field theory. *Addison-Wesley, Reading, USA*, pages 1–842, 1995.

[5] A.D. Martin, W.J. Stirling, R.S. Thorne, and G. Watt. Parton distributions for the LHC. *Eur.Phys.J.*, C63:189–285, 2009, 0901.0002.

[6] R. Brock et al. Handbook of perturbative QCD: Version 1.0. *Rev.Mod.Phys.*, 67:157–248, 1995.

[7] S. Alekhin, J. Blumlein, S. Klein, and S. Moch. The 3, 4, and 5-flavor NNLO Parton Distributions Functions from Deep-Inelastic-Scattering Data and at Hadron Colliders. *Phys.Rev.*, D81:014032, 2010, 0908.2766.

[8] R. D. Ball et al. Unbiased global determination of parton distributions and their uncertainties at NNLO and at LO. *Nucl.Phys.*, B855:153–221, 2012, 1107.2652.

[9] P. Jimenez-Delgado and E. Reya. Dynamical NNLO parton distributions. *Phys.Rev.*, D79: 074023, 2009, 0810.4274.

[10] J. Kretzschmar. Proton Structure Measurements and the HERAPDF fit. *To appear in the proceedings of Lake Louise Winter Institute: Fundamental Interactions (LLWI 2009)*, 2009, 0906.1108.

[11] K. Nakamura et al. Review of particle physics. *J.Phys.G*, G37:075021, 2010.

[12] M.L. Goldberger and S.B. Treiman. Form-factors in Beta decay and muon capture. *Phys.Rev.*, 111:354–361, 1958.

[13] C.A. Dominguez. The Goldberger-Treiman Relation: A Probe of the Chiral Symmetries of Quantum Chromodynamics. *Riv.Nuovo Cim.*, 8N6:1–27, 1985.

[14] R. P. Feynman. Forces in Molecules. *Phys. Rev.*, 56:340–343, 1939.

[15] ATLAS collaboration. Observation of an Excess of Events in the Search for the Standard Model Higgs boson with the ATLAS detector at the LHC. Technical Report ATLAS-CONF-2012-093, CERN, Geneva, Jul 2012.

[16] G. Bertone, D. Hooper, and J. Silk. Particle dark matter: Evidence, candidates and constraints. *Phys.Rept.*, 405:279–390, 2005, hep-ph/0404175.

[17] H.J. Schnitzer. Sigma term in pion-nucleon scattering. *Phys.Rev.*, D5:1482–1493, 1972.

[18] T.P. Cheng and Roger F. Dashen. Is SU(2) x SU(2) a better symmetry than SU(3)? *Phys.Rev.Lett.*, 26:594, 1971.

[19] M.M. Pavan, I.I. Strakovsky, R.L. Workman, and R.A. Arndt. The Pion nucleon Sigma term is definitely large: Results from a G.W.U. analysis of pi nucleon scattering data. *PiN Newslett.*, 16:110–115, 2002, hep-ph/0111066.

[20] J.M. Alarcon, J. Martin Camalich, and J.A. Oller. The chiral representation of the pi N scattering amplitude and the pion-nucleon sigma term. *Phys.Rev.*, D85:051503, 2012, 1110.3797.

[21] R.D. Young and A.W. Thomas. Recent results on nucleon sigma terms in lattice QCD. *Nucl.Phys.*, A844:266C–271C, 2010, 0911.1757.

[22] G. Martinelli, C. Pittori, C.T. Sachrajda, M. Testa, and A. Vladikas. A General method for nonperturbative renormalization of lattice operators. *Nucl.Phys.*, B445:81–108, 1995, hep-lat/9411010.

[23] W. Celmaster and R.J. Gonsalves. The Renormalization Prescription Dependence of the QCD Coupling Constant. *Phys.Rev.*, D20:1420, 1979.

[24] J.A. Gracey. Three loop anomalous dimension of nonsinglet quark currents in the RI-prime scheme. *Nucl.Phys.*, B662:247–278, 2003, hep-ph/0304113.

[25] H.J. Rothe. Lattice gauge theories: An Introduction. *World Sci.Lect.Notes Phys.*, 74:1–605, 2005.

[26] I. Montvay and G. Munster. Quantum fields on a lattice. *Cambridge, UK: Univ. Pr. (Cambridge monographs on mathematical physics)*, pages 1–491, 1994.

[27] C. Gattringer and C. B. Lang. Quantum chromodynamics on the lattice. *Lect.Notes Phys.*, 788:1–211, 2010.

[28] A. Zichichi. New Phenomena in Subnuclear Physics. Part A. Proceedings: First Half of the 1975 International School of Subnuclear Physics, Erice, Sicily, Jul 11-Aug 1 1975. *Plenum, NewYork*, pages 1–558, 1977.

[29] K. G. Wilson. Confinement of Quarks. *Phys.Rev.*, D10:2445–2459, 1974.

[30] E. Seiler. Gauge Theories as a Problem of Constructive Quantum Field Theory and Statistical Mechanics. *Lect.Notes Phys.*, 159:1–192, 1982.

[31] A.D. Kennedy. Algorithms for dynamical fermions. *Plenary talk at the 24th International Symposium on Lattice Field Theory (Lattice 2006)*, 2006, hep-lat/0607038.

[32] M. Luscher. Computational Strategies in Lattice QCD. *Les Houches Summer School: Session 93: Modern perspectives in lattice QCD: Quantum field theory and high performance computing*, pages 331–399, 2010, 1002.4232.

[33] M. Luscher. Advanced lattice QCD. *Les Houches Summer School, Session 68: Probing the Standard Model of Particle Interactions*, pages 229–280, 1998, hep-lat/9802029.

[34] G. Martinelli, G.C. Rossi, C.T. Sachrajda, S. R. Sharpe, M. Talevi, and M. Testa. Nonperturbative improvement of composite operators with Wilson fermions. *Phys.Lett.*, B411: 141–151, 1997, hep-lat/9705018.

[35] A. Vladikas. Three Topics in Renormalization and Improvement. *Les Houches Summer School: Session 93: Modern perspectives in lattice QCD: Quantum field theory and high performance computing*, pages 161–222, 2011, 1103.1323.

[36] P. Dimopoulos, R. Frezzotti, G. Herdoiza, K. Jansen, V. Lubicz, et al. Renormalization constants for Wilson fermion lattice QCD with four dynamical flavours. *PoS*, LATTICE2010: 235, 2010, 1101.1877.

[37] C. Alexandrou, M. Constantinou, T. Korzec, H. Panagopoulos, and F. Stylianou. Renormalization constants for 2-twist operators in twisted mass QCD. *Phys.Rev.*, D83:014503, 2011, 1006.1920.

[38] C. Alexandrou, M. Constantinou, T. Korzec, H. Panagopoulos, and F. Stylianou. Renormalization constants for one-derivative fermion operators in twisted mass QCD. *PoS*, LATTICE2010:224, 2010, 1012.2981.

[39] M. Constantinou, P. Dimopoulos, R. Frezzotti, V. Lubicz, H. Panagopoulos, A. Skouroupathisa, and F. Stylianou. Perturbative renormalization factors and O(a**2) corrections for lattice 4-fermion operators with improved fermion/gluon actions. *Phys.Rev.*, D83:074503, 2011, 1011.6059.

[40] M. Constantinou et al. Non-perturbative renormalization of quark bilinear operators with Nf = 2 (tmQCD) Wilson fermions and the tree-level improved gauge action. *JHEP*, 1008:068, 2010, 1004.1115.

[41] Maarten Golterman. Applications of chiral perturbation theory to lattice QCD. *Les Houches Summer School: Session 93: Modern perspectives in lattice QCD: Quantum field theory and high performance computing*, pages 423–515, 2009, 0912.4042.

[42] P. Boucaud et al. Dynamical Twisted Mass Fermions with Light Quarks: Simulation and Analysis Details. *Comput.Phys.Commun.*, 179:695–715, 2008, 0803.0224.

[43] S. Durr, Z. Fodor, C. Hoelbling, S.D. Katz, S. Krieg, et al. Lattice QCD at the physical point: Simulation and analysis details. *JHEP*, 1108:148, 2011, 1011.2711.

[44] B. B. Brandt, S. Capitani, D. Djukanovic, G. von Hippel, B. Jager, et al. Wilson fermions at fine lattice spacings: scale setting, pion form factors and (g-2)_mu. *PoS*, LATTICE2010: 164, 2010, 1010.2390.

[45] R. Baron, Ph. Boucaud, J. Carbonell, A. Deuzeman, V. Drach, et al. Light hadrons from lattice QCD with light (u,d), strange and charm dynamical quarks. *JHEP*, 1006:111, 2010, 1004.5284.

[46] R. Baron et al. Light hadrons from Nf=2+1+1 dynamical twisted mass fermions. *PoS*, LATTICE2010:123, 2010, 1101.0518.

[47] K. Jansen, T. Trappenberg, I. Montvay, G. Munster, and U. Wolff. Broken Phase of the Four-Dimensional Ising Model in a Finite Volume. *Nucl.Phys.*, B322:698, 1989.

[48] M. Luscher. Selected Topics in Lattice Field Theory. *Conf.Proc.*, C880628:451–528, 1988.

[49] K. Symanzik. Continuum Limit and Improved Action in Lattice Theories. 1. Principles and phi**4 Theory. *Nucl.Phys.*, B226:187, 1983.

[50] Y. Iwasaki. Renormalization Group Analysis of Lattice Theories and Improved Lattice Action: Two-Dimensional Nonlinear O(N) Sigma Model. *Nucl.Phys.*, B258:141–156, 1985.

[51] A. Shindler. Twisted mass lattice QCD. *Phys.Rept.*, 461:37–110, 2008, 0707.4093.

[52] S.R. Sharpe and J.M.S. Wu. Twisted mass chiral perturbation theory at next-to-leading order. *Phys.Rev.*, D71:074501, 2005, hep-lat/0411021.

[53] S. Aoki and O. Bar. Twisted-mass QCD, O(a) improvement and Wilson chiral perturbation theory. *Phys.Rev.*, D70:116011, 2004, hep-lat/0409006.

[54] R. Frezzotti, G. Martinelli, M. Papinutto, and G.C. Rossi. Reducing cutoff effects in maximally twisted lattice QCD close to the chiral limit. *JHEP*, 0604:038, 2006, hep-lat/0503034.

[55] R. Frezzotti and G.C. Rossi. Chirally improving Wilson fermions. 1. O(a) improvement. *JHEP*, 0408:007, 2004, hep-lat/0306014.

[56] R. Baron, B. Blossier, P. Boucaud, A. Deuzeman, V. Drach, et al. First results of ETMC simulations with N(f) = 2+1+1 maximally twisted mass fermions. *PoS*, LAT2009:104, 2009, 0911.5244.

[57] R. Frezzotti and G.C. Rossi. Chirally improving Wilson fermions. II: Four-quark operators. *JHEP*, 10:070, 2004, hep-lat/0407002.

[58] O. Bar, G. Rupak, and N. Shoresh. Simulations with different lattice Dirac operators for valence and sea quarks. *Phys.Rev.*, D67:114505, 2003, hep-lat/0210050.

[59] C. Alexandrou, T. Leontiou, J.W. Negele, and A. Tsapalis. The Axial N to Delta transition form factors from Lattice QCD. *Phys.Rev.Lett.*, 98:052003, 2007, hep-lat/0607030.

[60] J.D. Bratt et al. Nucleon structure from mixed action calculations using 2+1 flavors of asqtad sea and domain wall valence fermions. *Phys.Rev.*, D82:094502, 2010, 1001.3620.

[61] K. Cichy, V. Drach, E. Garcia Ramos, G. Herdoiza, and K. Jansen. Overlap Valence Quarks on a Twisted Mass Sea. *PoS*, LATTICE2010:077, 2010, 1011.0639.

[62] S. Dinter, V. Drach, R. Frezzotti, G. Herdoiza, K. Jansen, and G. Rossi. Sigma terms and strangeness content of the nucleon with $N_f = 2 + 1 + 1$ twisted mass fermions. *Submitted to JHEP*, 2012, 1202.1480.

[63] Y. Saad. Iterative methods for sparse linear systems. *Philadelphia SIAM*, pages 1–528, 2003.

[64] S. Basak et al. Clebsch-Gordan construction of lattice interpolating fields for excited baryons. *Phys.Rev.*, D72:074501, 2005, hep-lat/0508018.

[65] G. Martinelli and C.T. Sachrajda. A Lattice STUDY OF NUCLEON STRUCTURE. *Nucl.Phys.*, B316:355, 1989.

[66] M. Luscher and U. Wolff. How to calculate the elastic scattering matrix in two-dimensional quantum field theories by numerical simulation. *Nucl.Phys.*, B339:222–252, 1990.

[67] B. Blossier, M. Della Morte, G. von Hippel, T. Mendes, and R. Sommer. On the generalized eigenvalue method for energies and matrix elements in lattice field theory. *JHEP*, 0904:094, 2009, 0902.1265.

[68] B. Blossier, M. Della Morte, N. Garron, G. von Hippel, T. Mendes, H. Simma, and R. Sommer. HQET at order 1/m: III. Decay constants in the quenched approximation. *JHEP*, 1012:039, 2010, 1006.5816.

[69] R. Evans, G. Bali, and S. Collins. Improved Semileptonic Form Factor Calculations in Lattice QCD. *Phys.Rev.*, D82:094501, 2010, 1008.3293.

[70] C. Alexandrou, M. Brinet, J. Carbonell, M. Constantinou, P.A. Harraud, et al. Nucleon electromagnetic form factors in twisted mass lattice QCD. *Phys.Rev.*, D83:094502, 2011, 1102.2208.

[71] C. Alexandrou. Private communication, 2012. ETM Collaboration.

[72] A.D. Martin, W.J. Stirling, R.S. Thorne, and G. Watt. Uncertainties on alpha(S) in global PDF analyses and implications for predicted hadronic cross sections. *Eur.Phys.J.*, C64: 653–680, 2009, 0905.3531.

[73] C. Alexandrou, J. Carbonell, M. Constantinou, P.A. Harraud, P. Guichon, et al. Moments of nucleon generalized parton distributions from lattice QCD. *Phys.Rev.*, D83:114513, 2011, 1104.1600.

[74] D. Pleiter et al. Nucleon form factors and structure functions from N(f)=2 Clover fermions. *PoS*, LATTICE2010:153, 2010, 1101.2326.

[75] A. Sternbeck. Private communication for the QCDSF collaboration, 2011.

[76] Y. Aoki, T. Blum, H.-W. Lin, S. Ohta, S. Sasaki, et al. Nucleon isovector structure functions in (2+1)-flavor QCD with domain wall fermions. *Phys.Rev.*, D82:014501, 2010, 1003.3387.

[77] W. Detmold, W. Melnitchouk, J.W. Negele, D.B. Renner, and A. . Thomas. Chiral extrapolation of lattice moments of proton quark distributions. *Phys.Rev.Lett.*, 87:172001, 2001, hep-lat/0103006.

[78] J. Green, M. Engelhardt, S. Krieg, J. Negele, A. Pochinsky, and S. Syritsyn. Nucleon structure with pion mass down to 150 MeV. *Talk given at the 30th International Symposium on Lattice Field Theory (Lattice 2012), Cairns, Australia*, 2012.

[79] S. Dinter, C. Alexandrou, M. Constantinou, V. Drach, K. Jansen, and D. Renner. Nucleon matrix elements with $N_f = 2 + 1 + 1$ maximally twisted fermions. *PoS*, LATTICE2010: 135, 2010, 1101.5540.

[80] S.D. Bass and A.W. Thomas. The Nucleon's octet axial-charge g(A)**(8) with chiral corrections. *Phys.Lett.*, B684:216–220, 2010, 0912.1765.

[81] S. Alekhin and J. Blumlein. Private communication, 2011.

[82] J. Green, S. Krieg, J. Negele, A. Pochinsky, and S. Syritsyn. Excited state contamination in nucleon structure calculations. *PoS*, LATTICE2011:157, 2011, 1111.0255.

[83] S. Capitani, B. Knippschild, M. Della Morte, and H. Wittig. Systematic errors in extracting nucleon properties from lattice QCD. *PoS*, LATTICE2010:147, 2010, 1011.1358.

[84] S. Capitani, M. Della Morte, G. von Hippel, B. Jager, A. Juttner, et al. The nucleon axial charge from lattice QCD with controlled errors. *Phys.Rev.*, D86:074502, 2012, 1205.0180.

[85] D. Pleiter. Private communication for the QCDSF collaboration, 2010.

[86] C. Alexandrou, M. Constantinou, S. Dinter, V. Drach, K. Jansen, and D.B. Renner. Precision Study of Excited State Effects in Nucleon Matrix Elements. *Phys.Lett.*, B704:89–93, 2011, 1108.1076.

[87] C. Alexandrou, M. Constantinou, S. Dinter, V. Drach, K. Jansen, and D. Renner. Excited State Effects in Nucleon Matrix Element Calculations. *PoS*, LATTICE2011:150, 2011, 1112.2931.

[88] J. Bulava, M. Donnellan, and R. Sommer. On the computation of hadron-to-hadron transition matrix elements in lattice QCD. *JHEP*, 1201:140, 2012, 1108.3774.

[89] C. Alexandrou, A. Constantinou, and T. Leontiou. Private communication, 2011. ETM Collaboration.

[90] Y. Hua and T. K. Sakar. Generalized Pencil-of-Function Method for Extracting Poles of an EM System from its Transient Response. *IEEE Transactions on Antennas and Propagation*, 37:229–234, 1989.

[91] C. Aubin and K. Orginos. A new approach for Delta form factors. *AIP Conf.Proc.*, 1374: 621–624, 2011, 1010.0202.

[92] P. Boucaud et al. Dynamical twisted mass fermions with light quarks. *Phys.Lett.*, B650: 304–311, 2007, hep-lat/0701012.

[93] P. Dimopoulos, R. Frezzotti, C. Michael, G.C. Rossi, and C. Urbach. O(a**2) cutoff effects in lattice Wilson fermion simulations. *Phys.Rev.*, D81:034509, 2010, 0908.0451.

[94] V. Drach. Private communication, 2012. ETM Collaboration.

[95] D. Toussaint and W. Freeman. The Strange quark condensate in the nucleon in 2+1 flavor QCD. *Phys.Rev.Lett.*, 103:122002, 2009, 0905.2432.

[96] K. Takeda et al. Nucleon strange quark content from two-flavor lattice QCD with exact chiral symmetry. *Phys.Rev.*, D83:114506, 2011, 1011.1964.

[97] G.S. Bali et al. A lattice study of the strangeness content of the nucleon. *Prog.Part.Nucl.Phys.*, 67:467–472, 2012, 1112.0024.

[98] K. G. Wilson. Nonlagrangian models of current algebra. *Phys.Rev.*, 179:1499–1512, 1969.

[99] F.J. Yndurain. The theory of quark and gluon interactions. *Berlin, Germany: Springer*, pages 1–474, 2006.

[100] T. Muta. Foundations of quantum chromodynamics. Second edition. *World Sci.Lect.Notes Phys.*, 57:1–409, 1998.

List of Figures

List of Tables

Selbständigkeitserklärung

Ich erkläre, dass ich die vorliegende Arbeit selbständig und nur unter Verwendung der angegebenen Literatur und Hilfsmittel angefertigt habe.

Berlin, den 09.08.2012 .....
Simon Dinter